Interpret the figures and text by expanding on what is being illustrated, explaining procedures or techniques, indicating why it might be important or making connections to our class readings and laboratory work. Tell more than rewriting the caption. Try to use your interpretation to demonstrate additional knowledge beyond what is shown here. You should write on each page for about 10 minutes. Some articles occupy two pages.

ACS Nano (2020) DOI: 10.1021/acsnano.0c00907

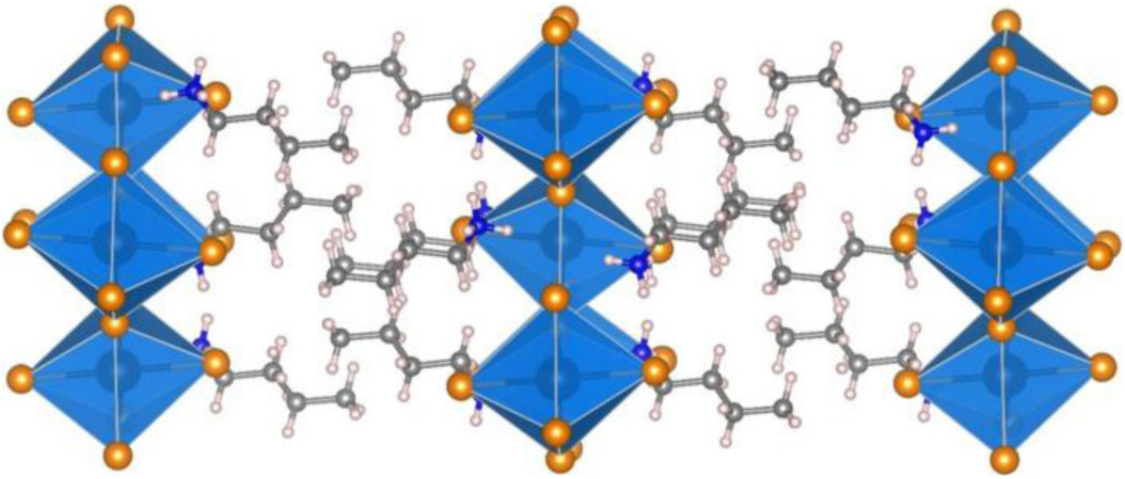

Figure S2. Crystal structure of $(BA)_2PbBr_4$

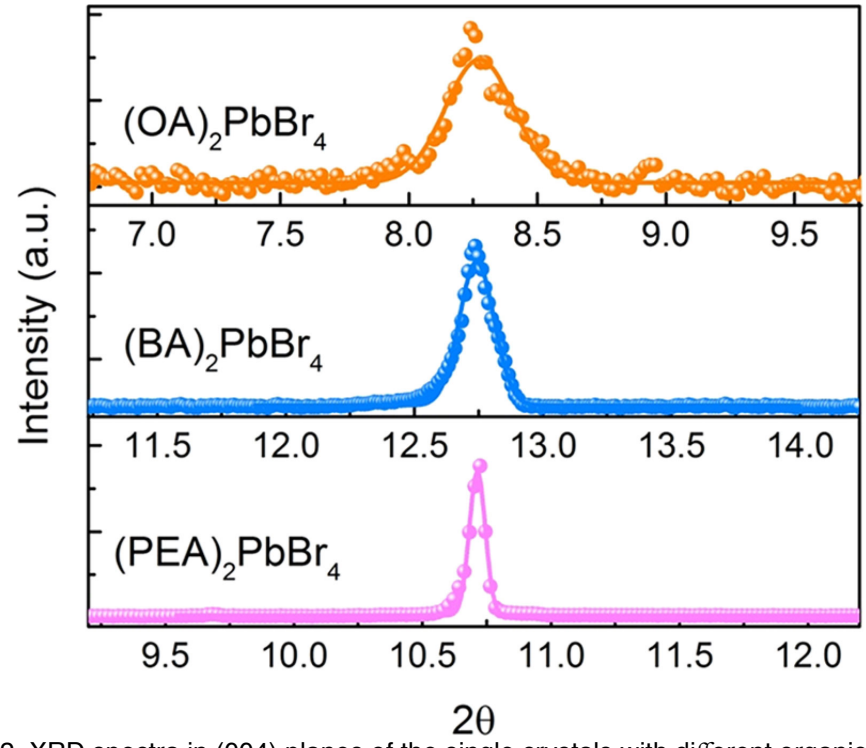

Figure 2. XRD spectra in (004) planes of the single crystals with different organic cations.

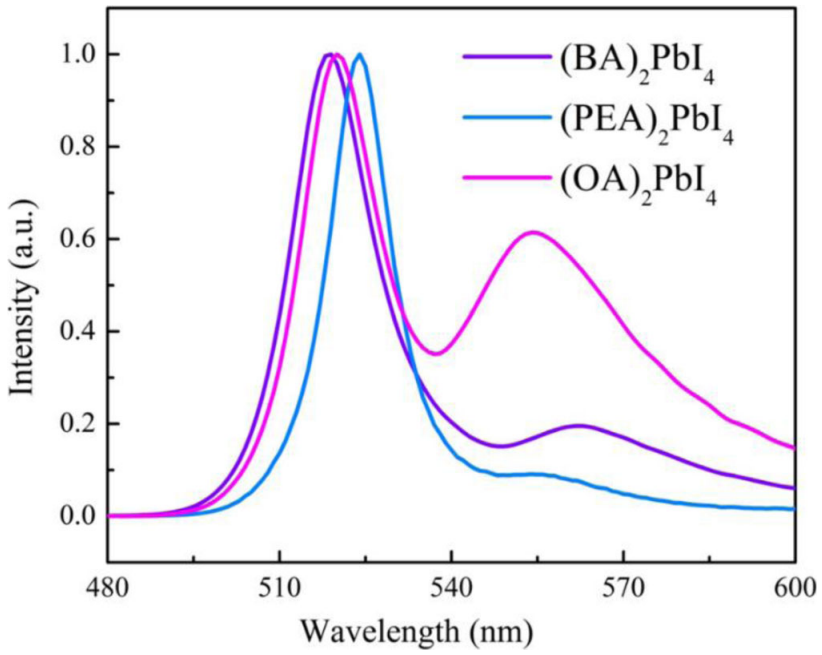

Figure S5. The PL spectra of $(BA)_2PbI_4$, $(PEA)_2PbI_4$, and $(OA)_2PbI_4$

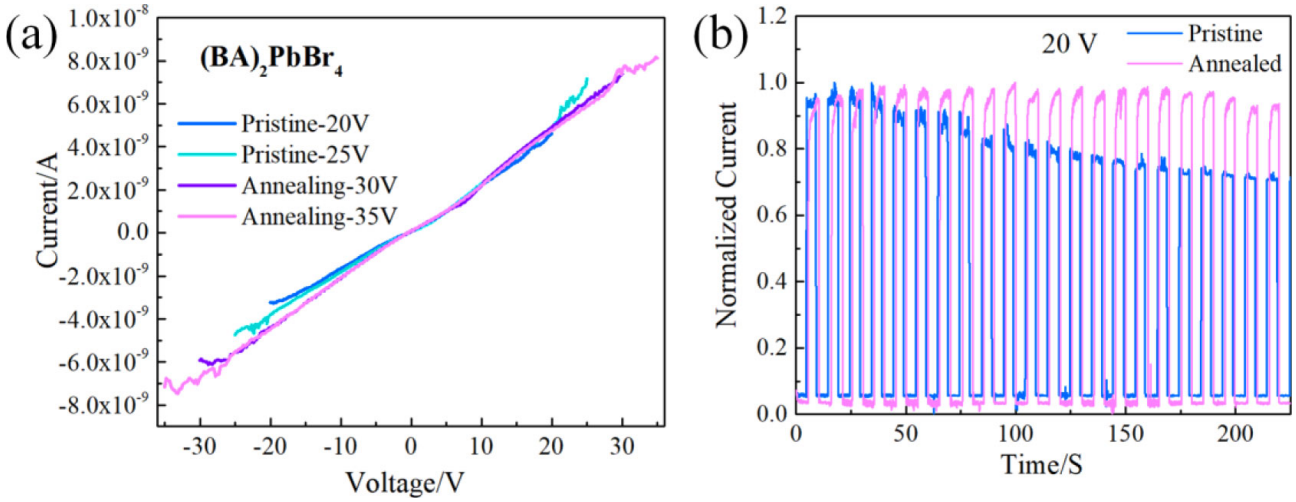

Figure S14. Photodetector based on $(BA)_2PbI_4$ (a) I–V curves under ultraviolet light at different voltages. (b) I–t curve illuminated by ultraviolet light at a bias of 20 V.

Filter membranes with a pore size of 200 nm (Nuclepore Track-Etched Polycarbonate (Hydrophilic) Membranes) were purchased from GE Healthcare Life Sciences and used to filter SWCNT suspensions.

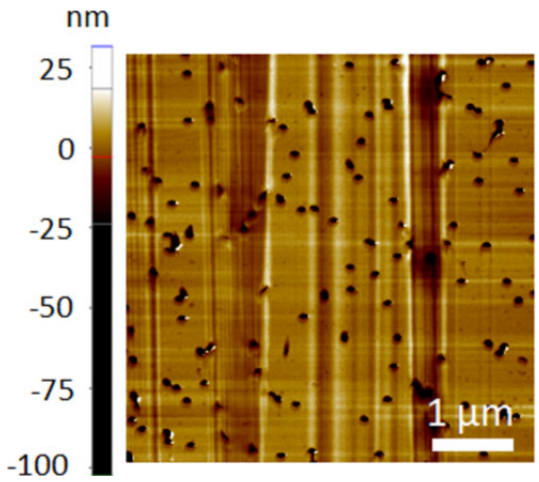

Figure 2. A magnified AFM image showing microgrooves on filter membranes.

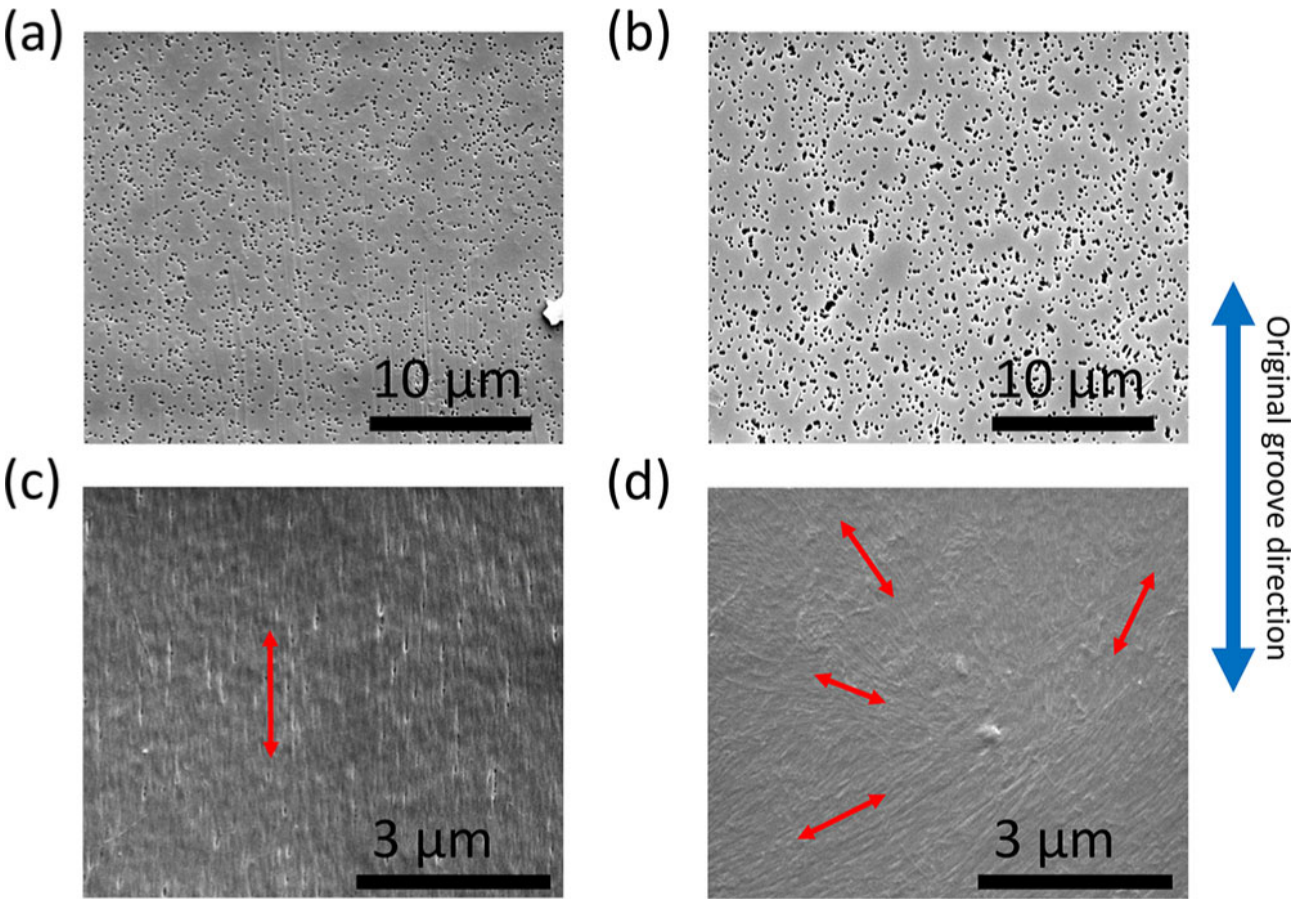

Figure 4. Disappearance of global alignment upon elimination of grooves through heating between glass slides on a hotplate. (a) An SEM image of a typical filter membrane without any treatment, showing microgrooves. (b) An SEM image of a filter membrane after heating treatment, exhibiting no grooves. (c) An SEM image of a CNT film made on the membrane shown in part a. The red arrow indicates the CNT alignment direction. (d) An SEM image of a CNT film made on the membrane shown in part b. The red arrows indicate the alignment directions of CNTs in domains.

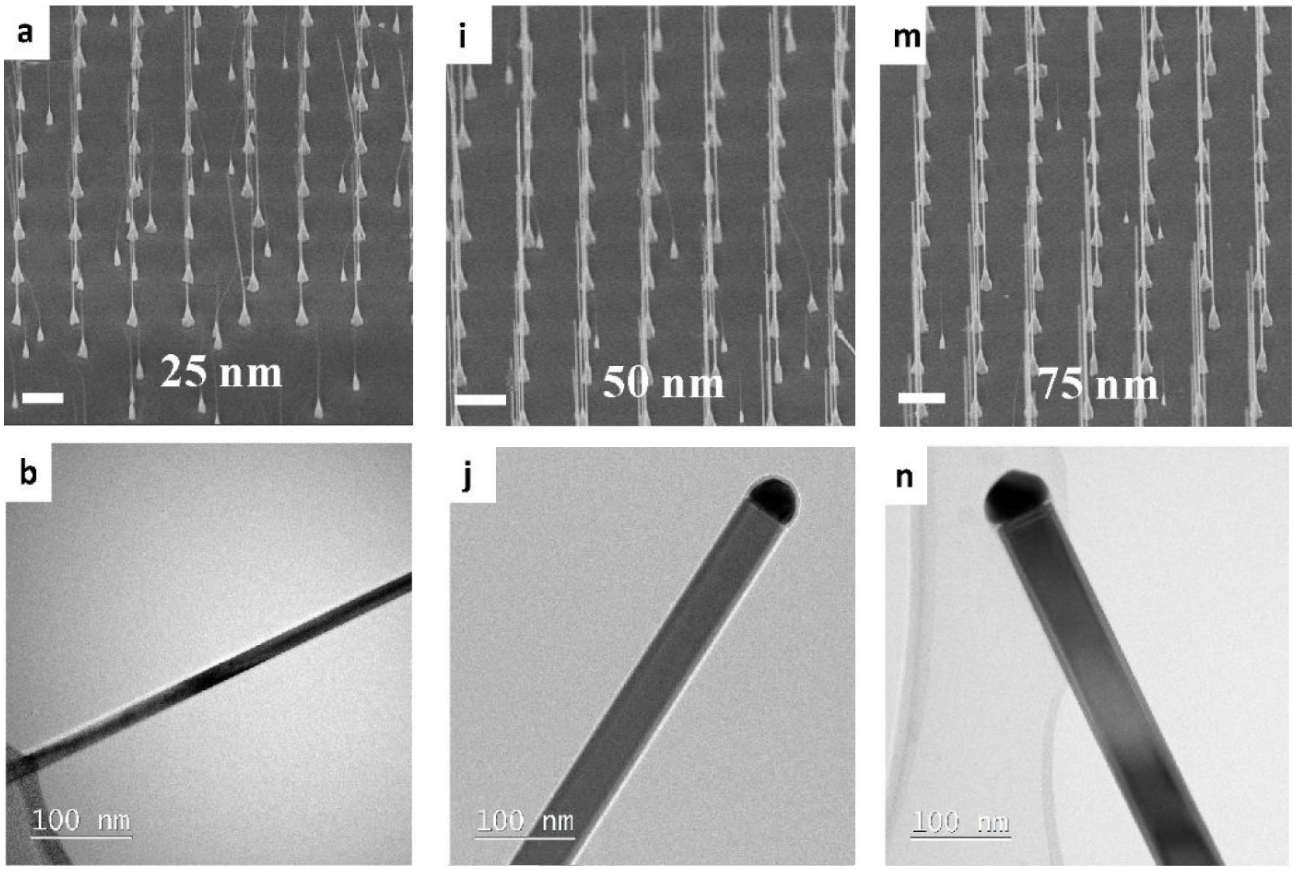

Figure S1. GaP nanowires (NWs) are grown by the vapour-liquid-solid (VLS) method, using an array of gold catalyst droplets. (a, i, m) SEM images of arrays of GaP NWs with increasing diameter. The scale bars are 2 µm. (b, j, n) TEM images of the NWs.

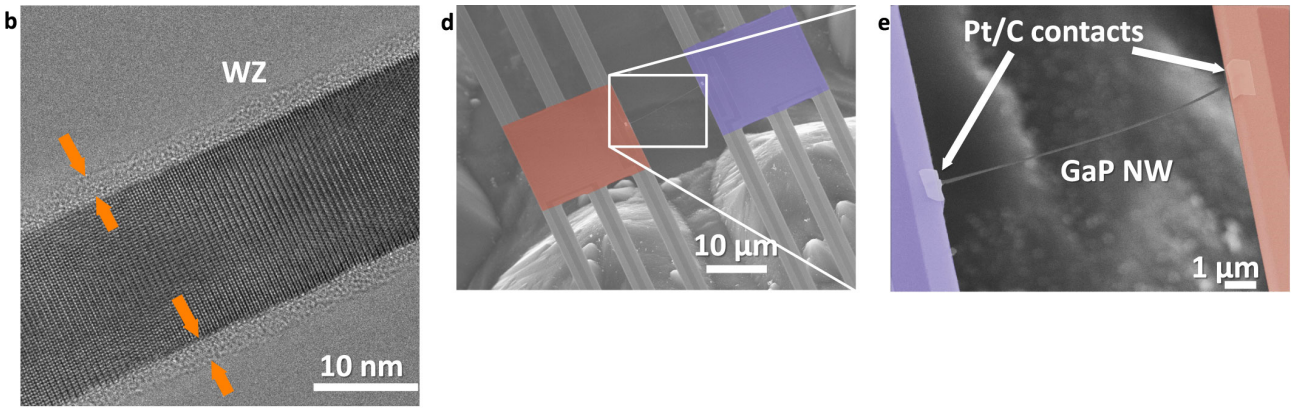

Figure 1. GaP NW properties and device for thermal conductance measurements. (b) High-resolution TEM image showing a defect-free WZ crystal structure and a layer of oxide (orange arrows). (d) SEM image of the thermal conductance measuring device, with suspended heating (red) and sensing (blue) membranes. The device measures and controls the temperature with an accuracy of 10 mK. (e) Zoom-in of the GaP NW bridging the suspended membranes. Electron beam-induced deposited Pt/C improves the thermal contact.

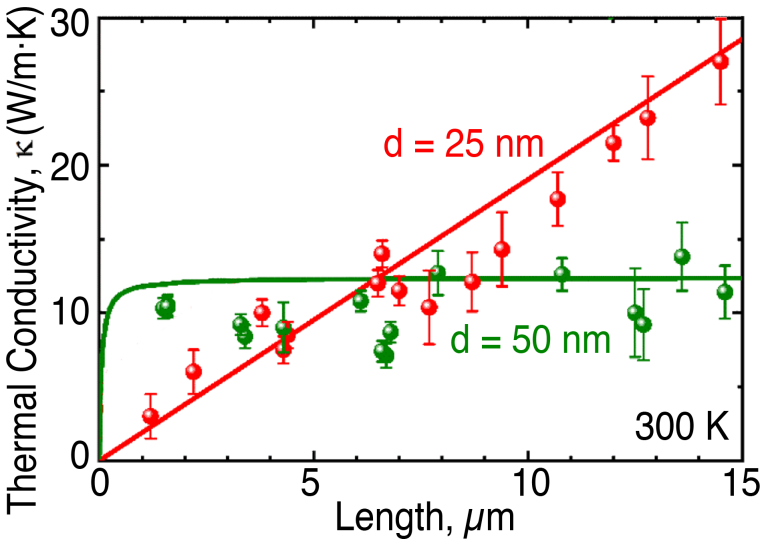

Figure 2. Room-temperature thermal conductivity κ of GaP NWs with *d* = 25 and 50 nm. Lines are based on Landauer's theory assuming negligible specular phonons for d = 50 nm NWs and negligible diffusive phonons for d = 25 nm NWs. We observe room-temperature axial ballistic heat flow in ultrathin, 25 nm diameter, GaP NWs up to wire lengths of at least 15 μm, and a sharp transition to diffusive heat flow when the diameter is doubled to 50 nm.

Ballistic phonon transport may find application in novel cooling solutions for computer chips, which require rapid removal of heat from ever decreasing volumes. Ballistic heat flow could possibly be realized more easily in other compound semiconductors composed of lighter elements than Ga and P, such as Al and N, because of even longer phonon mean free paths.

From Chem 117

Material	Thermal conductivity, W/(K·m)
Air	0.025
PMMA (polymethylmethacrylate)	0.19
Water (liquid)	0.60
Glass	0.85
Ice	2.2
Stainless steel	16
Iron	80.4
Brass (Cu 63%, Zn 37%)	125
Aluminium	237
Copper	401
Diamond	3320

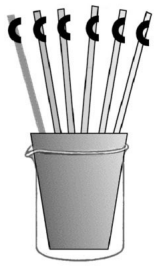

http://en.wikipedia.org/wiki/List_of_thermal_conductivities

LEDs were fabricated with a device structure of PET/AgNWs/ZnO (80 nm)/PEDOT:PSS (40 nm)/$CsPbBr_3$ perovskite emitter (50 nm)/TPBi (40 nm)/LiF (1 nm)/Al (100 nm). In the device, AgNWs/ZnO was used as an anode, PEDOT:PSS as a hole-transport layer, $CsPbBr_3$ perovskite as the green emitter, TPBi as an electron-transport layer and LiF/Al as a cathode, respectively.

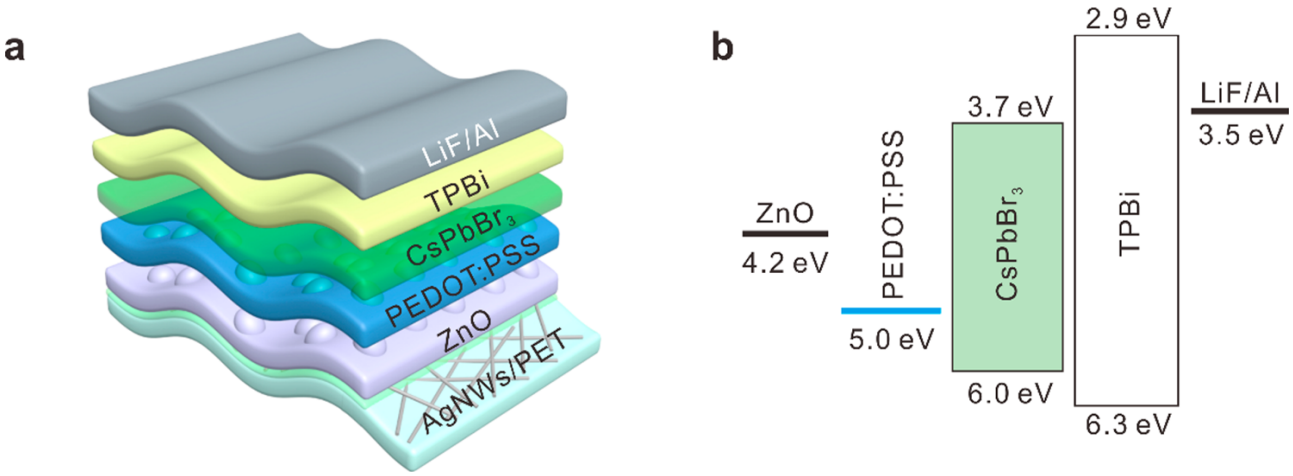

Figure 3. (a) Schematic diagram of the perovskite LED device on a flexible PET substrate with a AgNWs-based composite electrode. (b) Schematic energy-level diagram of the LED.

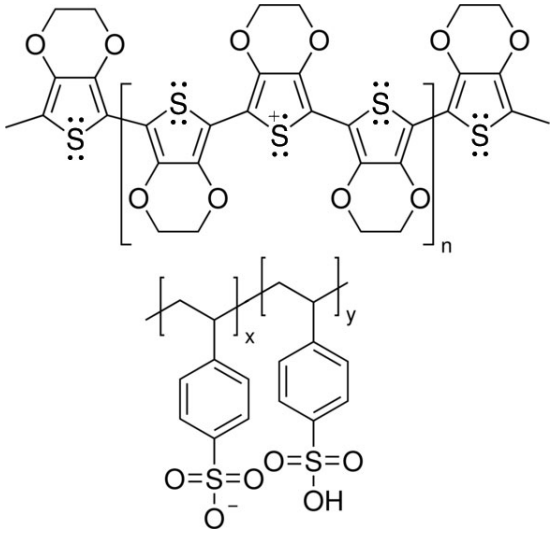

Chemical structure of PEDOT:PSS

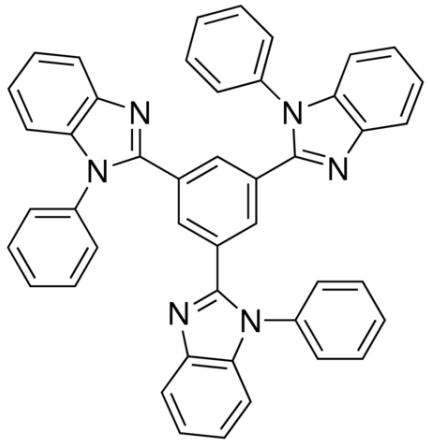

Chemical structure of TPBi.

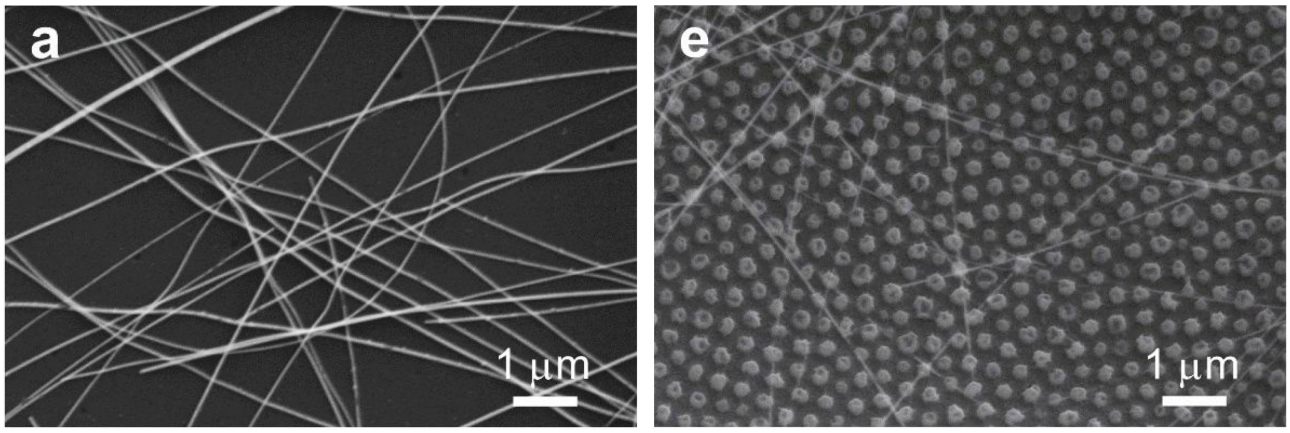

Figure S8. SEM images of (a) AgNWs spin-coated on PET and (e) patterned ZnO on AgNWs.

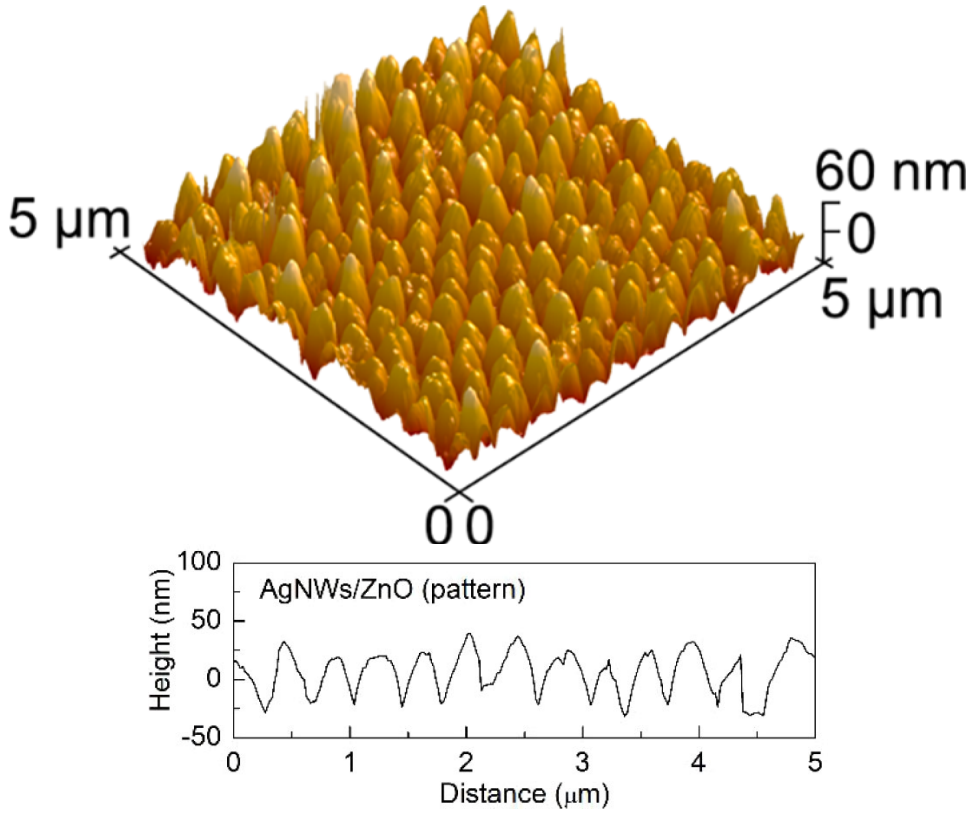

Figure 3. AFM of the patterned ZnO layer. After coating the ZnO sol–gel precursor on AgNWs and heating at 150 °C for 20 s, a PDMS mold was pressed in conformal contact on the ZnO film with a constant pressure of 0.5 bar for 30 s and subsequently peeled off. The patterned ZnO film was further annealed for 12 min to complete crystallization.

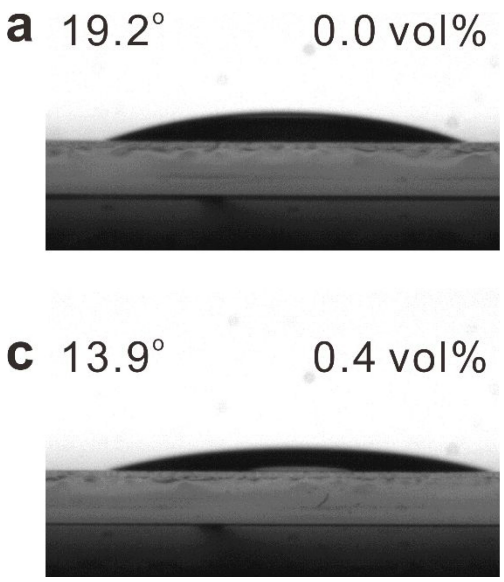

Figure S1. Optical micrographs of a droplet of perovskite precursor solution on the modified PEDOT:PSS with various ETA ratios. A small amount of surfactant (Triton X-100) was mixed into PEDOT:PSS to improve the wetting property.

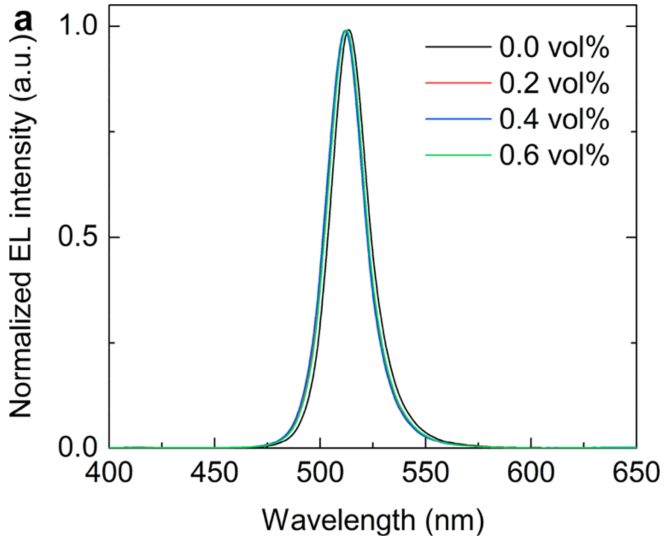

Figure 2. Device performance of LEDs fabricated on ITO with various ethanolamine (ETA) ratios in PEDOT:PSS. (a) Normalized EL spectra under a bias of 4 V.

Figure 4. Photograph of device performance of LED fabricated on PET in operation.

Interpret the figures and text by expanding on what is being illustrated, explaining procedures or techniques, indicating why it might be important or making connections to our class readings and laboratory work. Tell more than rewriting the caption. Try to use your interpretation to demonstrate additional knowledge beyond what is shown here. (**You should write on each page for about 10 minutes**.)

ACS Nano (2019) DOI: 10.1021/acsnano.9b02196

$ZrTe_2$ thin films were grown on a (110) $SrTiO_3$ substrate by the PLD technique. Comparison of the XRD pattern with standard data reveals that the $ZrTe_2$ thin film has a preferred orientation along its *c*-axis.

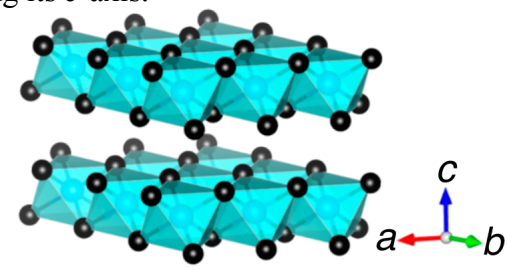

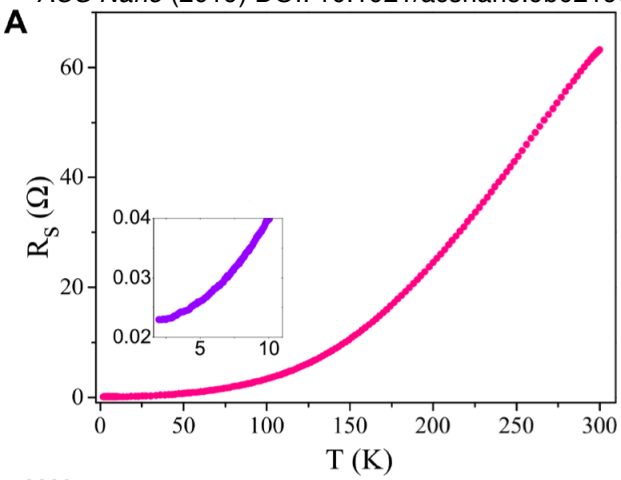

Figure 1. (A) Temperature dependence of the sheet resistance in the $ZrTe_2$ thin film.

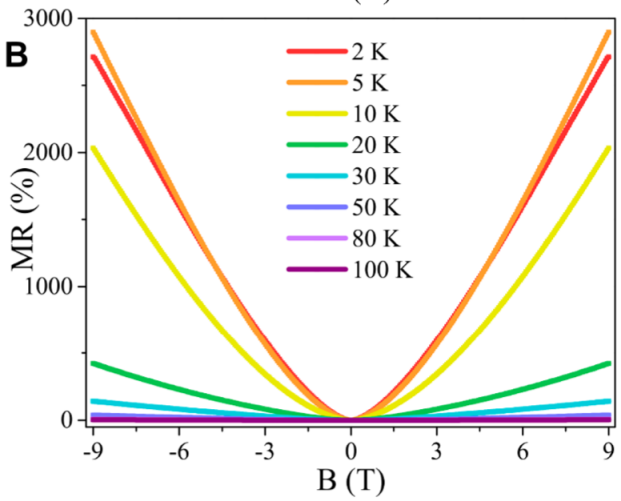

(B) MR of the $ZrTe_2$ thin film at selected temperatures measured with B || *c*-axis.

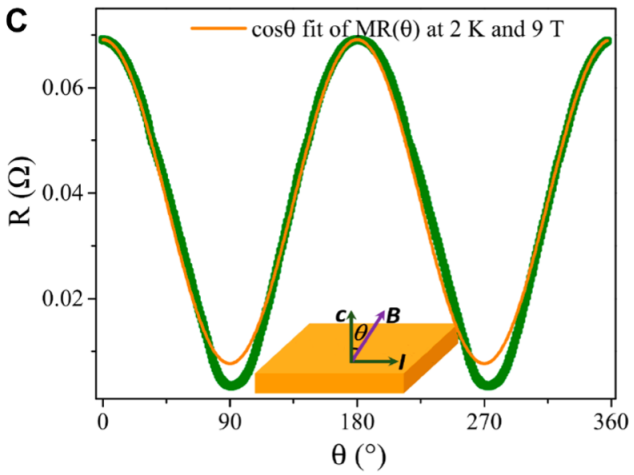

(C) MR as a function of the tilted angle, θ, at T = 2 K and 9 T. θ is the angle between the magnetic field and the *c*–axis.

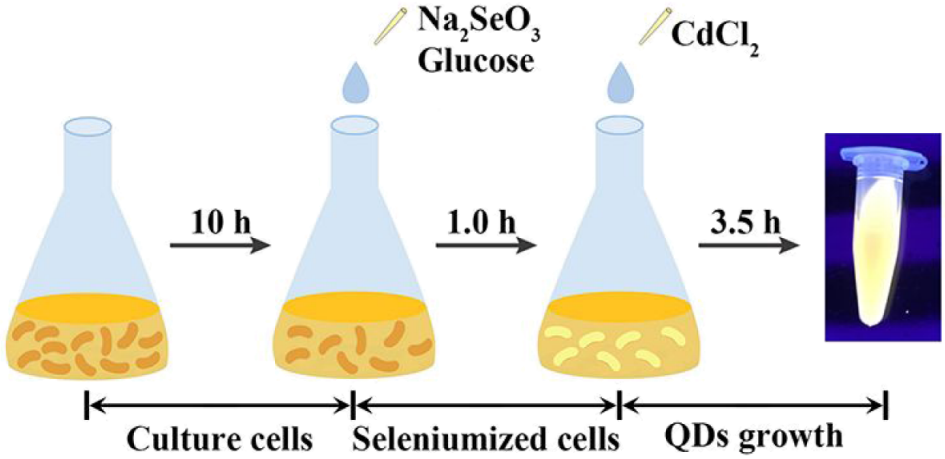

Experimental Section. A single colony of *E. coli* JM109 strain was picked from an agar plate and inoculated in 10 mL of medium overnight. The cultures were diluted by 1:10 with fresh medium and incubated for an additional 10 h. After that, Na_2SeO_3 was added to the medium at a final concentration of 1 mM, and 4 g/L of glucose was added as the substrate. After 1 h of cultivation for seleniumized cells, $CdCl_2$ was dosed to a final concentration of 6 mM. After an additional 3.5 h of cultivation, the *E. coli* cells were collected by centrifugation (6000× *g*, 4 °C, 5 min). All experiments were conducted at 37 °C.

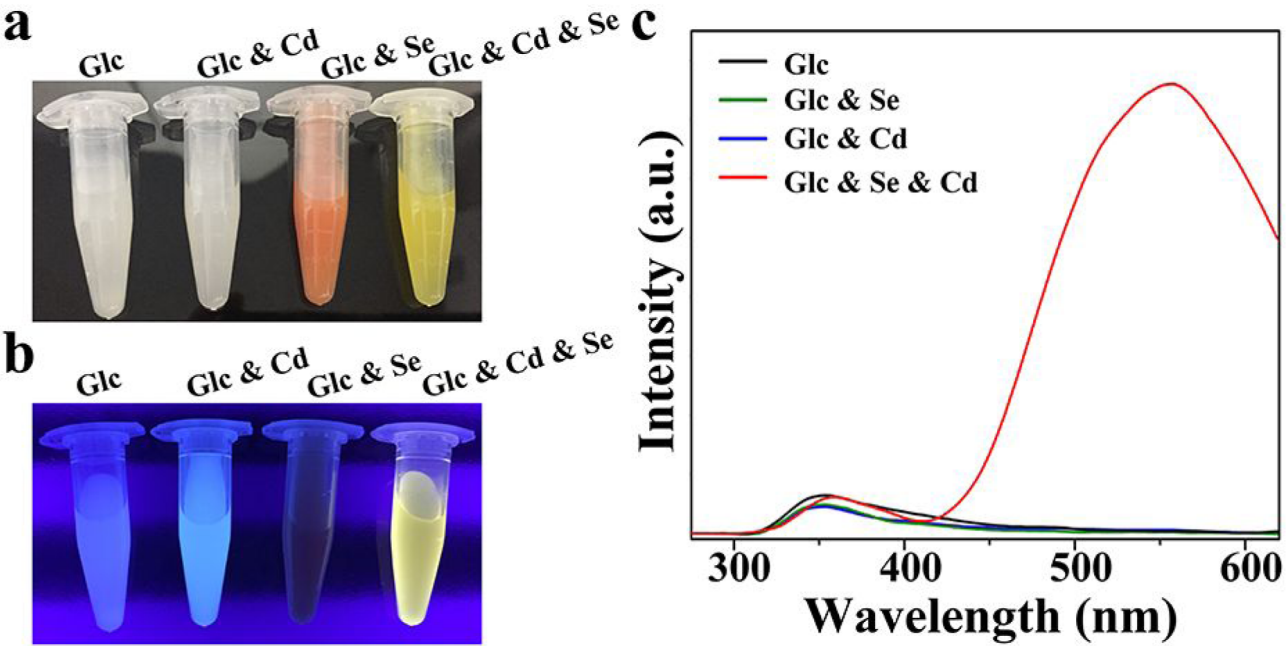

Figure S3. Optical images of treated *E. coli* cells under sunlight (a) and UV irradiation (b). (c) Fluorescence spectra of cells excited by a 310-nm wavelength.

Experimental Methods. CNTs with −COOH groups were dispersed with anhydrous ethanol, followed by ultrasonification for several hours. The suspensions were spread onto a water surface by spray-coating, resulting in a uniform preassembled film formed at the air/water interface. PDMS films were fabricated from Sylgard 184. The PDMS and corresponding cross-linker (the ratio between component A and B was 1:10) were diluted using hexane with a weight ratio of 4% and sprayed onto the surface of the prepared CNT film to achieve a uniform layer, followed by a typical PDMS curing process (at 70 °C for 2h). The film can then be transferred onto arbitrary substrates with excellent self-adhesion.

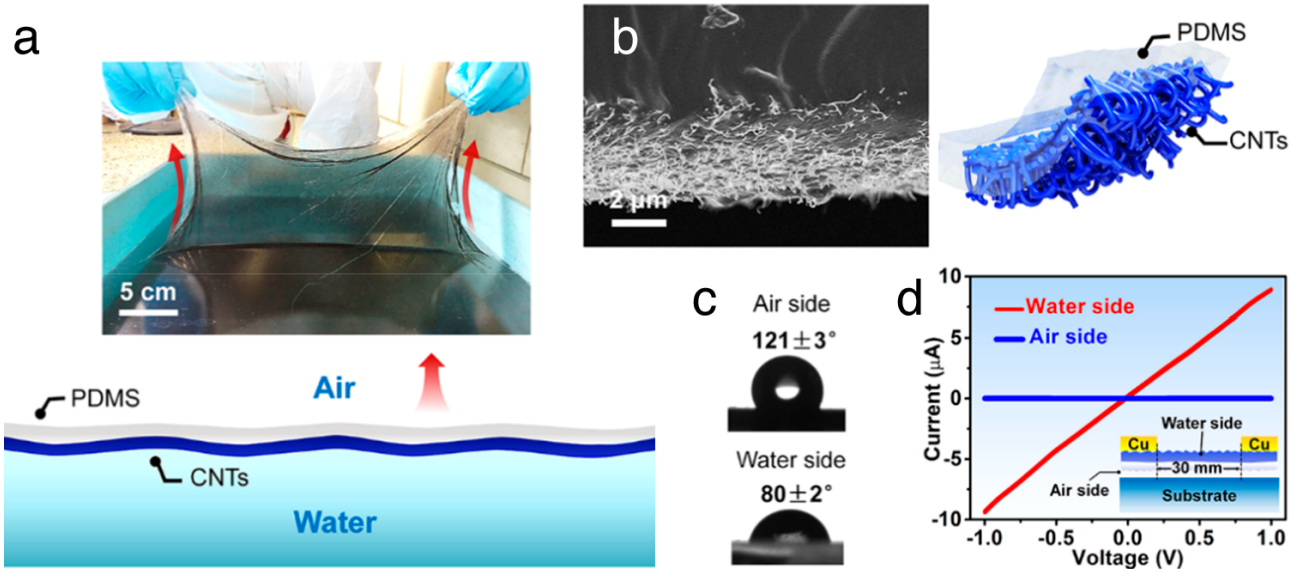

Figure 1. (a) Sketch and photograph of the fabrication of stretchable ultrathin film at an air/water interface. (b) SEM cross-sectional image showing exposed CNT (rough surface) and sketch. (c) Water contact angle for air and water sides of the self-assembled film. (d) Current−voltage curves of the water and air side layers of the hybrid film.

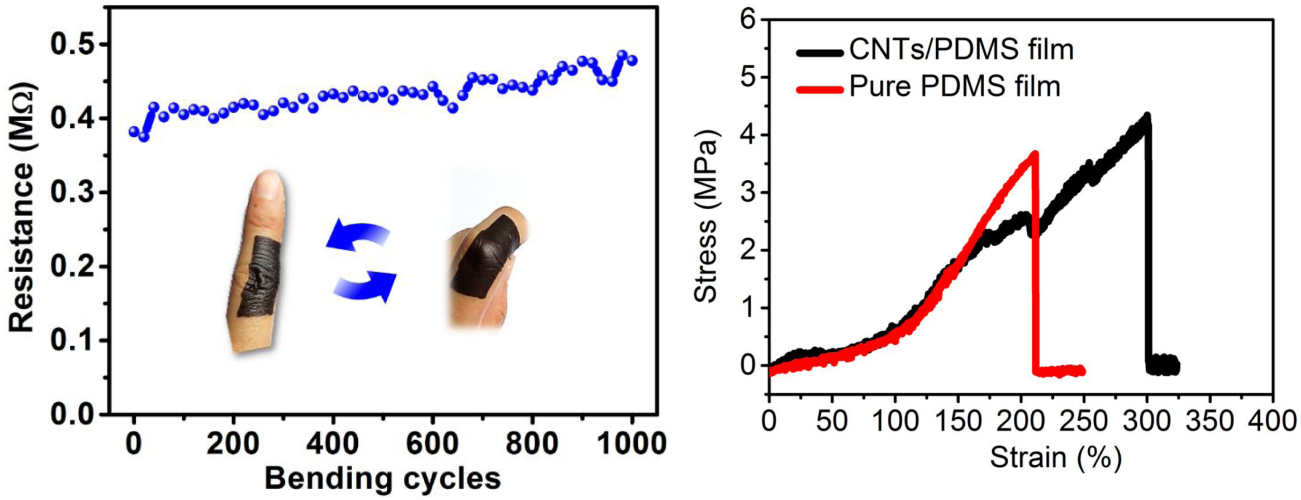

Methods. A diluted AgNW dispersion was spin-coated several times at 1500 rpm for 20 s on a PET substrate, followed by a heating treatment at 100 °C for 5 min. A sol−gel derived ZnO precursor solution was prepared by dissolving zinc acetate dehydrate (Sigma-Aldrich, 99.0%, 220 mg) in a mixture of 2-methoxyethanol (TCL, 99.0%, 2 mL) and ethanolamine (Aladdin, 99.0%, 61 μL) with stirring for 12 h for the hydrolysis reaction under ambient conditions. The ZnO precursor solution was spin-coated several times on the AgNW-coated PET substrate at 3000 rpm for 40 s and then annealed at 150 °C for 10 min to form a dense ZnO film that tightened the AgNW connections. The patterning of moth-eye nanostructures was conducted by soft nanoimprint lithography, where the PDMS mold was prepared as in previous reports. The key feature is a synergetic interplay of a AgNWs-based network for electrical conduction and a moth eye nanopatterned ZnO layer for broadband light trapping. The resulting samples were transferred into a nitrogen-filled glovebox for depositing the PBDB-T ITIC photoactive layers, followed by MoO_3 and Ag layers.

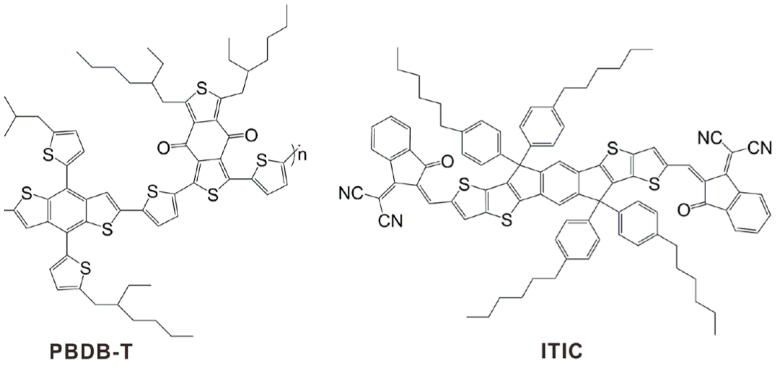

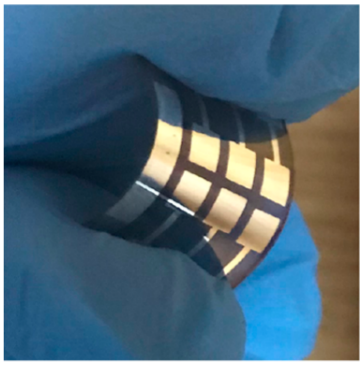

Figure 1. Photograph of the fabricated 11% efficient organic solar cell.

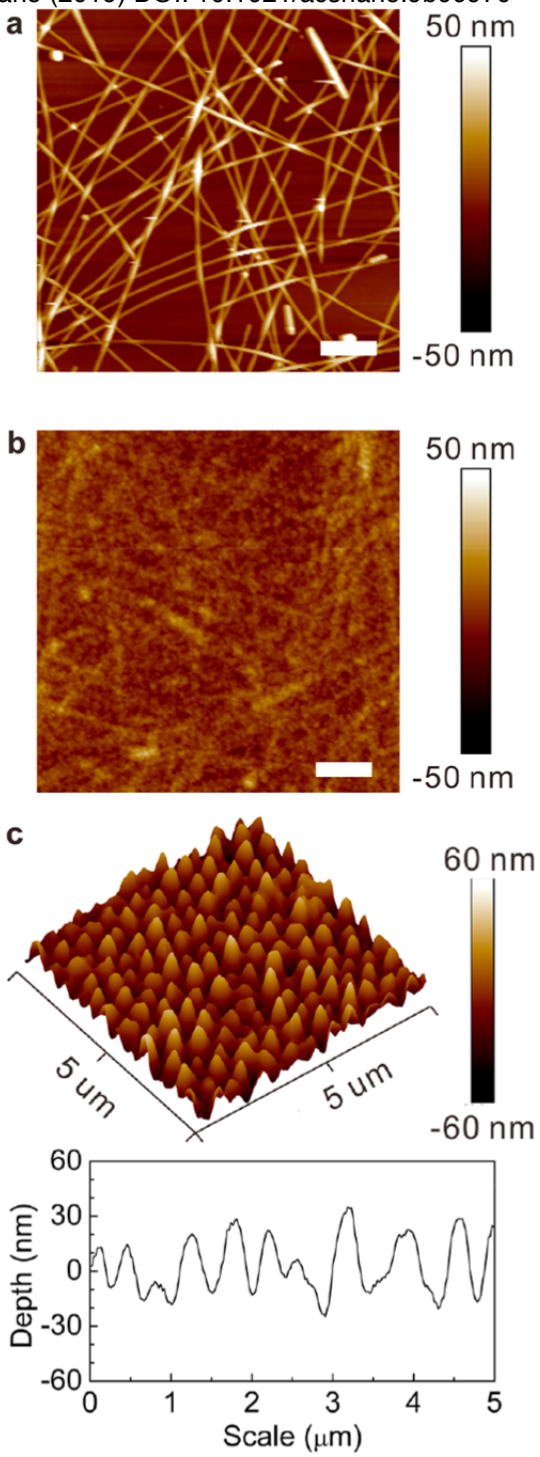

Figure 2. AFM images of (a) bare AgNWs and (b) ZnO coated AgNWs on PET substrates. Scale bar: 500 nm. (c) Larger image showing the previous layer patterned with moth-eye nanostructures.

Synthesis of Au Nanocube. Au NCs were synthesized by a seed-mediated growth method. First, a seed solution was prepared by reducing 0.1 mL of 25 mM $HAuCl_4$ with 0.6 mL of 0.01 M $NaBH_4$ in 7.65 mL of 0.1 M CTAB solution, followed by stirring for 2 min and keeping at 30 °C for 1 h. The obtained seed solution was diluted 10 times by adding 1 mL of seed solution into 9 mL of water. Then, 2.5 μL of diluted seeds was added into a growth solution containing 0.8 mL of 0.1 M CTAB, 0.1 mL of 7 mM $HAuCl_4$, 4 mL water, and 0.6 mL of 0.1 M ascorbic acid. The solution was then kept undisturbed at 30 °C overnight, followed by washing with water after centrifugation at 7830 rpm for 10 min. Thiolated-polystyrene was added to render the nanoparticles hydrophobic and produce polystyrene-capped Au nanocubes.

Capping Au Nanospheres with DNA. Au nanospheres were reacted with thiol-terminated DNA.

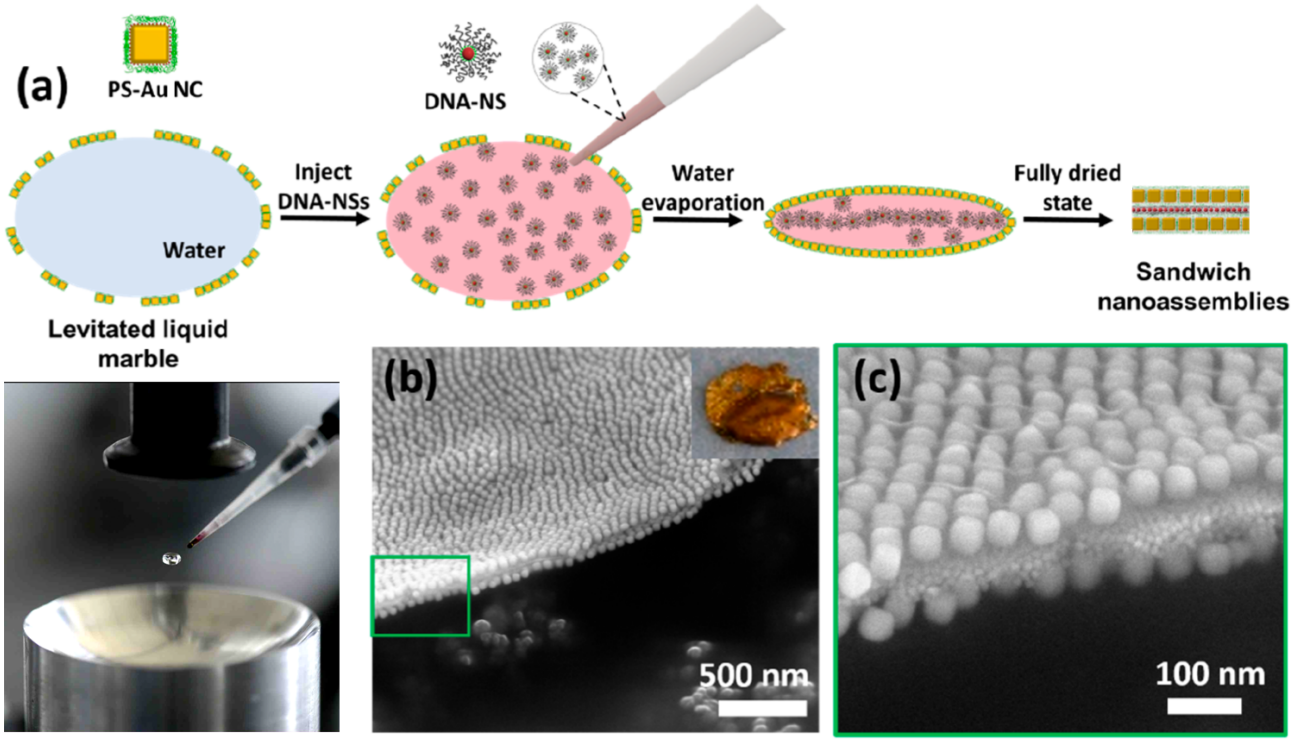

Figure 3. Levitation mediated self-assembly of a sandwich nanoassembly with DNA-NSs inside. (a) Schematic representation of the assembly of a sandwich nanoassembly by injecting concentrated DNA-NSs suspension as shown in photograph. (b, c) SEM images of the cross-section of a sandwich nanoassembly showing DNA-NSs located between two layers of Au NC nanoassemblies, inset shows the image of a whole piece of sandwich nanoassembly.

Interpret the figures and captions by expanding on what is being illustrated, explaining procedures or techniques, indicating why it might be important or making connections to our class readings and laboratory work. Tell more than rewriting the caption. Try to use your interpretation to demonstrate additional knowledge beyond what is shown here. (**You should write on each page for about 10 minutes**.)

All figures on this page are from *ACS Nano* (2018) DOI: 10.1021/acsnano.7b08294

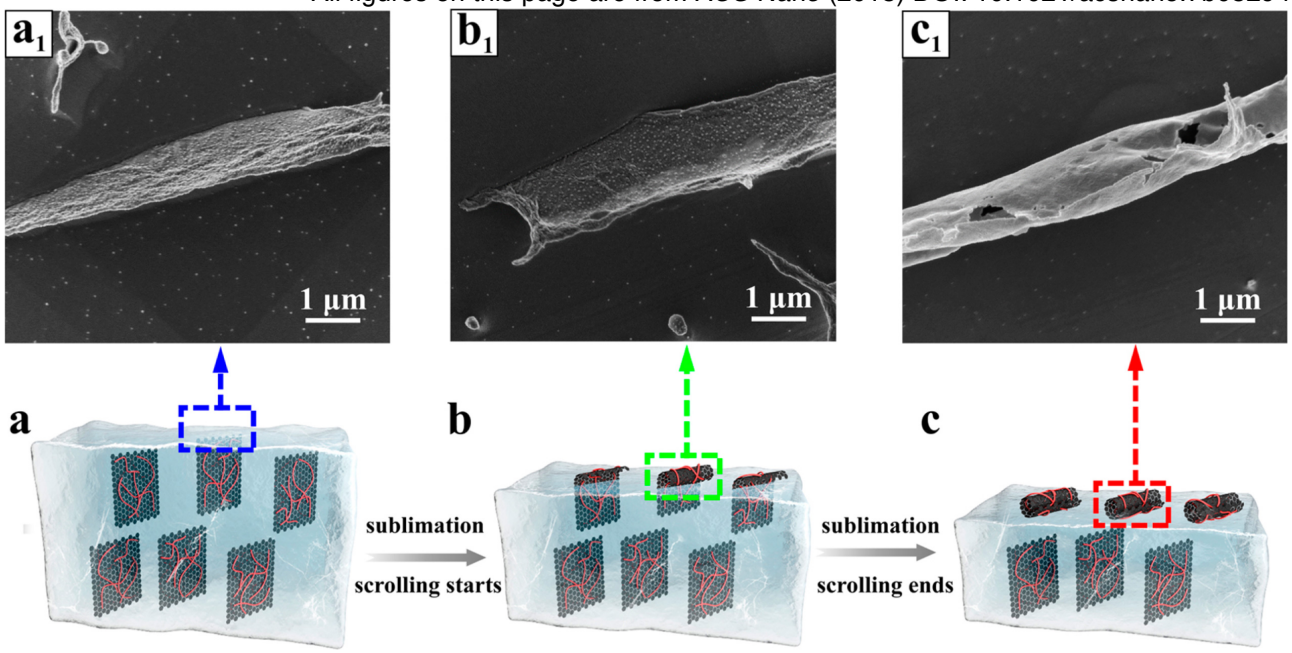

Figure 3. Schematic and cryo-SEM images of the scrolling behavior from PSS-rGO nanosheets to nanoscrolls. Poly(sodium *p*-styrenesulfonate) with a benzene ring and -SO_3^- groups is used to prepare a GO aqueous dispersion which is then reduced with hydrazine hydrate. Without the PSS, stacked rGO layers are formed instead of nanoscrolls. (a) The dispersion is poured into a glass bottle and immersed in liquid nitrogen to become a fast frozen solid; the PSS-rGO nanosheets vertically align in the ice. (b, c) Sublimation of the ice produces spontaneous scrolling of the nanosheets.

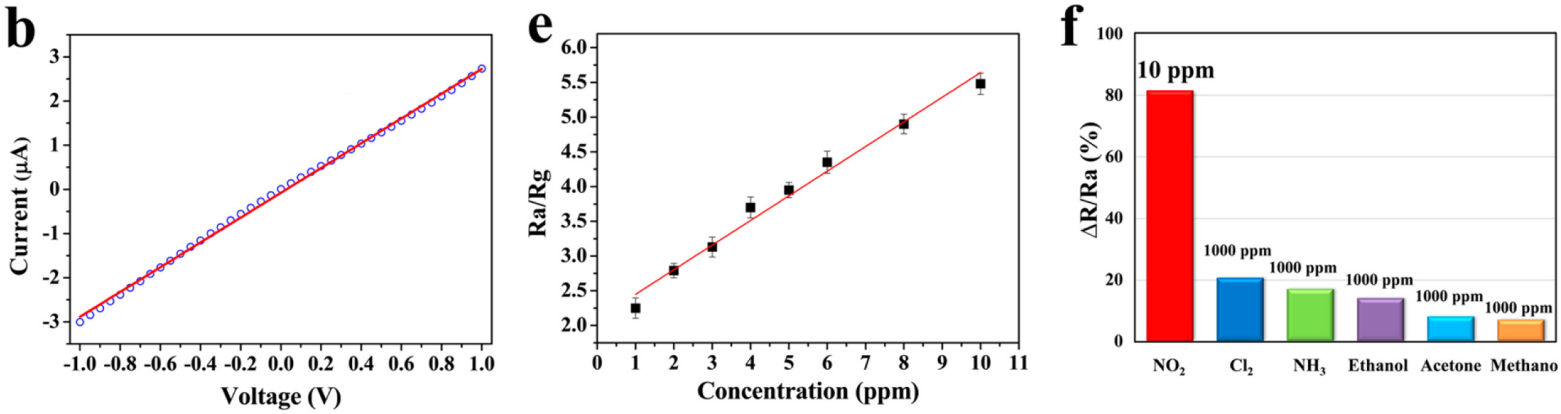

Figure 4. A drop and dry method was adopted to fabricate gas sensors on Ag−Pd interdigitated electrodes supported by a ceramic substrate. (b) After drying, resistance was measured for the thin sensing film. The resistance in air relative to the resistance in another gas (e) depended linearly on the presence of NO_2 and (f) was selective against higher concentrations of other gases.

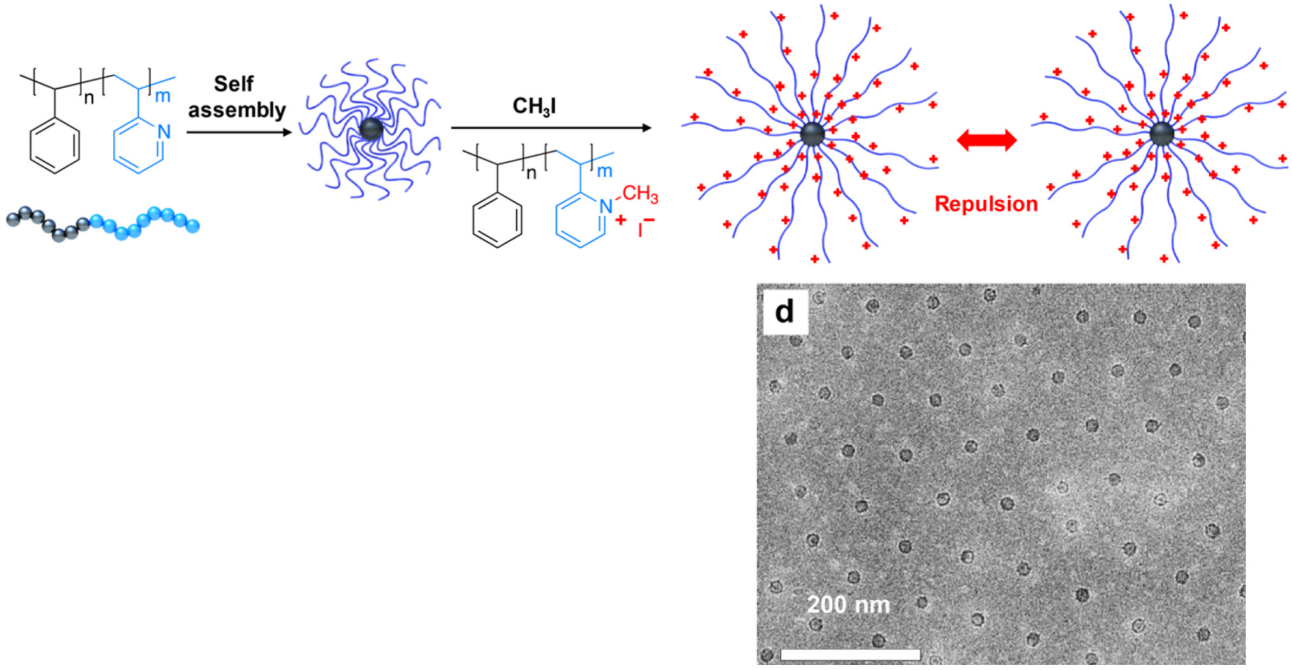

Figure 1. Schematic for preparation of PS-**b**-P2VP micelles for photonic lattices. (d) TEM image.

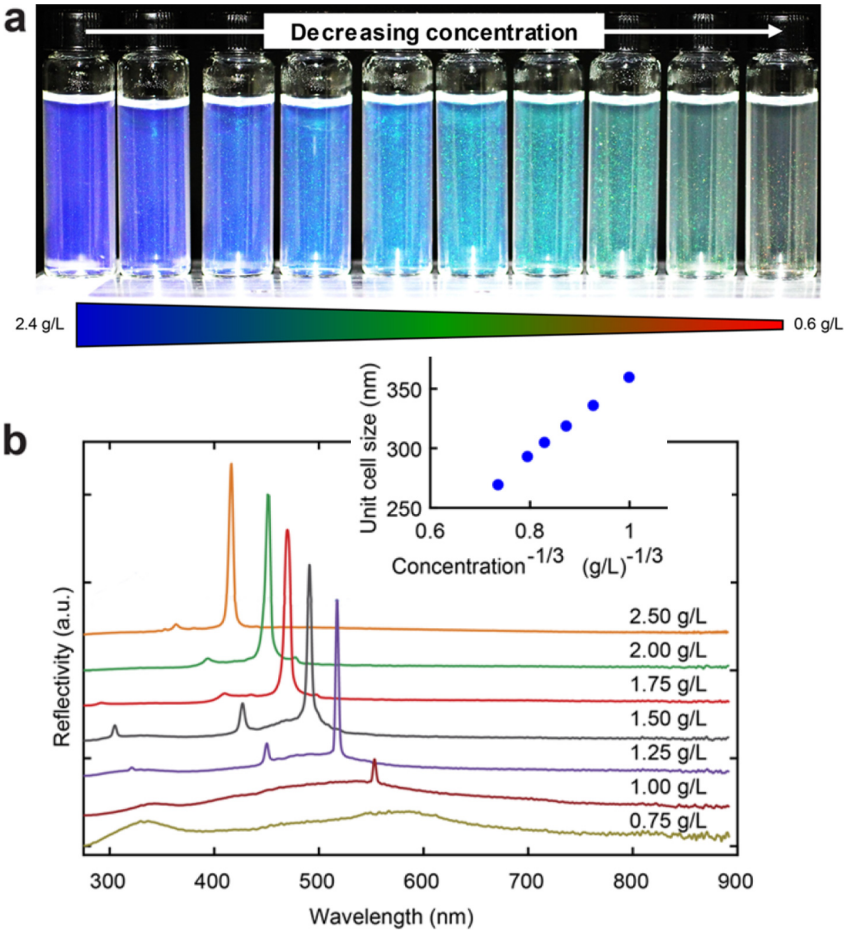

Figure 4. Concentration dependence of structural color for PS-**b**-P2VP micellar photonic crystals. (a) Photographic series for c = 2.40−0.60 g/L in 0.20 g/L increments displaying structural colors. (b) Spectra for different c. Inset: The unit cell size, a, as a function of $c^{-1/3}$.

All figures on this page are from *ACS Nano* (2018) DOI: 10.1021/acsnano.8b00140

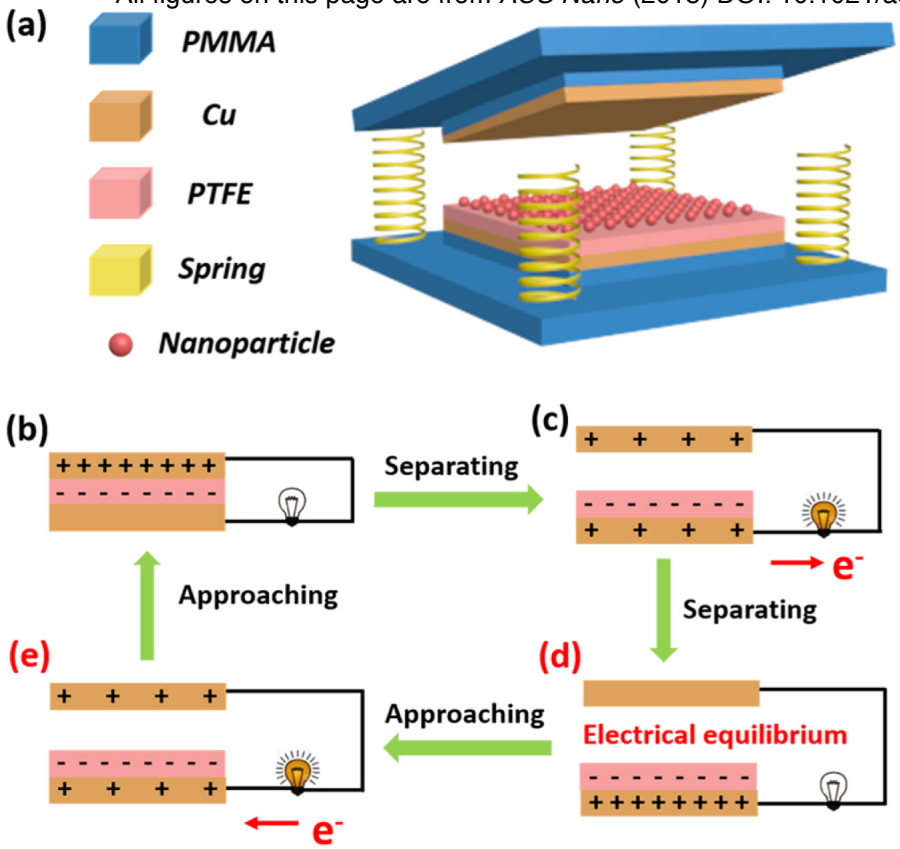

Figure 1. Schematic diagram (a) and operation principal of the TENG (b–e). Contact or friction between the PTFE and copper film transfers electrons, which flow after separation back to the initial state. As force once again is applied, the electrons flow in a reverse direction until the two surfaces fully contact each other, starting another cycle.

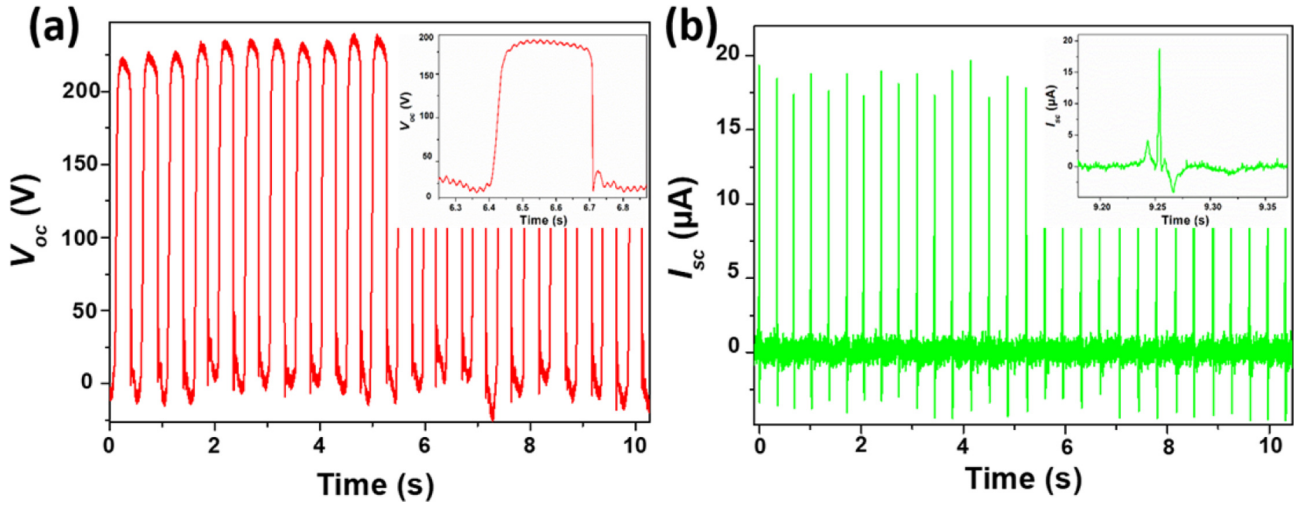

Figure 3. Output performance of the TENG (4 cm x 4 cm with 1.0 cm spacing. triggered by a hand with stable applied force.

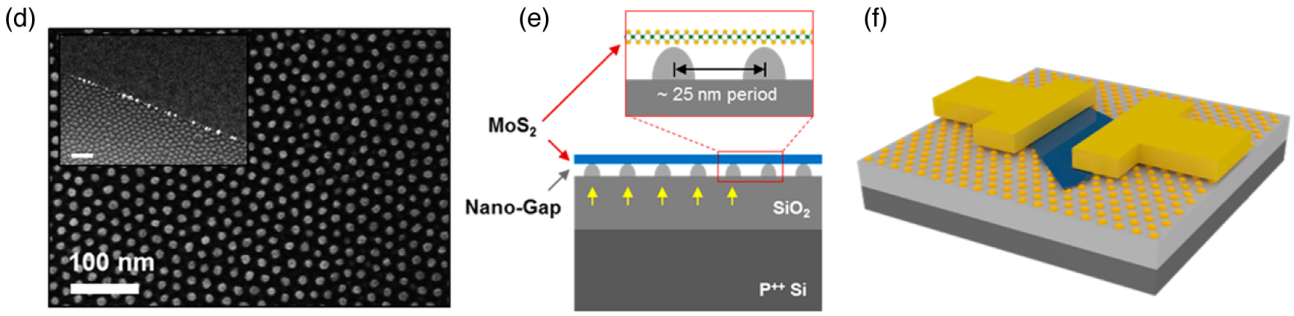

Figure 1. (d) SEM image of fabricated SiO_2 nanostructures. (e) The yellow arrows indicate the locations of nanostructures fabricated by self-assembly of PS-**b**-PDMS, plasma oxidation to convert PDMS microdomains to SiO_x nanostructures, and transfer of MoS_2 mechanically exfoliated from bulk crystals using a conventional Scotch tape method, in order to create a nanogap between MoS_2 and the basal plane. (f) Schematic of the device used for the measurements in Figures 5 and 6. Photoresist was spin-coated and after conventional photolithography an 80 nm Au layer was deposited by thermal evaporation.

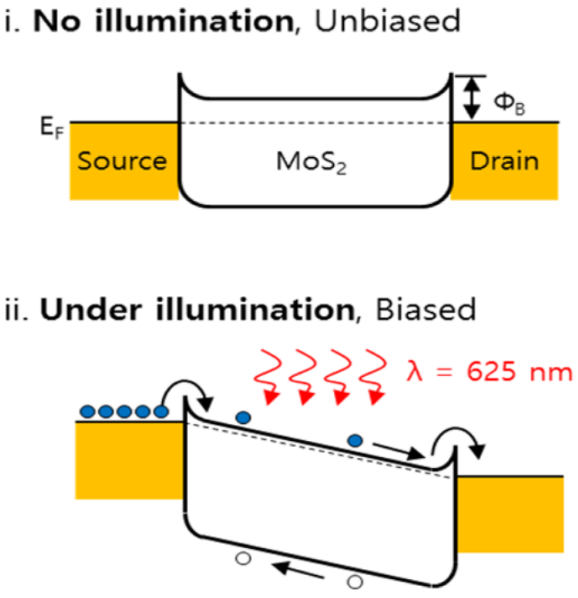

Figure 5. Band structure change of the device upon light illumination.

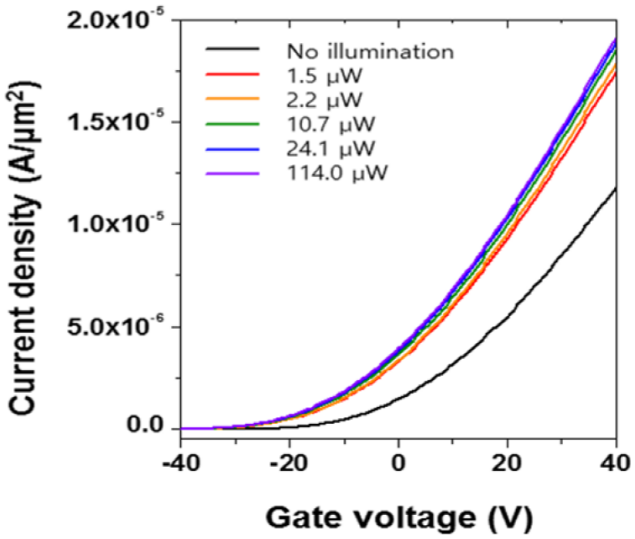

Figure 6. Current density dependence on gate voltage and illumination laser power for the MoS_2 FET.

Interpret the figures by expanding on what is being illustrated, explaining procedures or techniques, indicating why it might be important or making connections to our class readings and laboratory work. Tell more than rewriting the caption. Try to use your interpretation to demonstrate additional knowledge beyond what is shown here. (**You should write for about 10 minutes on each page**.)

All figures on this page are from Nano Lett (2017) DOI: 10.1021/acs.nanolett.7b00754

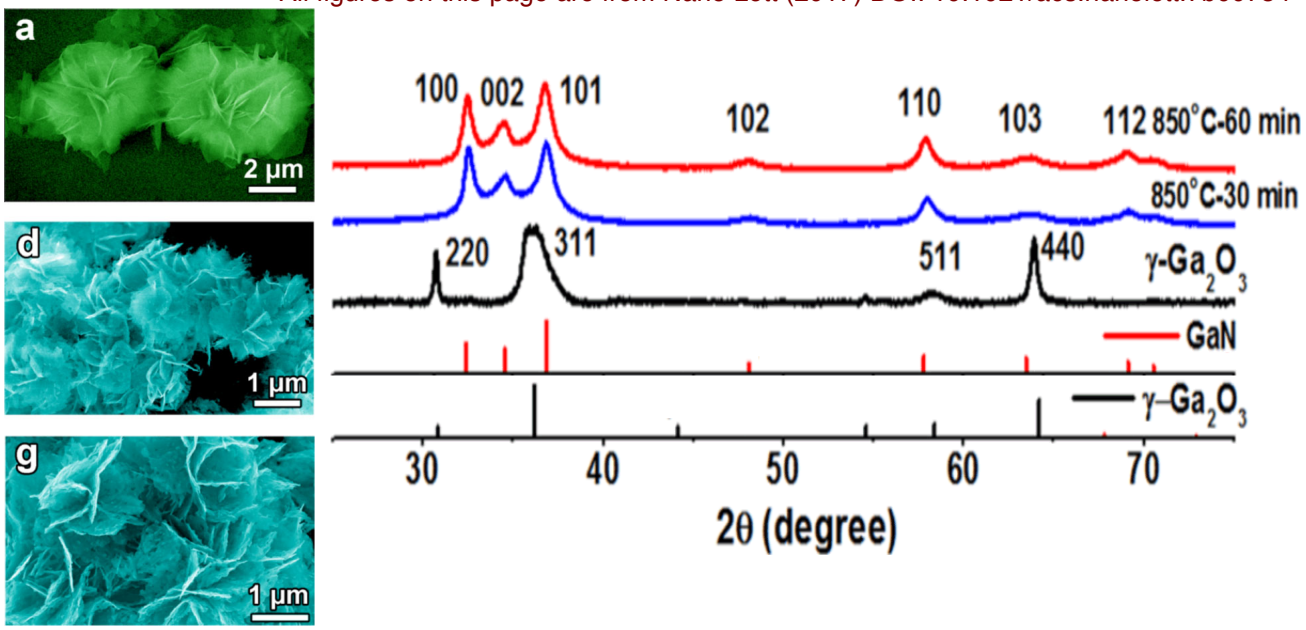

Figure 3. (Left) Typical SEM image of flower-like γ-Ga_2O_3 nanosheets and TEM images of thin GaN nanosheets obtained by reaction with NH_3 gas (100 sccm) at 850 °C for 30 and 60 min.
(Right) XRD patterns of γ- Ga_2O_3 nanosheets and GaN nanosheets nitrified at 850°C for 30 and 60 min.

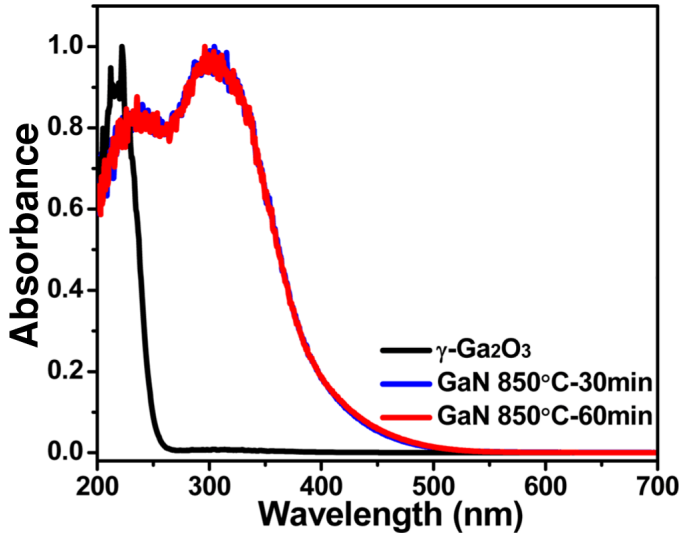

Figure 5. UV−vis spectra of γ- Ga_2O_3 and GaN nanosheets synthesized at 850 °C with different times.

All figures on this page are from ACS Nano (2017) DOI: 10.1021/acsnano.7b00805

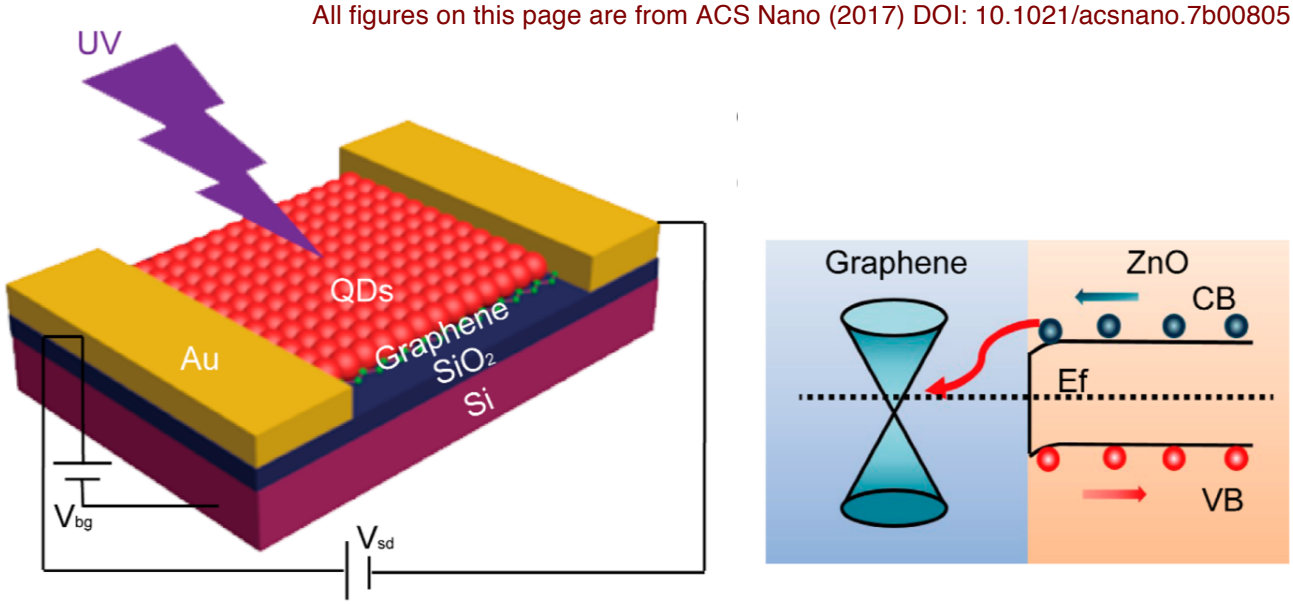

Figure 1. (Left)Three-dimensional view of the ZnO QD/GFET nanohybrid photodetector. (Right) Energy level diagram of ZnO QDs/GFET heterojunctions and charge-transfer process under UV illumination.

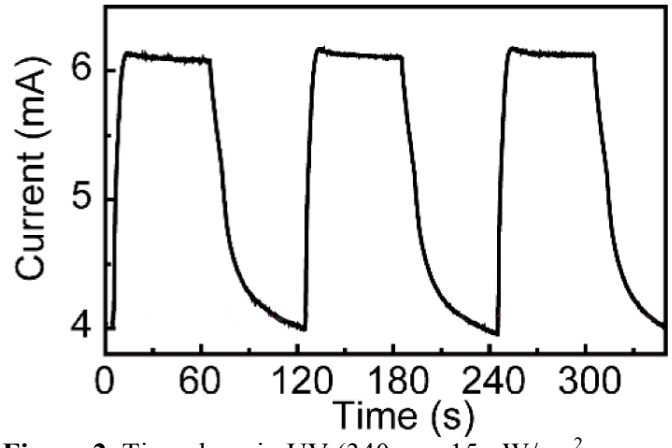

Figure 2. Time domain UV (340 nm, 15 μW/cm^2, zero gate voltage) photoresponse of the ZnO QD/GFET device.

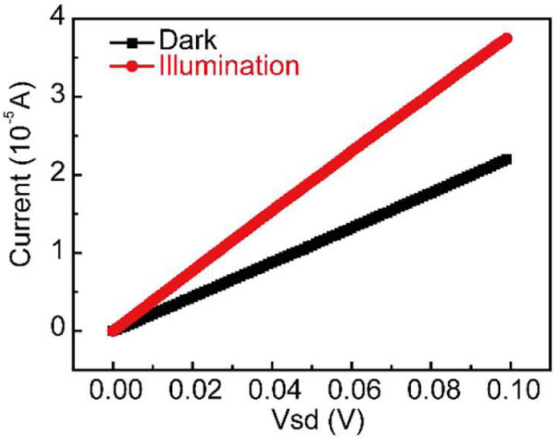

Figure S3. I-V curves for ZnO QD/GFET device under dark and illumination (2.5 μW/cm^2, 340 nm).

All figures on this page are from ACS Nano (2017) DOI: 10.1021/acsnano.7b00304

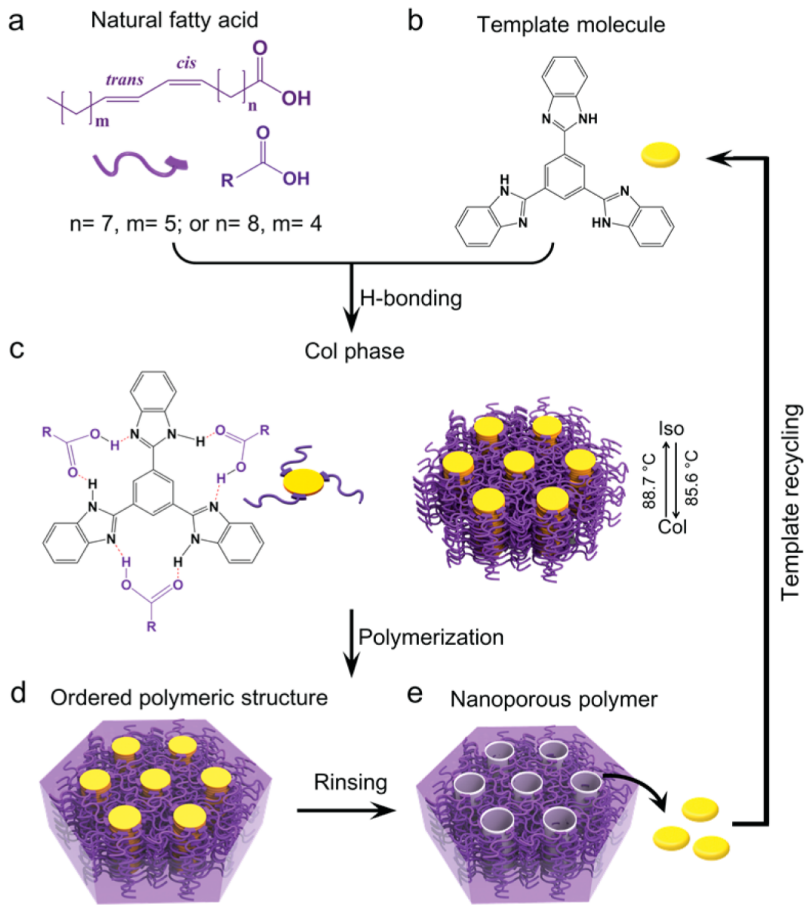

Figure 1. (a) Molecular structures of polymerizable conjugated linoleic acid fatty acid (CLA). (b) Molecular structure of the template molecule 1,3,5-tris(1*H*-benzo[*d*]imidazol-2-yl)benzene (TBIB). (c) Supramolecular complex TBIB/$(CLA)_3$ formed by fatty acids and the template molecule and its self-assembled Col_h mesophase. (d) Mesophases containing a small amount (~1 wt %) of the radical photoinitiator 2-methoxy-2-phenylacetophenone polymerized by exposure to 365 nm UV light. (e) Nanoporous polymer obtained after removing the template TBIB molecules. The TBIB can be recycled and reused for subsequent fabrication.

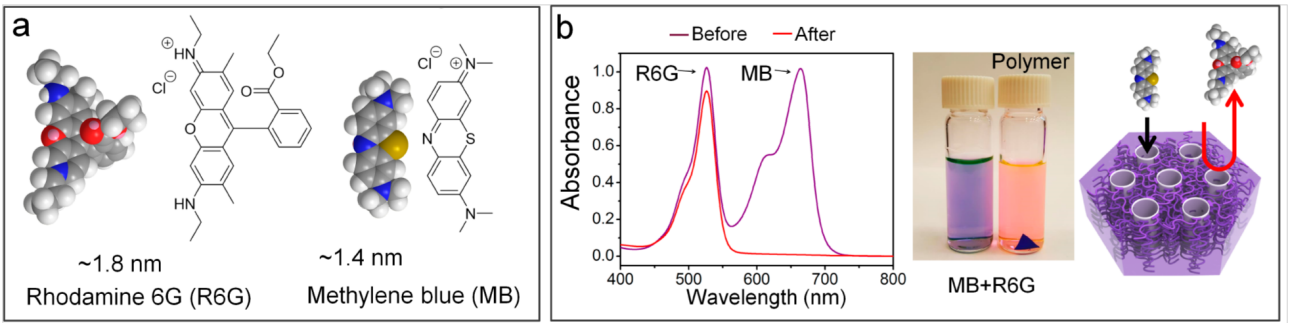

Figure 6. (a) Molecular structures and space-filling models of Rhodamine 6G (R6G) and methylene blue (MB). (b) Selective adsorption of MB into nanopores (~1.2−1.5 nm diameter) from a solution of MB and R6G as confirmed by UV−vis spectra and a color change of the solution.

ACS Nano (2017) DOI: 10.1021/acsnano.7b01217

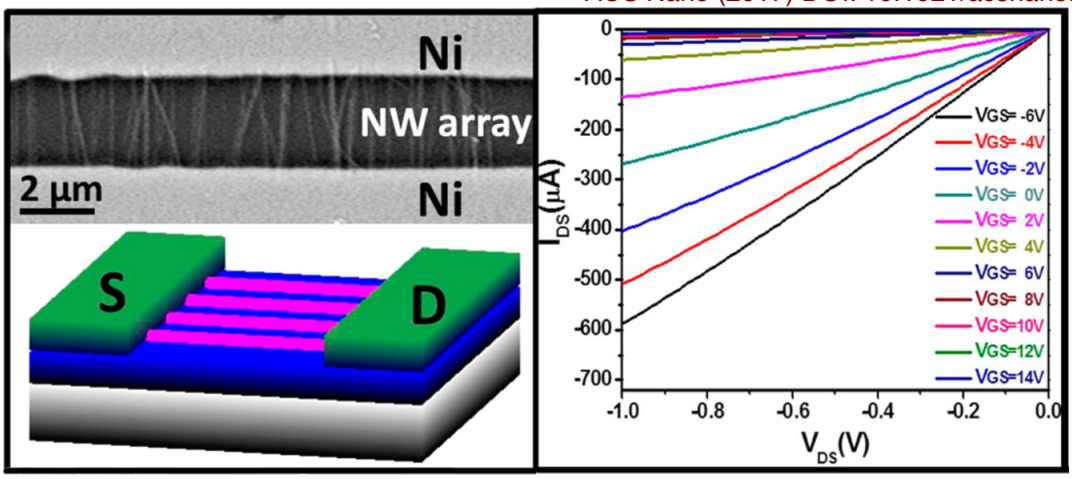

Figure 6. Electrical characterization of typical Pd-catalyzed GaSb NW parallel-arrayed FET.

Nano Lett (2017) DOI: 10.1021/acs.nanolett.6b05241

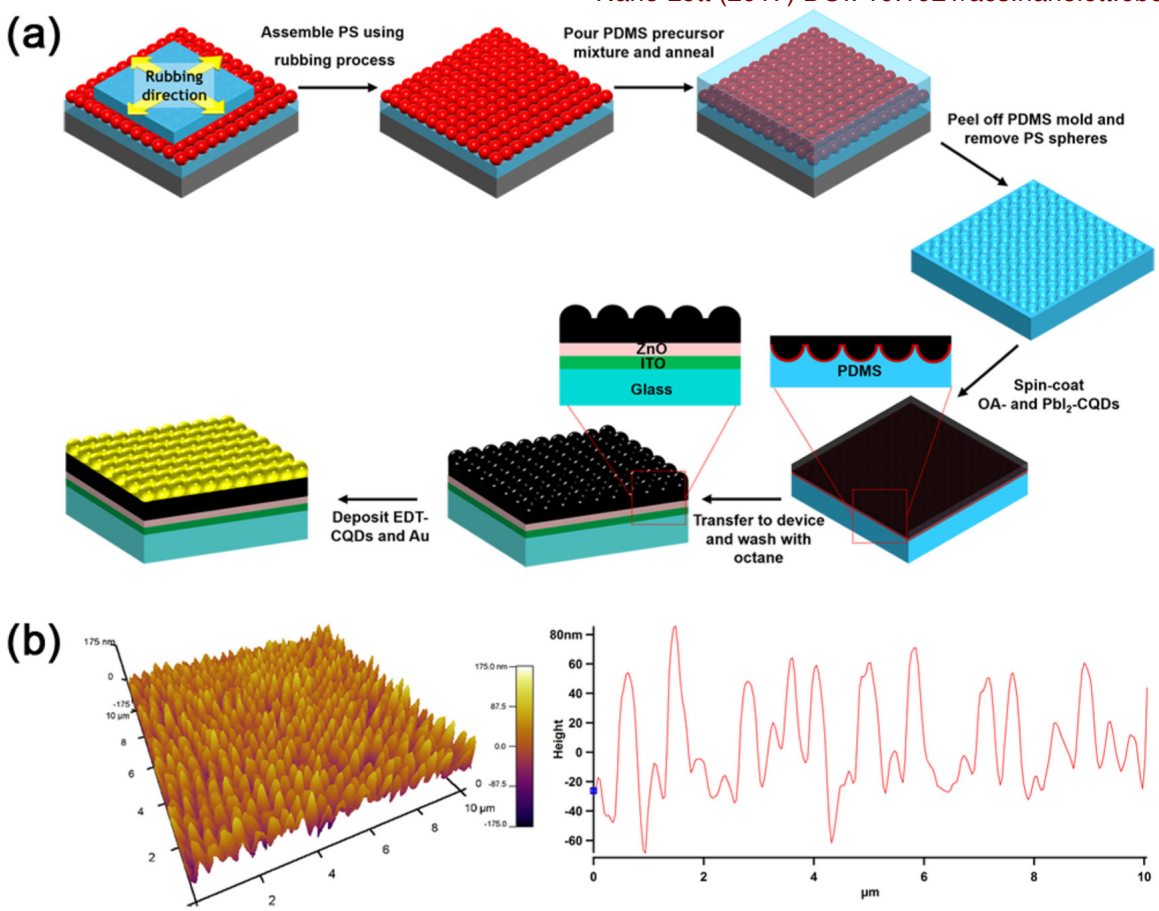

Figure 1. (a) Schematic illustration of the fabrication of patterned PDMS mold and nanostructured CQD solar cells. (b) AFM image and line profile of the nanostructured CQD film.

Chem 150 **Second Test** April 27, 2016

Interpret the figures by expanding on what is being illustrated, explaining procedures or techniques, indicating why it might be important or making connections to our class readings and laboratory work. Tell more than rewriting the caption. Try to use your interpretation to demonstrate additional knowledge beyond what is shown here. **All the figures on a given page are from the same paper EXCEPT FOR THIS PAGE.**

Nature Chemistry (2016) DOI: 10.1038/nchem.2438

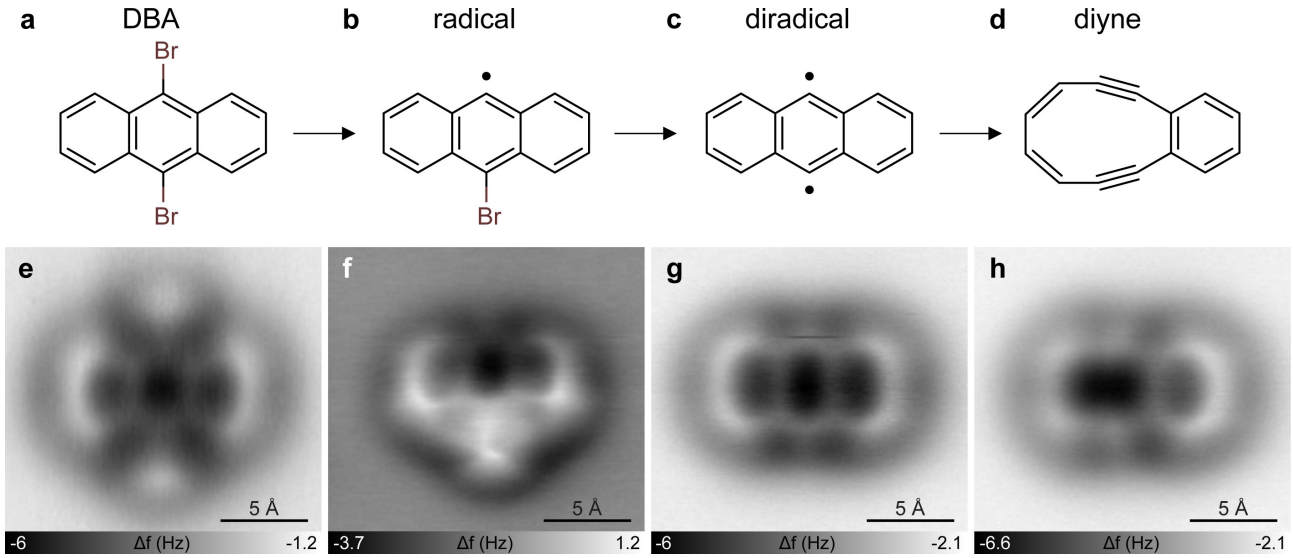

Figure 2. Structures and AFM imaging of the starting material, reaction intermediates and product. **a-d** Chemical structures of the reaction products formed by successive STM-induced debromination of 9,10-dibromoanthracene (DBA) and subsequent retro-Bergman cyclization. **e-h** Corresponding constant-height AFM images of the molecules in a-d on NaCl(2ML)/Cu(111) using a CO tip.

J. Opt. 18 (2016) 033001

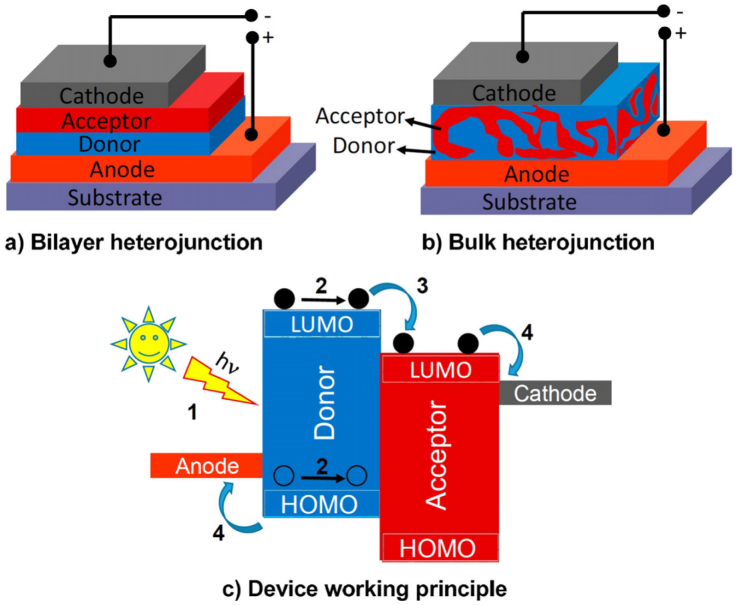

Figure 1. Schematics of (a) bilayer and (b) bulk heterojunction organic photovoltaic devices and (c) their operating principles. Organic solar cells rely on a heterojunction resulting from the contact of a donor and an acceptor material. Absorption of solar photons creates excitons, which diffuse to the donor/acceptor interface, where they are dissociated into free holes and electrons by the electric field.

AuNW Synthesis. 39 mg of $HAuCl_4 \cdot 3H_2O$ were dissolved in a mixture of 5.8 mL of *n*-hexane and 1.7 mL of oleylamine. 1.5 mL of triisopropylsilane were added and the solution was kept undisturbed at RT overnight. The wires were precipitated by adding ethanol. The supernatant was removed, and the wires were redispersed in *n*-hexane. The washing step was repeated once, and the wires were finally redispersed in cyclohexane to achieve gold concentrations of 4 and 8 mg/mL, respectively.

Fabrication of PDMS Stamps. The PDMS stamp was prepared using a lithographically fabricated silicon master (size 1 x 1 cm^2). The prepolymer and the cross-linker of a PDMS kit (Sylgard 184, Dow Corning) were mixed in a 10:1 weight ratio and degassed until no air bubbles were visible. The mixture was then poured on the silicon master, which had been silanized with a trichloro(octadecyl)silane.

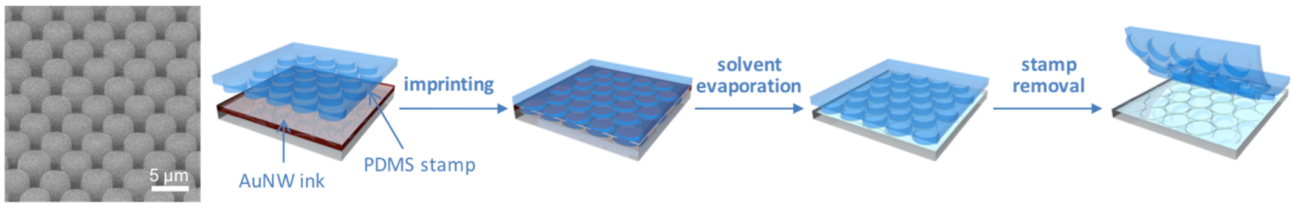

Figure 1. SEM of used PDMS pillar structure and schematic diagram of the nanoimprinting process, which consists of the following steps: 1. spreading of the AuNW ink on a substrate; 2. imprinting using a PDMS stamp; 3. evaporation of the solvent; 4. removal of the stamp.

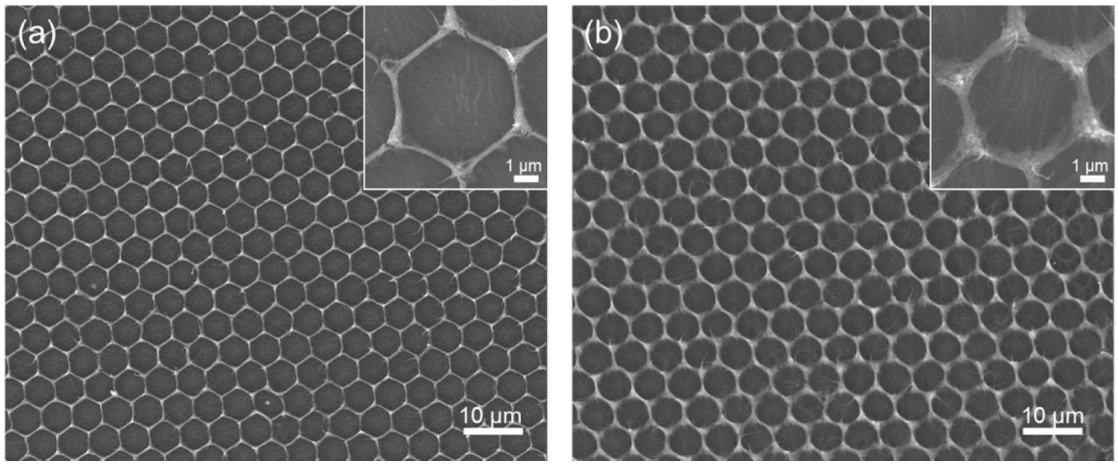

Figure 2. SEM images of imprinted gold nanowires after plasma treatment for (a) low concentration (NM-15 nm) and (b) high concentration (NM-45 nm) of nanowires. Insets show magnifications of bundled nanowires.

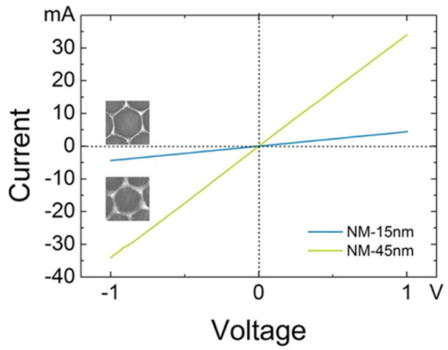

Figure 3. Current−voltage curves for both samples.

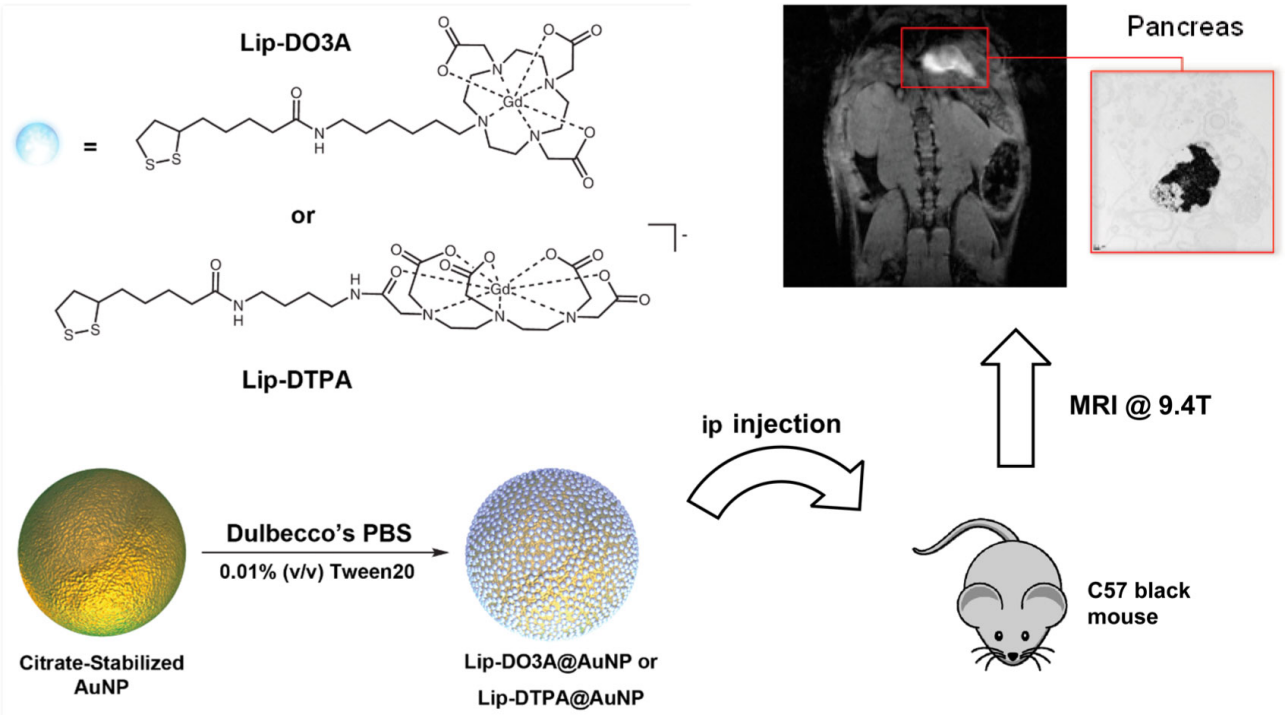

Scheme 1. Gd(III) chelates (Lip-DO3A and Lip-DTPA) were conjugated to the surface of AuNPs to create Lip-DO3A@AuNP and Lip-DTPA@AuNP. These constructs were injected into the ip cavity of C57 black wild-type mice. After 24 h, T1-weighted MR images of the peritoneal cavity were acquired and revealed remarkable accumulation in the pancreas providing significant image contrast. (inset) TEM of fixed pancreatic tissue shows nanoparticle uptake in pancreatic cells.

Preparation of Cs-oleate: Cs_2CO_3 (0.814g) was loaded into 100 mL 3-neck flask along with octadecene (40mL, ODE, Sigma-Aldrich, 90%) and oleic acid (2.5 mL), dried for 1h at 120 ºC, and then heated under N_2 to 150 ºC until all Cs_2CO_3 reacted. Since Cs-oleate precipitates out of ODE at room-temperature, it has to be pre-heated to 100 ºC before injection.

Synthesis of $CsPbBr_3$ NCs: ODE (5 mL) and 0.188 mmol $PbBr_2$ (0.069g) were dried under vacuum for 1h at 120 ºC. Dried oleylamine (0.5 mL) and dried oleic acid (0.5 mL) were injected at 120 ºC under N_2. After complete solubilisation of the $PbBr_2$ salt, the temperature was raised to 140-200 ºC (for tuning the NC size) and Cs-oleate solution (0.4 mL, 0.125 M in ODE) was quickly injected and, 5s later, the reaction mixture was cooled by the ice-water bath. The majority of growth occurs within the first 1−3 s so the size of $CsPbBr_3$ NCs can be most conveniently tuned in the range of 4−15 nm by the reaction temperature (140− 200 °C) rather than by the growth time.

Isolation and purification of $CsPbBr_3$ NCs. Addition of tert-butanol to the crude solution (1:1 by volume) was helpful for precipitation. After centrifugation, the supernatant was discarded and the particles were redispersed in toluene or hexane forming long-term colloidally stable solutions.

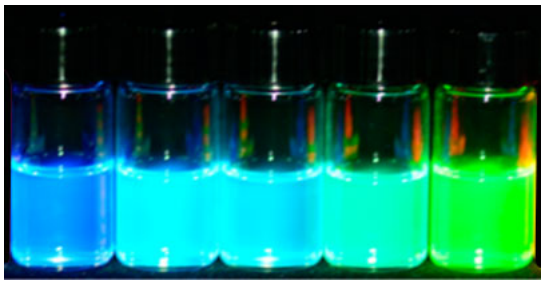

Figure 2. Colloidal perovskite $CsPbBr_3$ NCs in toluene under a UV lamp (λ = 365 nm).

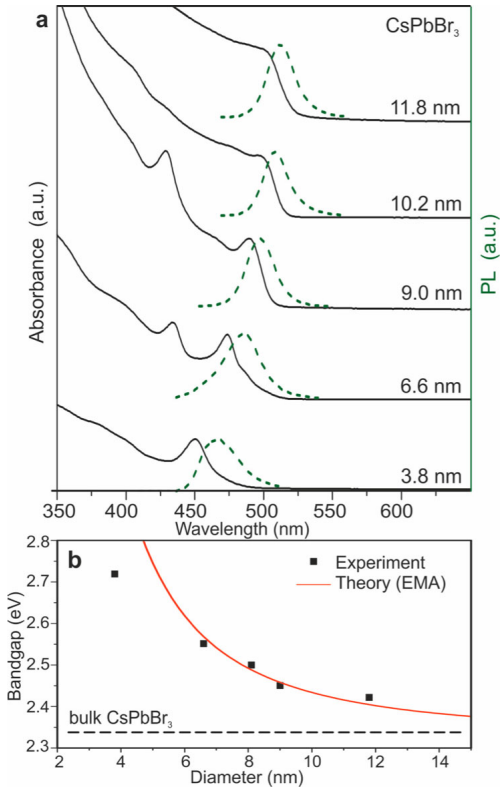

Figure 3. (a) Quantum-size effects in the absorption and emission spectra of 4−12 nm $CsPbBr_3$ NCs. (b) Experimental versus theoretical (effective mass approximation, EMA) size dependence of the band gap energy.

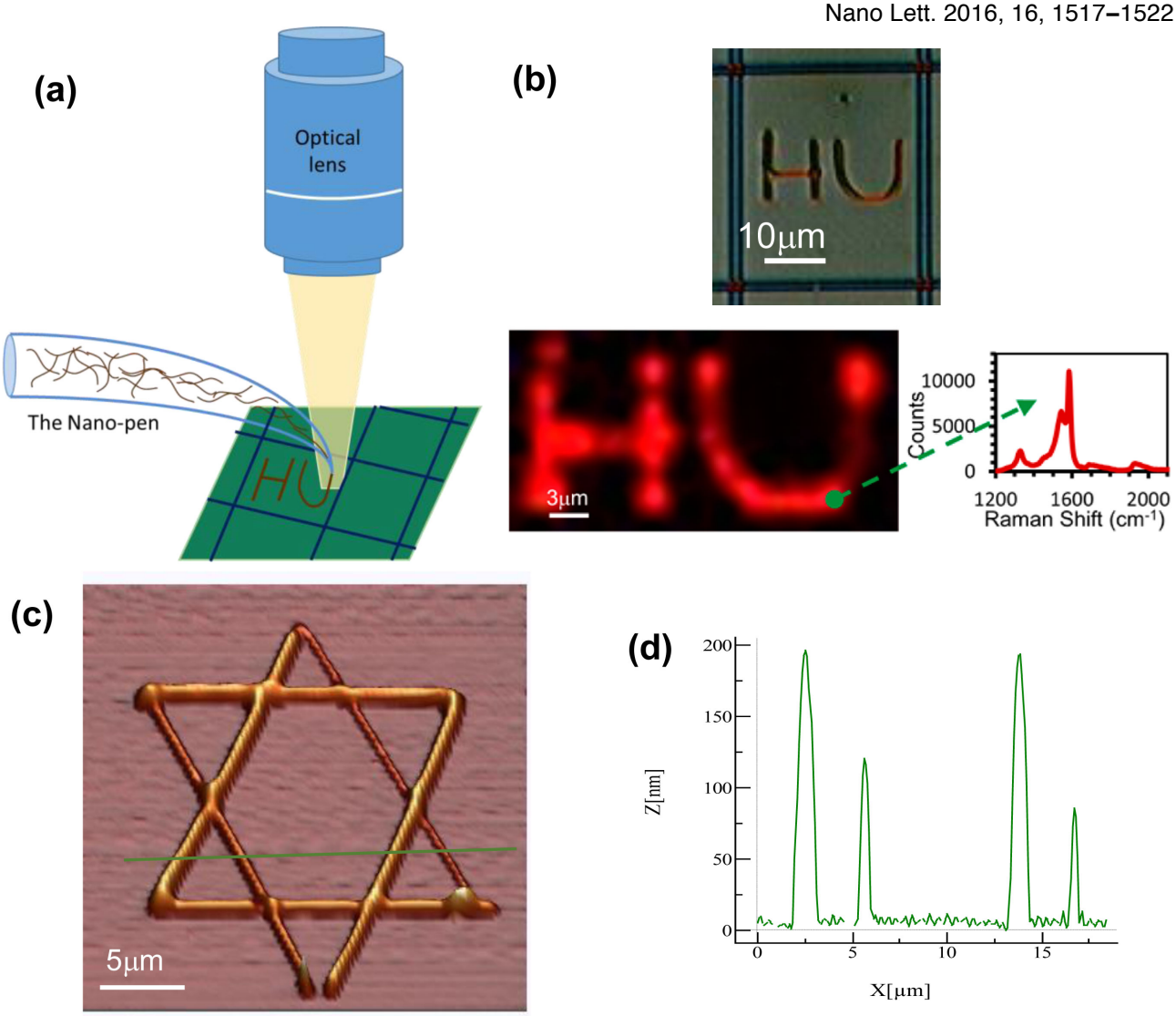

Figure S1. Examples of drawing of complex SWCNT patterns on SiO_2 substrate. (a) Illustration of the nanopen drawing system (Nanonics Imaging Ltd, Jerusalem, Israel). Cantilevered glass probes with AFM sensitivity allow for a complete view of the probe tip which permits a direct view of the drawing with a standard upright optical microscope. (b) This permits transparent integration with spectroscopic methodologies such as Raman for chemical characterization of the drawn structures. Pattern seen through the optical microscope, Raman mapping of the G+ mode of "HU" structure and a Raman spectrum at a point in this image. (c) A 3D AFM of the Star of David with (d) an associated AFM line scan.

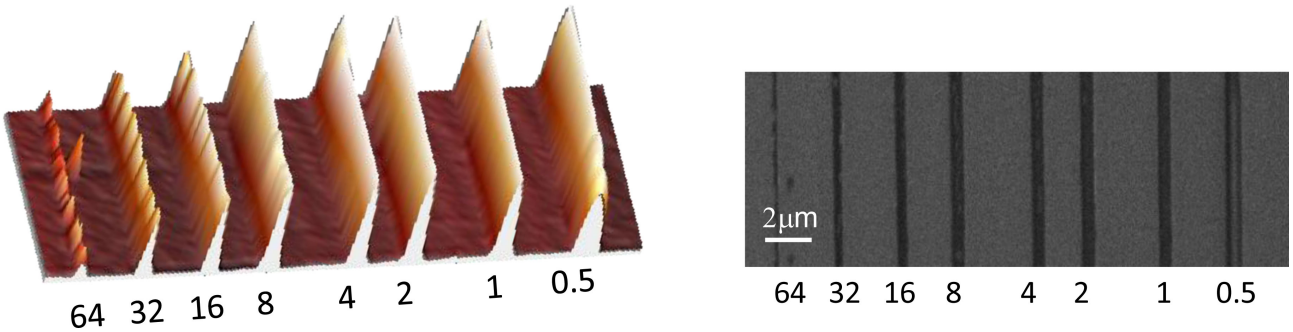

Figure S7. Effect of the drawing speed, μm/s, on the line dimensions. AFM image (left) and SEM image (right).

Chem 150 **Second Test** April 30, 2014

Interpret the figures and text by expanding on what is being illustrated, explaining procedures or techniques, indicating why it might be important or making connections to our class readings and laboratory work. Tell more than rewriting the caption. Try to use your interpretation to demonstrate additional knowledge beyond what is shown here. ***All material on a given page is from the same paper.***

Nano Lett. (2014) dx.doi.org/10.1021/nl500144k

Figure 2a outlines the procedure for fabricating the AuNP-polymer composite film. Citrate-capped AuNPs with a size of about 15 nm were first synthesized by a slightly modified Turkevich method. A ligand exchange process was then performed to introduce bis(p-sulfonatophenyl)-phenylphosphine (BSPP), a stronger ligand compared to citrate, to the surface of the AuNPs. Adding a trace amount of NaCl changed the solution color from ruby red to blue. Polyvinylpyrrolidone (MW = 360 000) was then dissolved in the solution to form a viscous suspension, which was finally cast onto a glass substrate to produce a composite film after slow removal of the solvent by evaporation.

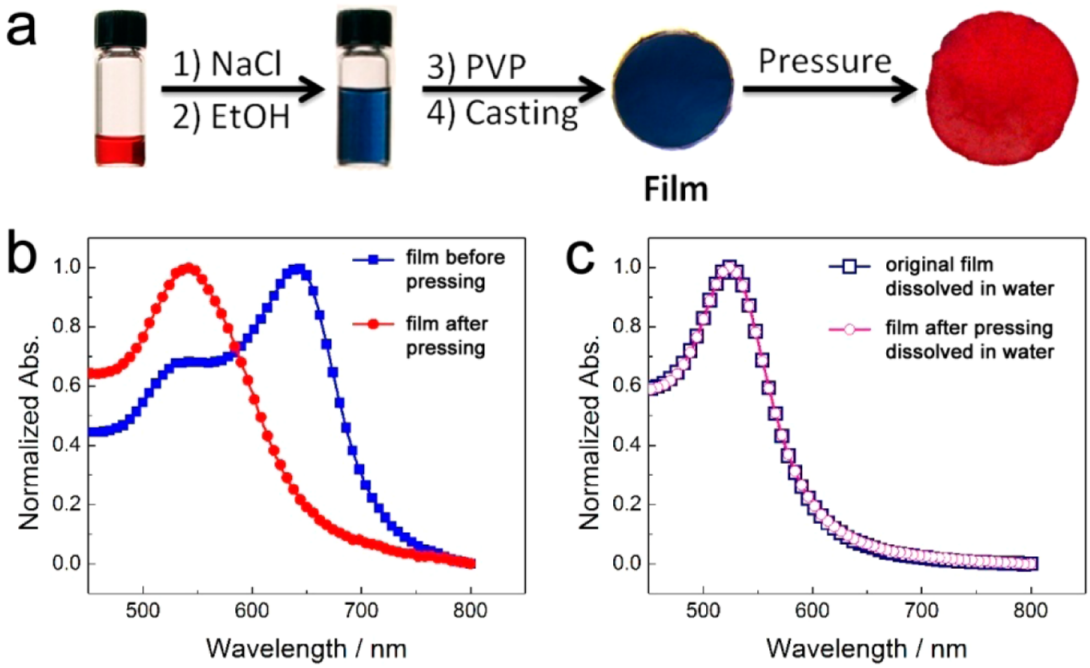

Figure 2. Fabrication of the composite film and its pressure-responsive color switching performance. (a) Illustration of film fabrication procedure and compression test results. (b, c) Normalized UV−vis extinction profiles for films before/after pressing (b) and the nanoparticle suspensions recovered from both films (c).

ZnO hexagonal nanorod arrays on stainless steel foil substrate were achieved by low-temperature deposition in aqueous solution containing 0.035 M $Zn(NO_3)_2$ and 0.55 M $NH_3 \cdot H_2O$ in a sealed beaker at a constant temperature of 75 °C for 30 h. After the growth, the steel foil was covered uniformly by arrays of vertically aligned hexagonal nanorods in tight contact to the stainless steel foil. The X-ray diffraction pattern shows that they are actually crystals of hexagonal ZnO (JCPDS No. 36-1451). After immersing these ZnO nanorod arrays in an aqueous solution consisting of 0.075 M $(NH_4)_2TiF_6$ and 0.2 M H_3BO_3 at room temperature for 40 min, amorphous TiO_2 nanotube arrays could be facilely obtained. The XRD pattern of the TiO_2 nanotube arrays confirmed that they are amorphous. The deposition of TiO_2 from the metal-fluoro complex ion, $TiF_6^{-2} + 6H_2O \leftrightarrow TiO_2 + 6F^- + 4H_3O^+$, is enabled by scavenging the F^- with the help of boric acid, $H_3BO_3 + 4F^- + 4H^+ \leftrightarrow BF_4^- + H_3O^+ + 2H_2O$. This results in the formation of TiO_2 nanotubes, while the ZnO nanorods dissolve in the acidic environment, $ZnO + 2H_3O^+ \rightarrow Zn^{+2} + 3H_2O$.

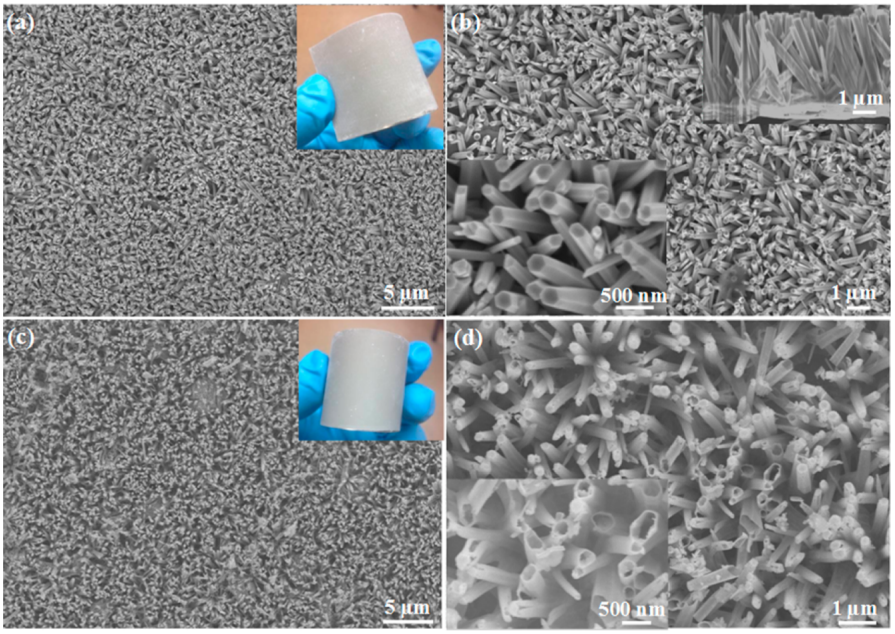

Figure 1. SEM images of ZnO nanorod arrays (a and b) and TiO_2 nanotube arrays (c and d) on stainless steel foil via a facile deposition and in situ etching route.

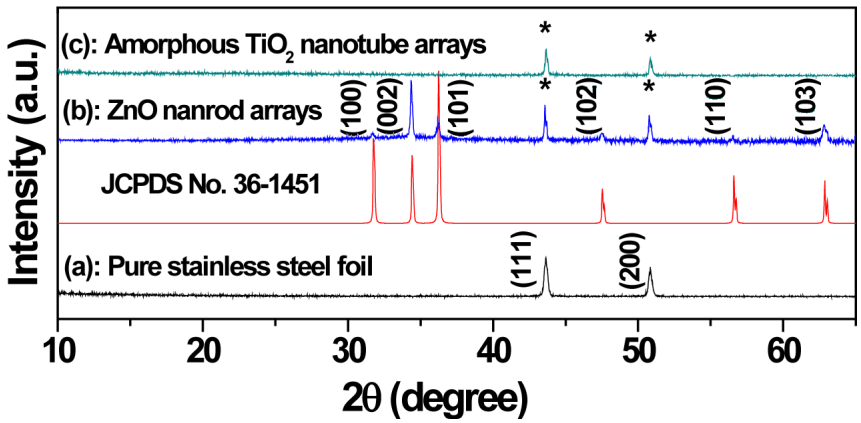

Figure S5. XRD patterns of pure stainless steel foil (a); crystallized ZnO nanorod arrays on stainless steel foil (b); and amorphous TiO_2 nanotube arrays on stainless steel foil (c) The standard XRD patterns of ZnO (JCPDS No. 36-1451) is also presented.

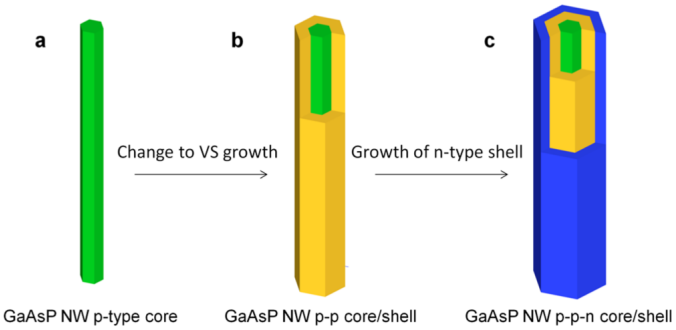

Figure 1. Schematic illustration of the nanowires assembly: (a) the self-catalyzed GaAsP nanowires with Be doping grown by the VLS mechanism, (b) the growth of p-type GaAsP shell by the VS mechanism, and (c) the growth of n-type GaAsP shell by the VS mechanism to form GaAsP p−n homojunction.

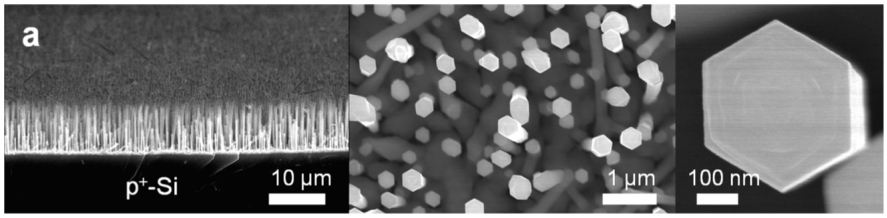

Figure 2. (a) Low-magnification side-view and top-view and high-magnification top-view SEM images of vertically orientated GaAsP p−n homojunction nanowires grown onto a p+-Si (111) substrate.

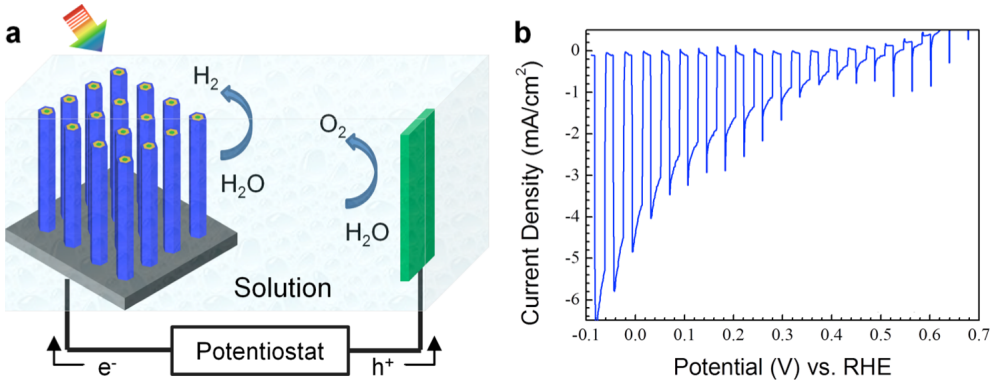

Figure 3. (a) PEC water splitting device structure for GaAsP nanowires grown on Si substrates. (b) Current density potential characteristics of GaAsP homojunction nanowires photocathode. The current-potential curve was measured in 0.1 M KP_i buffer solution (pH 7) at a scan rate of 10 mV/s under chopped AM 1.5G illumination.

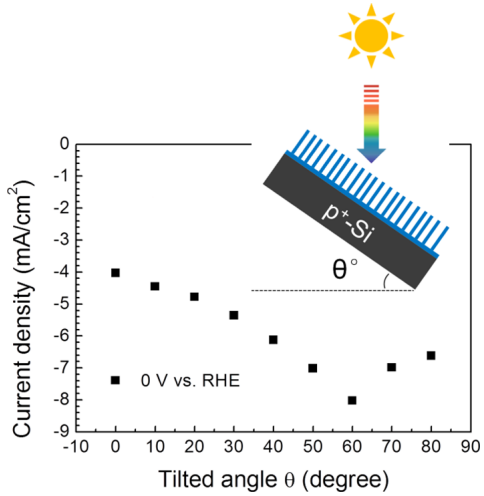

Figure 4. Current density measured 0 V vs RHE as a function of off-normal incident angle θ.

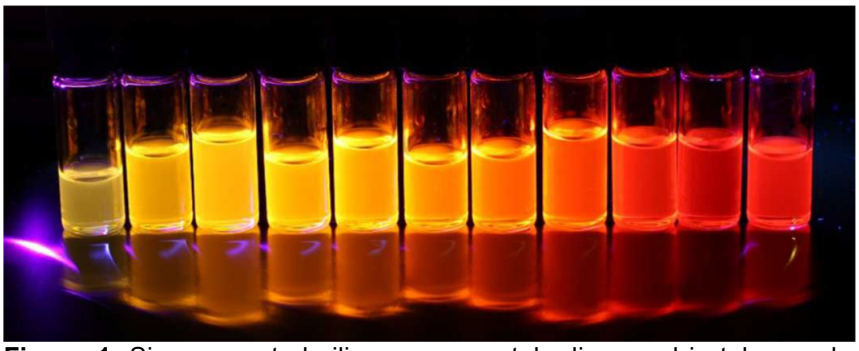

Figure 1. Size-separated silicon nanocrystals dispersed in toluene showing intense luminescence from the deep red to the yellow spectral region. Excitation: (a) 365 nm LED.

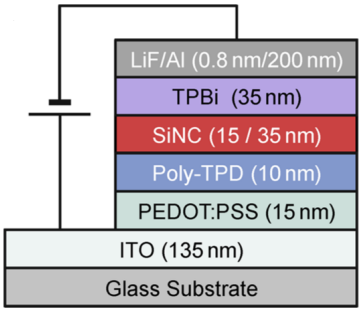

Figure 2. Schematic view of SiLED stack. All SiLEDs were built by spin-coating of the different functional layers on lithographically structured ITO-covered glass substrates followed by a thermal evaporation step of the cathode.

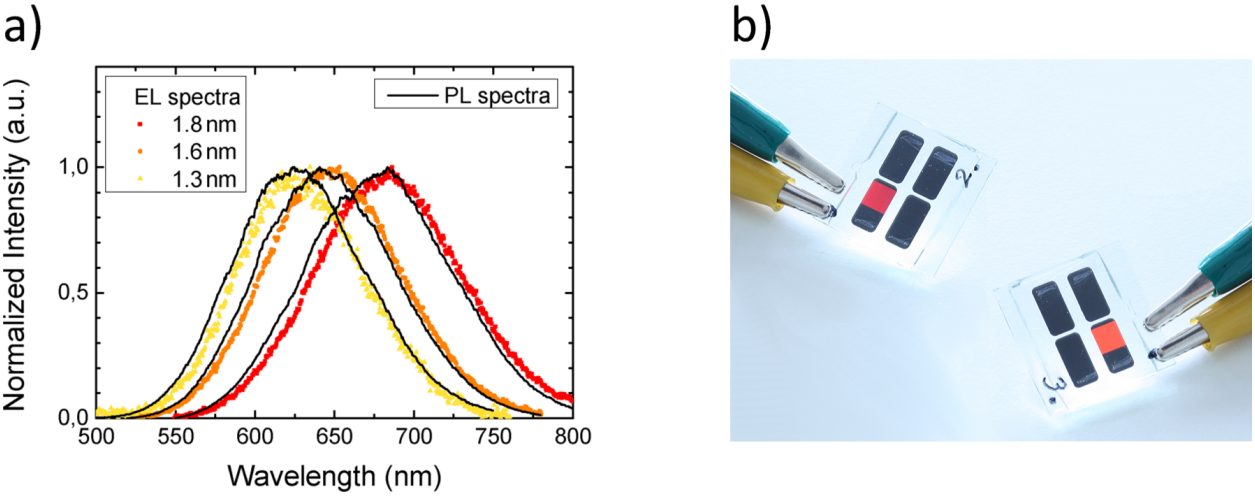

Figure 5. Optoelectronic parameters of SiLEDs featuring different emission wavelengths. (a) Comparison of EL and PL of three different-sized emitters. (b) SiLEDs photographs taken at ambient lighting conditions and unmodified with any image processing software. The SiLEDs feature strong red and orange luminescence and can easily be operated under ambient conditions for several hours.

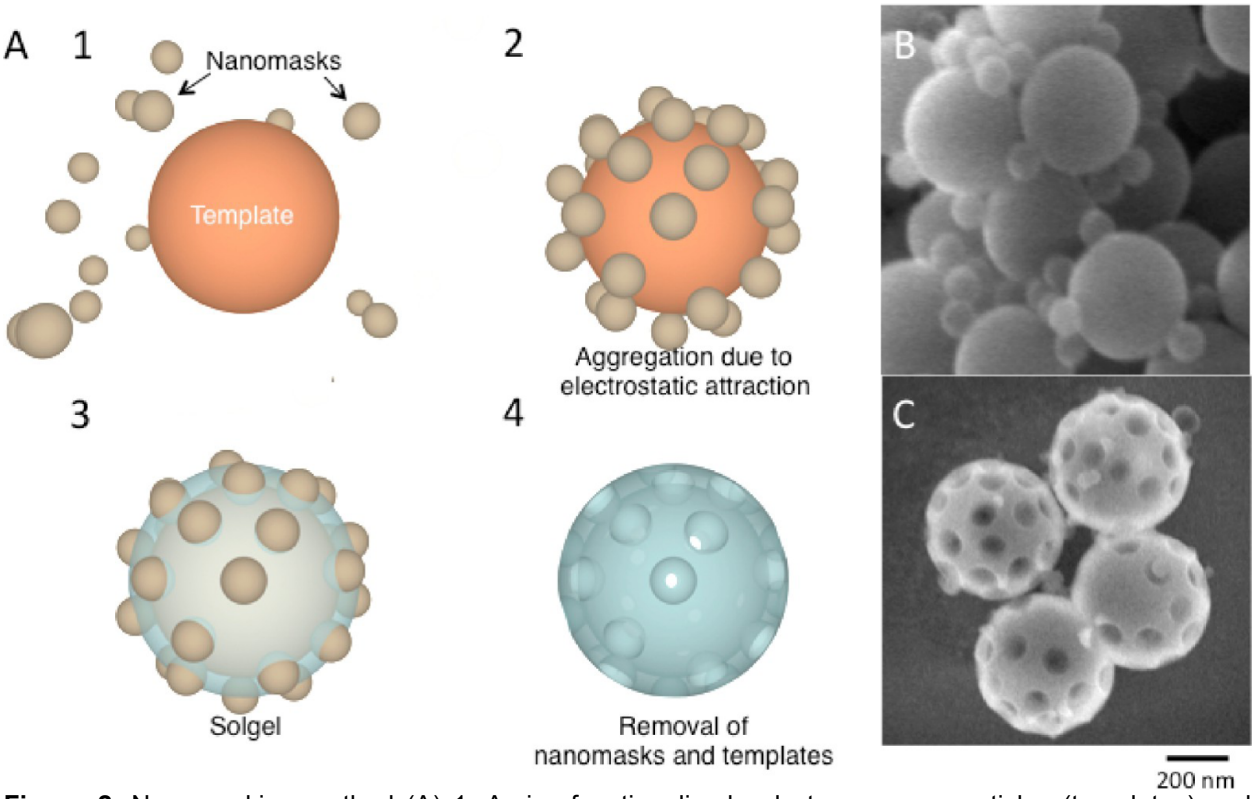

Figure 2. Nanomasking method (A) 1. Amine-functionalized polystyrene nanoparticles (templates) and carboxy-functionalized polystyrene nanoparticles (nanomasks) are mixed in solution. 2. Templates and nanomasks attract each other resulting in aggregation. 3. Tetramethoxysilane (TMOS) is hydrolyzed in aqueous solution to give silicic acid,

$$Si(OCH_3)_4 + 4H_2O \rightarrow Si(OH)_4 + 4HOCH_3.$$

The silica polycondensation reaction occurs on the basic template surface,

$$Si(OH)_4 + OH^- \rightarrow Si(OH)_3O^- + H_2O,$$

$$Si(OH)_4 + Si(OH)_3O^- \rightarrow (HO)_3Si\text{-}O\text{-}Si(OH)_3 + OH^-,$$

while nanomasks block this reaction at the point of contact with the templates. 4. Polymer templates and nanomasks are removed by calcination to generate mesoporous nanospheres. (B) Scanning electron micrograph of aggregated 500 nm templates and 100 nm nanomasks. (C) Scanning electron micrograph of silica mesoporous nanospheres. Scale bar refers to both (B) and (C).

Chem 150 **Second Test** April 24, 2013

Interpret the figures by expanding on what is being illustrated, explaining procedures or techniques, indicating why it might be important or making connections to our class readings and laboratory work. Tell more than rewriting the caption. Try to use your interpretation to demonstrate additional knowledge beyond what is shown here. ***All the figures on a given page are from the same paper.***

Langmuir, **2012**, *28* (36), 13112–13117. **DOI:** 10.1021/la302353t

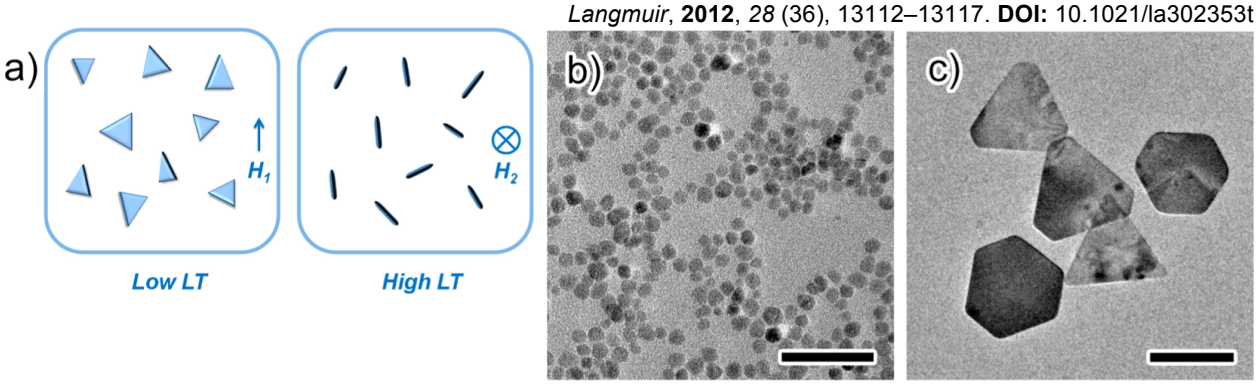

Figure 1. (a) Scheme for tuning of light transmittance of colloidal solution by changing the orientation of (c) Ag nanoplates in ferrofluid composed of (b) Fe_3O_4 nanocrystals. The scale bars in (b) and (c) are 50 and 500 nm, respectively.

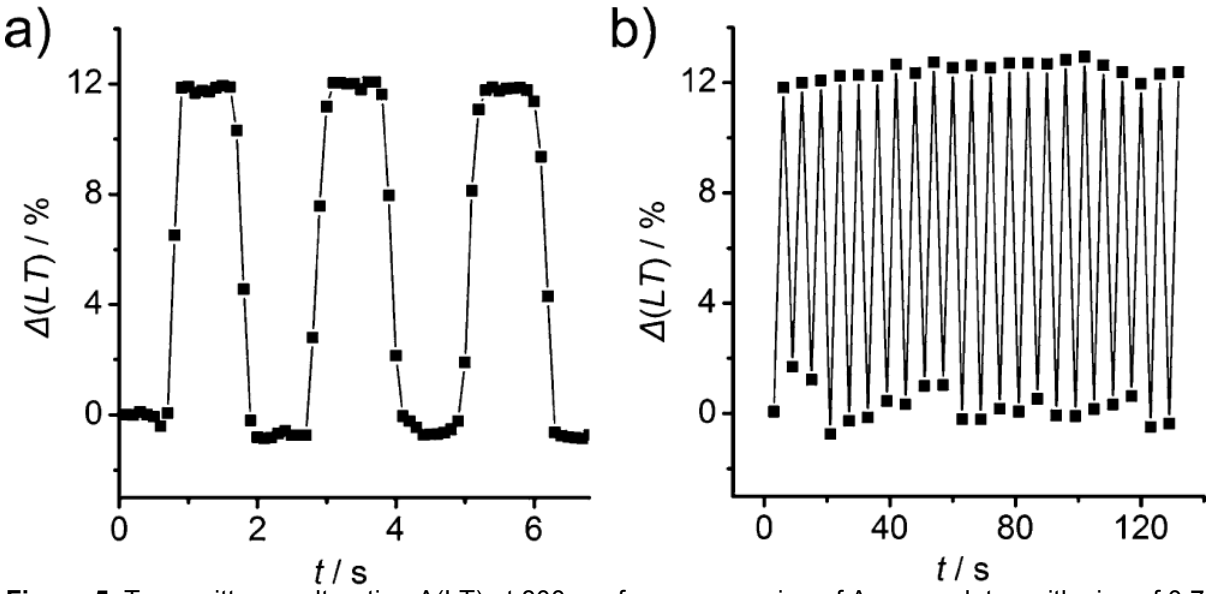

Figure 5. Transmittance alteration Δ(LT) at 800 nm for a suspension of Ag nanoplates with size of 0.7 μm and concentration of 5 mM operated in a periodically orientation-switching magnetic field (280 mT).

Experimental Section. Aqueous ferrofluid containing Ag nanoplates was sealed between two parallel cover glasses, and placed in the light path of UV−vis spectrometer with glass perpendicular to the incident light. A NdFeB magnet or electromagnet was set up around the sample to provide an external magnetic field whose direction was parallel or perpendicular to the incident light. The transmission spectra of the liquid film were measured by an Ocean Optics spectrometer. The transmittance of samples with magnetic field orientation parallel to the light path was set as reference (LT=100%) for the measurement of all samples in this work.

Nano Lett., **2012**, *12* (9), 5014–5019. **DOI:** 10.1021/nl302796f

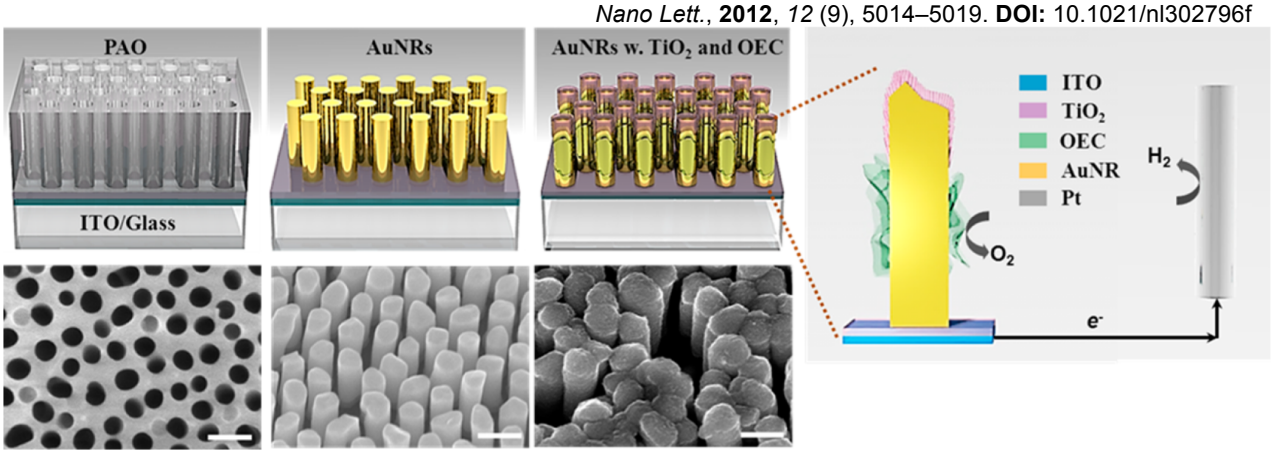

Figure 1. Left: ITO-coated glass slides were coated with a 20nm TiO_2 layer and a 1μm layer of Al prepared by electron-beam evaporation, and the aluminum film was anodized to form porous aluminum oxide (PAO). Middle: Au was electrochemically deposited in the PAO and the PAO template removed by wet etching. Right: TiO_2 was evaporated on the Au nanorods using electron-beam evaporation, and a cobalt borate oxygen evolution catalyst (OEC) electrodeposited on the gold. All scale bars correspond to 150 nm. Extreme right: Schematic of the working cell in which only the plasmonic anode is exposed to light. The cathode is a platinum mesh that is not illuminated.

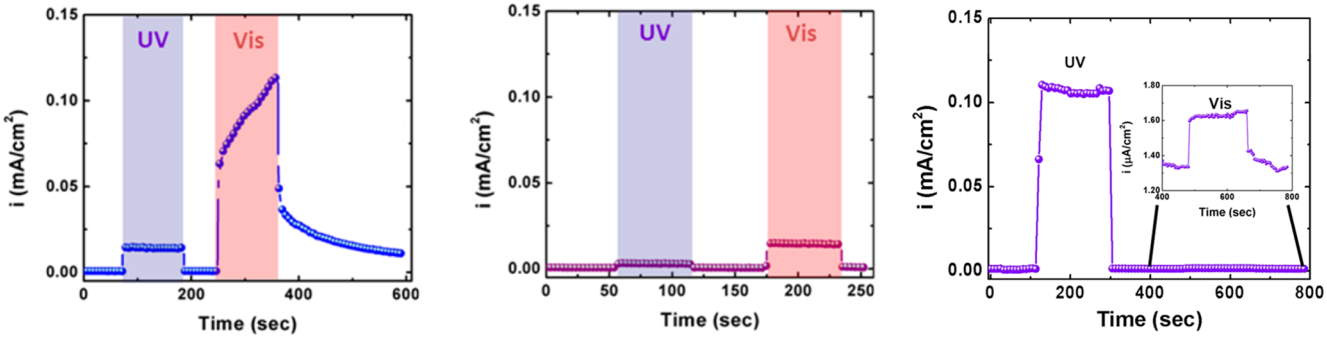

Figures 3 and S2. Left: Photocurrent vs time plots for AuNR/TiO_2 with Co-OEC present on the Au nanorods. Middle: AuNR/TiO_2 in which the Co-OEC was omitted. Right: TiO_2 thin film with Co-OEC deposited on its surface. In the absence of the gold nanorods the visible light activity is ~1% of that measured with UV illumination.

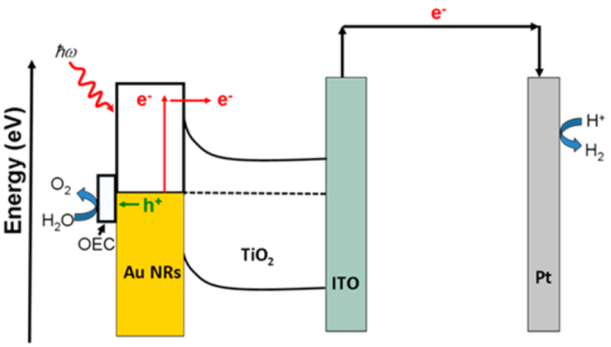

Figure 4. Energy band diagram of the unit. The electron−hole pairs created in AuNR upon excitation in visible light are separated as electron hole pairs with energetic electrons injected into TiO_2. The energetic holes are efficiently extracted by Co-OEC and used for water oxidation.

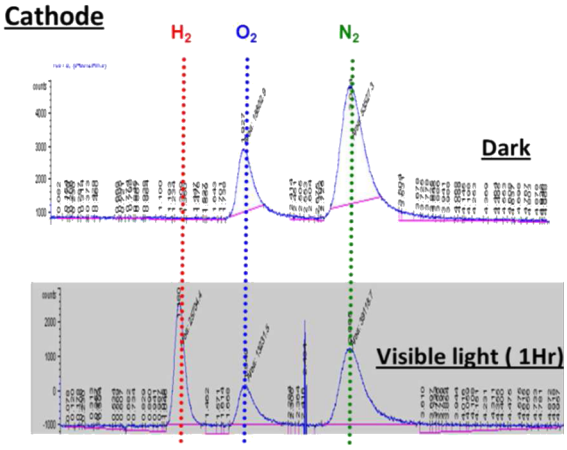

Figure S3. Gas chromatography analyses of gases observed in the Pt mesh cathode compartment. A clear H_2 peak is observed in the cathode compartment after 1 hour of visible light illumination. No measurable H_2 peaks were observed during dark periods.

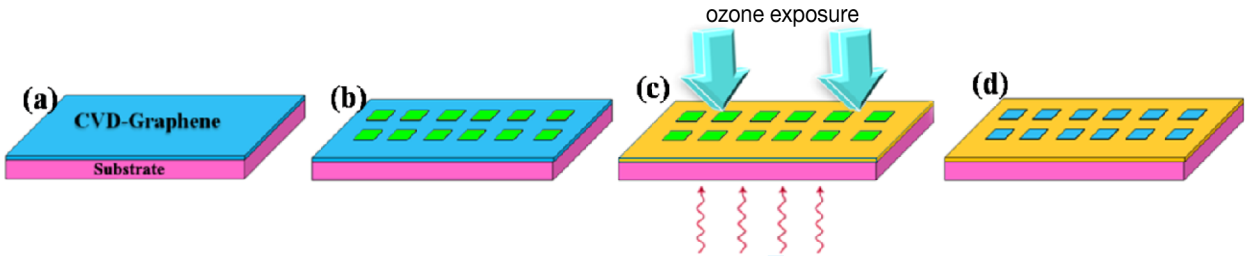

Figure S2. The patterning process of graphene films by ozone photolithography. (a) Pristine graphene film (blue) is transferred to a target substrate; (b) Photoresist coating (green) is added at specific locations using standard photolithography; (c) Graphene with photoresist patterns is treated by ozone at temperatures higher than 80°C to cause the exposed regions to become insulating; (d) The photoresist coating is removed to give conductive grapheme squares separated by insulating GO strips.

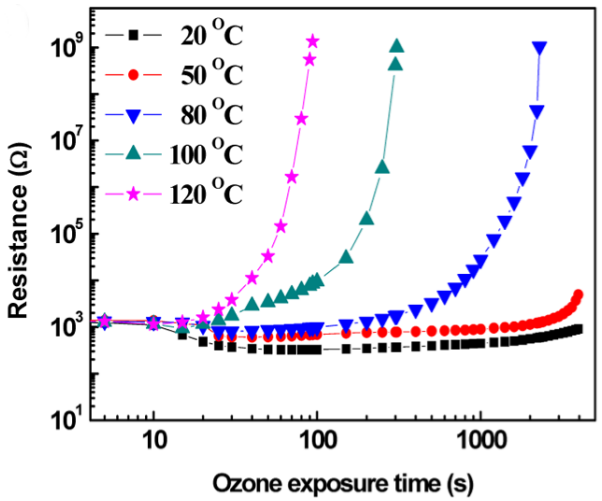

Figure 1. Electrical resistance change of CVD-grown graphene films over time at different ozone treatment temperatures.

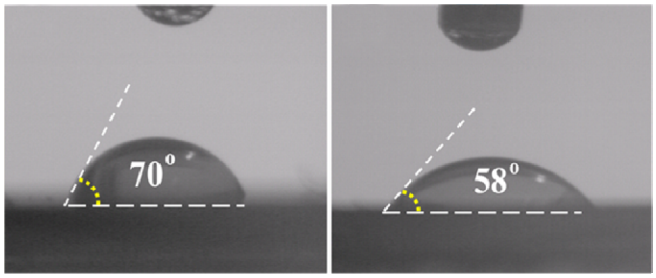

Figure S3. Contact angle of the graphene surface before (left) and after (right) ozone photolithography.

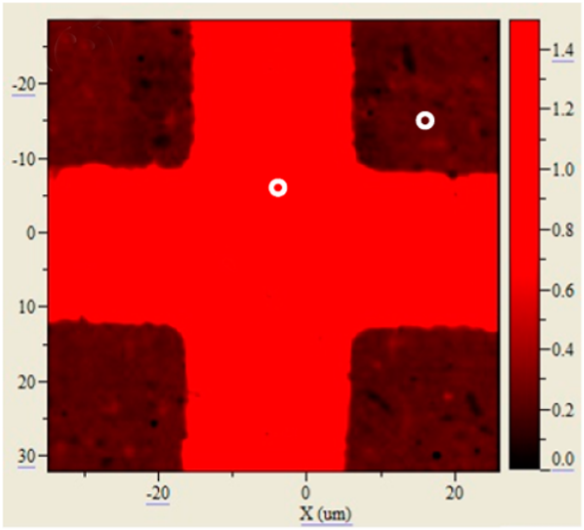

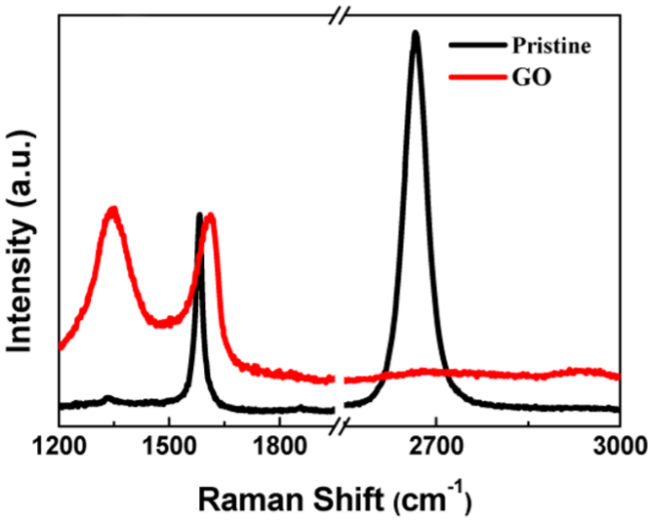

Figure 6. Raman mapping results. Left: The red cross represents the GO strips, and the black squares are the pristine graphene. Right: Raman spectra corresponding to the different regions in the pattern (white circles).

Nano Lett., **2013**, *13* (3), pp 994–999. **DOI:** 10.1021/nl3041417. Publication Date (Web): February 13, 2013

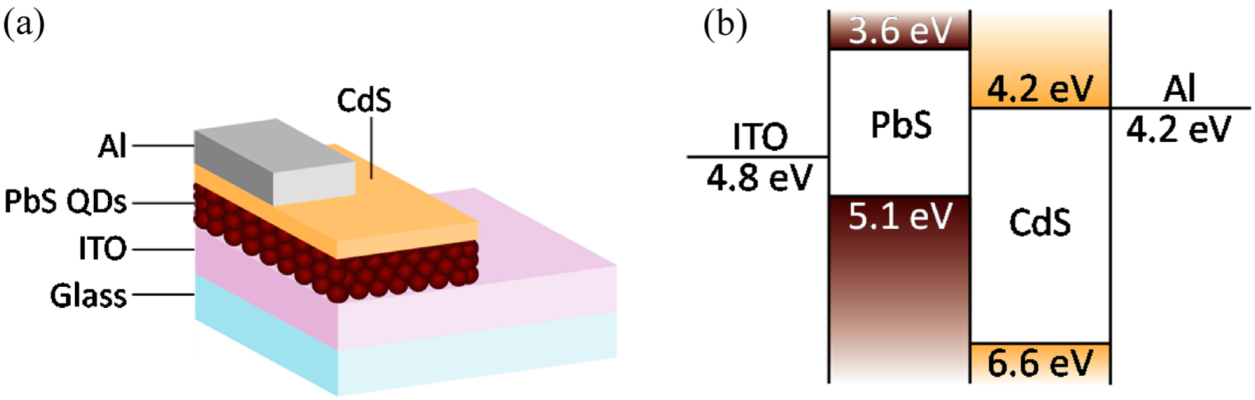

Figure 1. (a) Schematic of the PbS QD/CdS heterojunction device fabricated in this study. (b) Energy band diagram showing band edges of isolated 1.5eV PbS QDs and CdS along with electrode work functions.

Device Fabrication: Patterned ITO glass substrates (purchased from Thin Film Devices) were treated with 15mM (3-mercaptopropyl)trimethoxysilane (MPTMS) in toluene overnight to promote adhesion between PbS QDs and substrates. After treatment, the substrates were sonicated and rinsed with 2-propanol to remove free MPTMS molecules. PbS QDs were deposited onto treated ITO glass substrates via dip coating in a glovebox. A dip coating cycle consists of: (1) dipping the substrate into 10mg/ml PbS QDs in hexane, (2) dipping the film in 2mM 1,2-ethanedithiol in acetonitrile for 30 sec, and (3) rinsing by dipping in pure acetonitrile. The above dip coating cycle was repeated to achieve desired PbS QD thicknesses. The PbS QD-coated ITO substrates were then immersed into a 100mL aqueous solution, containing 138 mg of cadmium acetate, 308 mg of ammonium acetate, 4.1 mL of ammonium hydroxide, and 91 mg of thiourea, at 80 °C for 10 min to deposit the CdS layer. Finally, Al electrodes were deposited via thermal evaporation at a rate of 0.1 nm/s at a base pressure of 2×10^{-6} Torr.

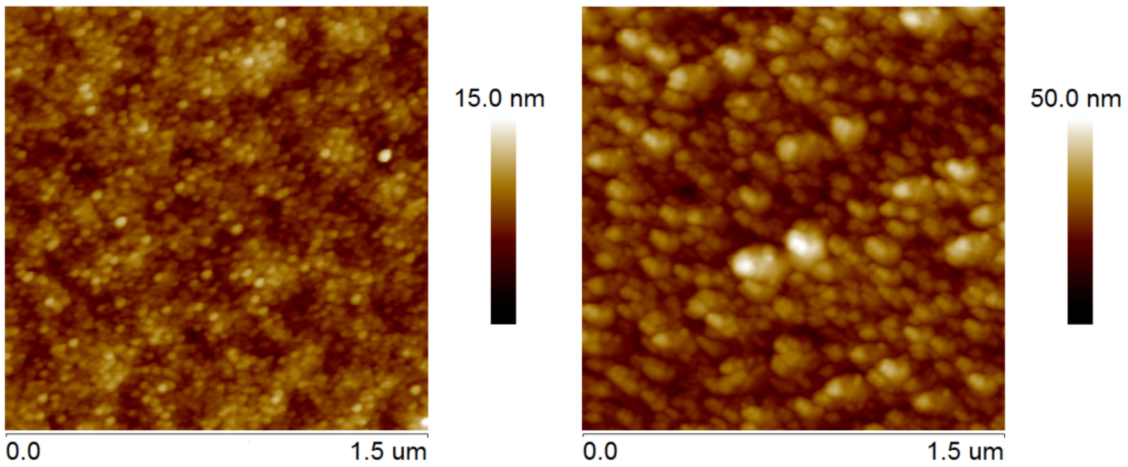

Figure S6. AFM surface images of (left) the PbS QD thin film and (right) the CdS thin film.

Chem 150 **Second Test** April 25, 2012

Interpret the figures by expanding on what is being illustrated, explaining procedures or techniques, indicating why it might be important or making connections to our class readings and laboratory work. Tell more than rewriting the caption. Try to use your interpretation to demonstrate additional knowledge beyond what is shown here. ***All the figures on a given page are from the same paper.***

Nano Lett., **DOI:** 10.1021/nl2042968, Publication Date (Web): February 24, 2012

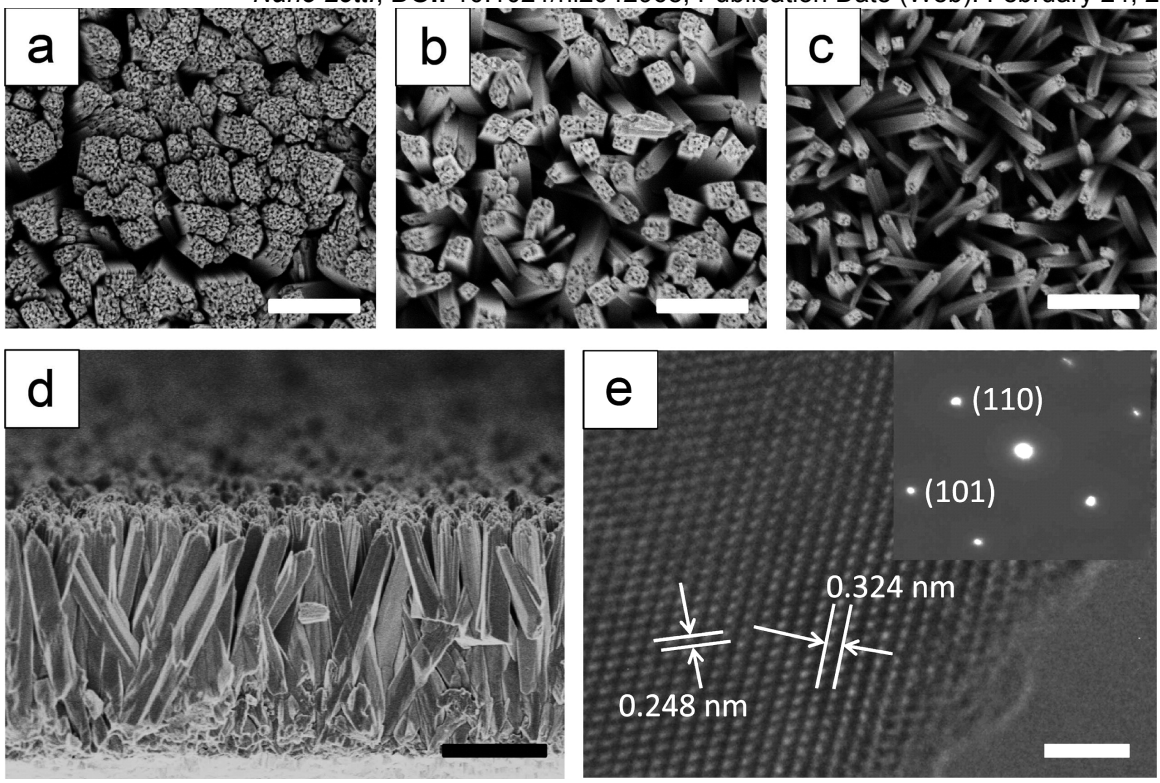

Figure 1. (a−c) Top-view SEM images of as synthesized Sn/TiO_2 NW arrays with different densities on FTO-coated glass substrates. Scale bars in panels a−c are 500 nm. (d) Side-view SEM image of as-synthesized Sn/TiO_2 NW array with median density, as in b. Scale bar is 1 μm. (e) HR-TEM images of a typical Sn/TiO_2 NW. Two d-spacing values of 0.324 and 0.248 nm are shown, correlated to (110) and (101) planes of a rutile TiO_2 structure, respectively. Scale bar is 2 nm.

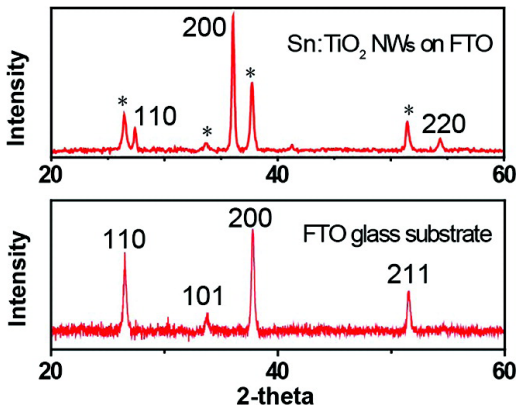

Figure 2. Upper: XRD spectrum of as-synthesized Sn/TiO_2 NW arrays on a FTO-coated glass substrate. The (110), (200), and (220) peaks of TiO_2 are marked. Lower: XRD spectrum of a blank FTO-coated glass substrate.

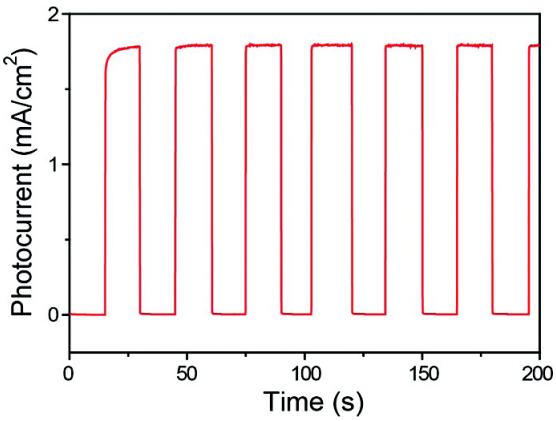

Figure 4. Time-dependent photocurrent density of a Sn/TiO_2 NW photoanode at repeated on/off cycles of simulated sunlight illumination at −0.44 V versus Ag/AgCl with 1 M KOH used for the electrolyte solution.

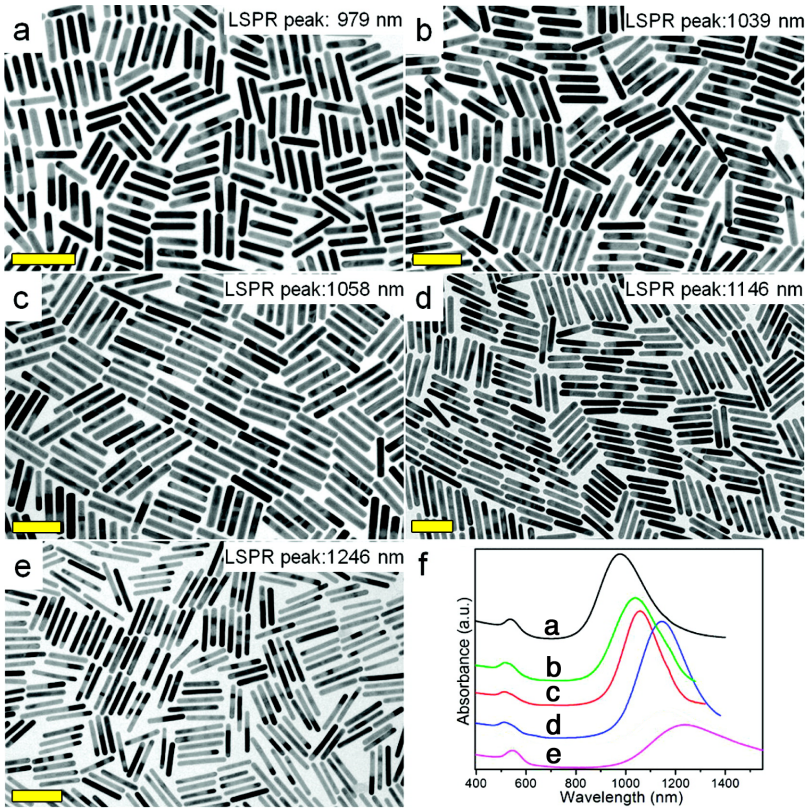

Figure 4. Synthesis of high aspect ratio gold NRs using hexadecyltrimethylammonium bromide (CTAB) surfactant with the addition of HCl to lower the pH and 5-bromosalicylic acid as an additive. The NR aspect ratio can be further tuned by the amount of $AgNO_3$ added. (a-e) TEM image of gold NRs synthesized as indicated in Table S4 and labelled with the longitudinal surface plasmon resonance (LSPR) peak. All scale bars represent 100 nm. (f) Respective UV-vis-NIR spectra of gold NRs.

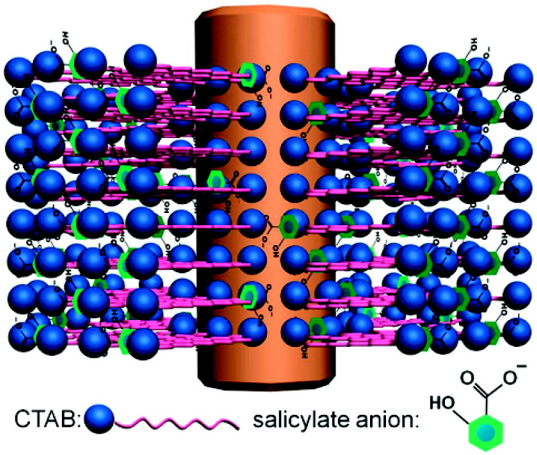

Figure 8. A cartoon illustrating the proposed mechanism to explain the role of aromatic additives (sodium salicylate is shown as an example) in mediating the binding between CTAB bilayers and certain facets of growing gold NRs. Note that surfactant molecules are not drawn at the nanorod tip region for clarity purposes.

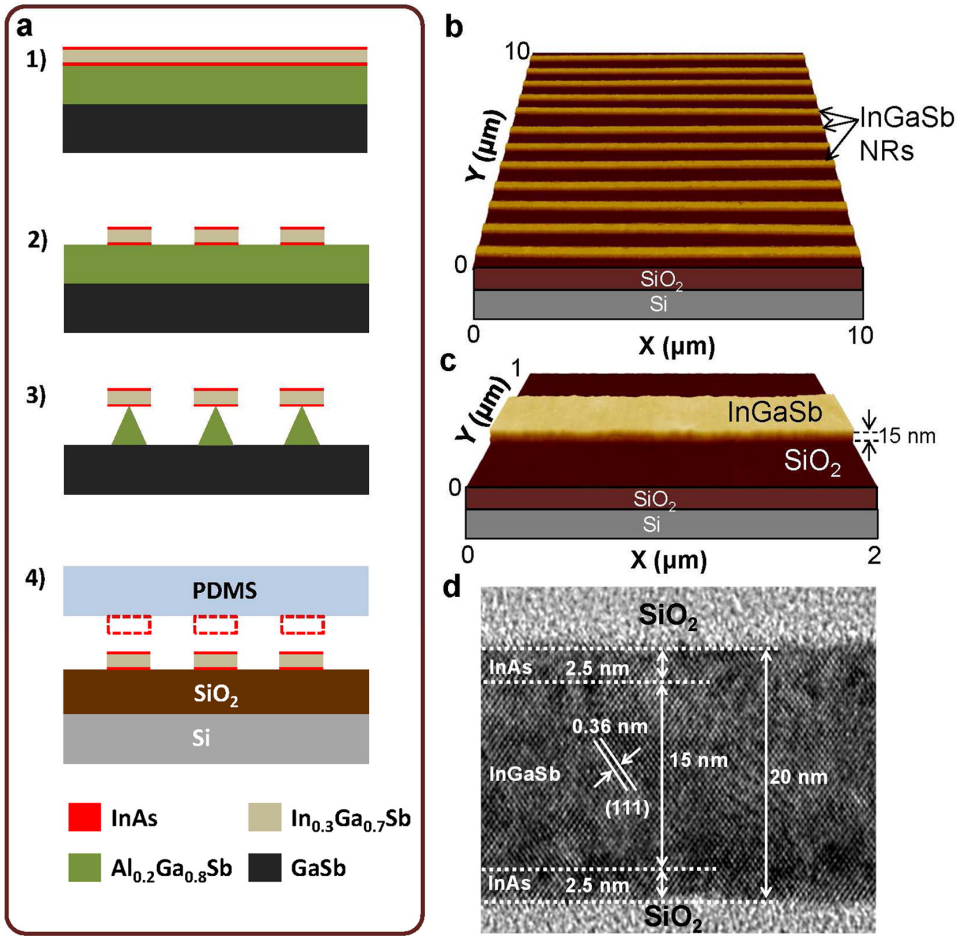

Figure 1. Figure 1. InAs/InGaSb/InAs heterostructure III−V on-insulator device architecture (XOI). (a) Process schematic illustrating the fabrication of ultrathin InAs/InGaSb/InAs XOI substrates. The initial structure (1) is first prepatterned into NRs by lithography and wet etching (2). Afterward, the AlGaSb sacrificial layer is etched to partially release the NRs (3) which are subsequently transferred onto a Si/SiO_2 substrate by employing a PDMS slab (4). (b,c) AFM images of transferred InAs/InGaSb/InAs NRs on a Si/SiO_2 substrate with a width and height of ~350 and ~15 nm (T_{InGaSb} = 10 nm), respectively. (d) TEM image of an InAs/InGaSb/InAs XOI (T_{InGaSb} = 15 nm).

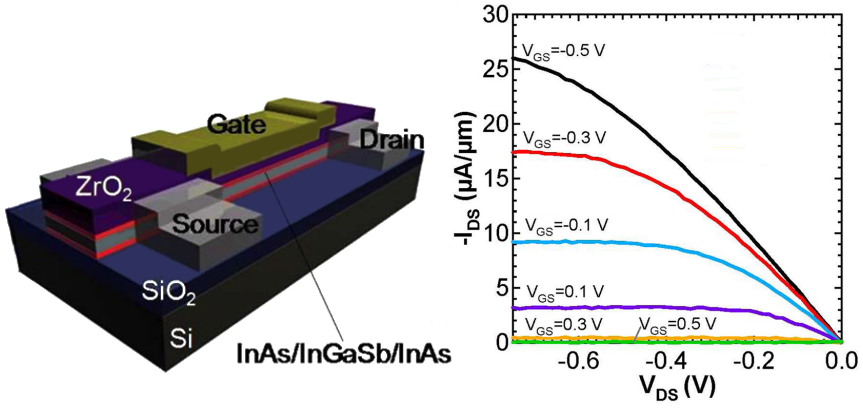

Figure 5. Output characteristics of a top-gated (10 nm ZrO_2 gate dielectric) InAs/InGaSb/InAs XOI p-FET with a channel length of ~6.1 μm and T_{InGaSb} = 7 nm. The Si substrate is grounded during the measurements.

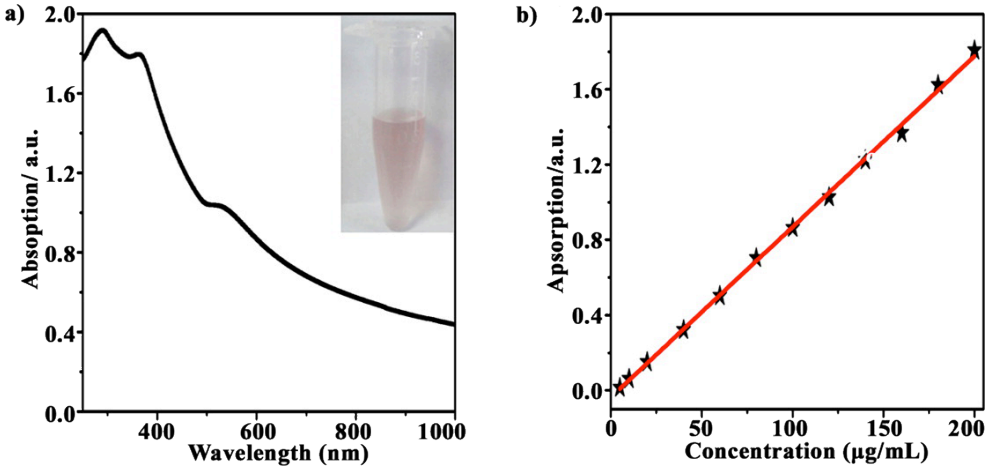

Figure 2. (a) UV−vis-NIR spectrum of AuNPs@SiNWs aqueous solution with a concentration of 70 μg/mL. Inset shows a corresponding photo of the AuNPs@SiNWs sample. (b) Absorbance at 808 nm vs AuNPs@SiNWs concentration.

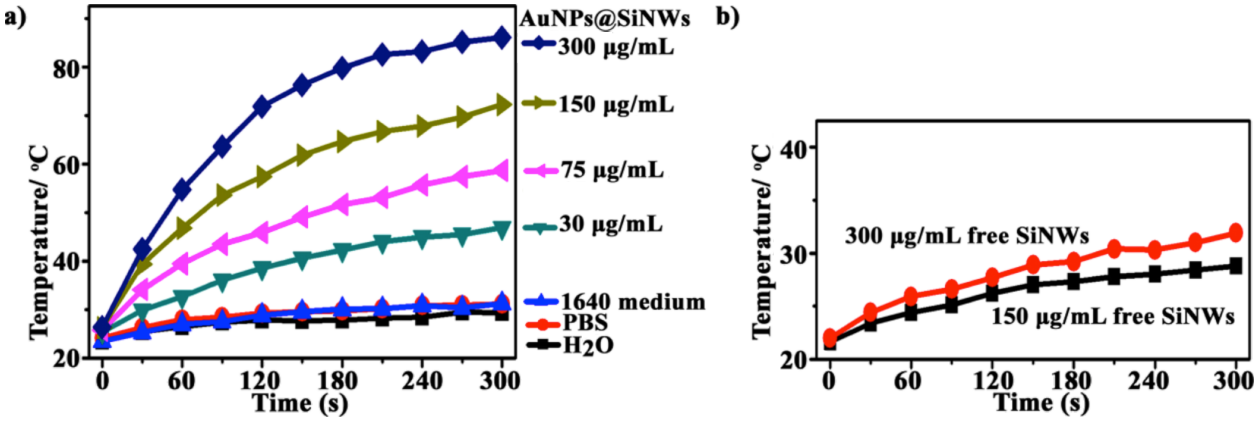

Figure 3. Photothermal effect of AuNPs@SiNWs (a) and free SiNWs (b) solutions showing temperature increase as a function of NIR irradiation (2W/cm^2) time and sample concentration. AuNPs@SiNWs solutions showed a rapid rise in temperature, whereas water, PBS, and RPMI 1640 medium showed little change in temperature upon NIR laser irradiation.

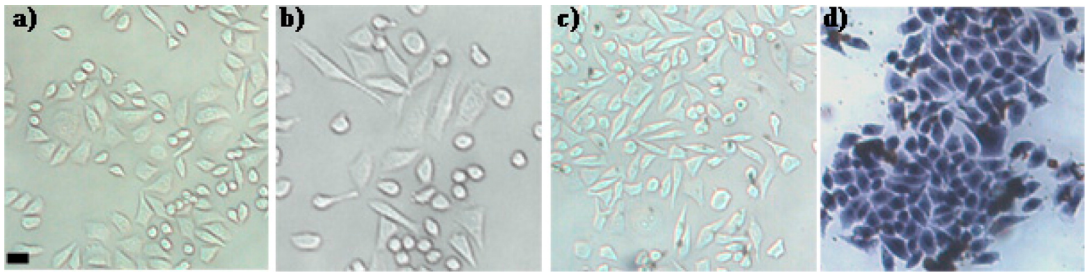

Figure 5. Optical images of KB cells. (a) Control cells, (b) control cells after laser irradiation, (c) cells cultured with 150 μg/mL PEG-AuNPs@SiNWs, and (d) cells cultured with 150 μg/mL PEG-AuNPs@SiNWs after 3 min 2 W/cm^2 808 nm laser irradiation. Dark color indicates dead cells (Trypan blue test). Scale bar = 20 μm.

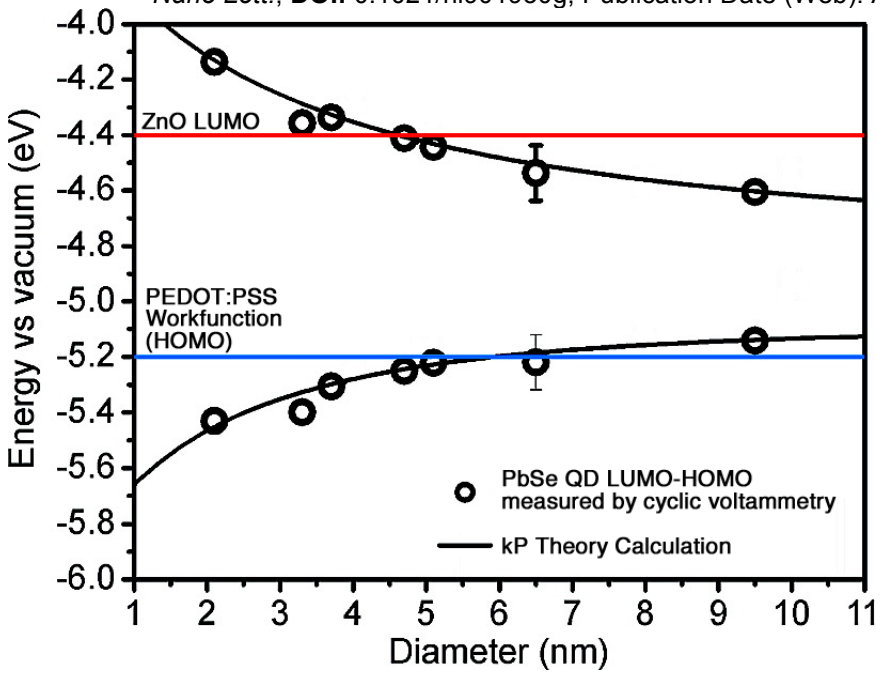

Figure 1. Size dependent PbSe NC energy levels measured by cyclic voltammetry (circles). Measured energy levels show good fit with theoretical calculation (curves). The upper horizontal line shows the ZnO LUMO level and the lower horizontal line shows the PEDOT:PSS workfunction (HOMO).

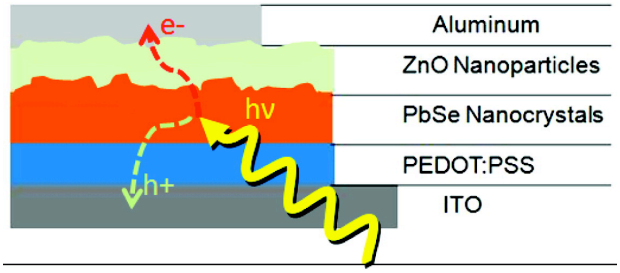

Figure 2. PbSe NC photovoltaic device structure that employs ZnO and PEDOT:PSS as electron and hole collection layers respectively.

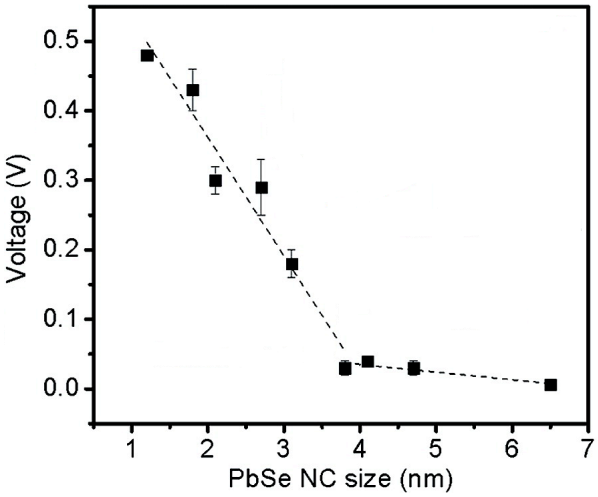

Figure 3. Voltages from devices (V_{OC}) with various PbSe NC sizes. Two distinctive domains are observed. Devices made from large (d > ~3.8 nm) NCs show no appreciable photovoltaic effect whereas devices made from small (d < ~3.8 nm) NCs show increasing V_{OC} with decreasing NC size. The critical diameter (~4 nm) agrees reasonably with the CV result.

Chem 150 **Second Test** April 27, 2011

Interpret the figures by expanding on what is being illustrated, explaining procedures or techniques, indicating why it might be important or making connections to our class readings and laboratory work. Tell more than rewriting the caption. Try to use your interpretation to demonstrate additional knowledge beyond what is shown here.
All the figures on a given page are from the same paper.

Nano Lett., **2011**; 10.1021/nl2001692

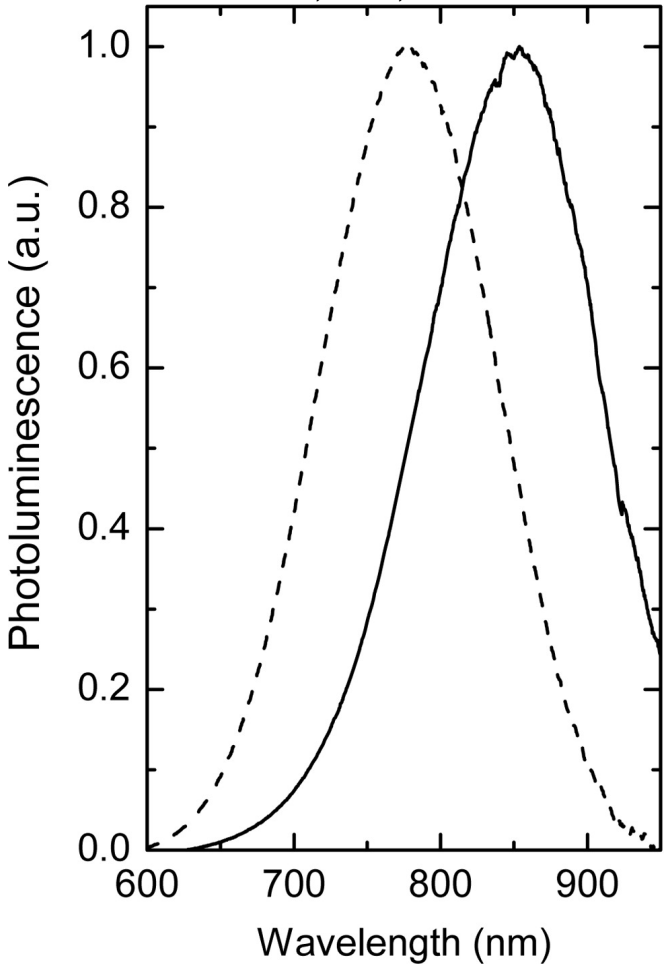

Figure 1. Photoluminescence for silicon nanocrystals chemically passivated with 1-dodecene. The diameters of the silicon nanocrystals shown are 5 nm (solid line) and 3 nm (broken line) with peak emission wavelengths of 853 and 777 nm, respectively. For both spectra, the excitation wavelength is 395 nm.

Nano Lett., **2011**, *11* (3), pp 1331-1336; 10.1021/nl104412b

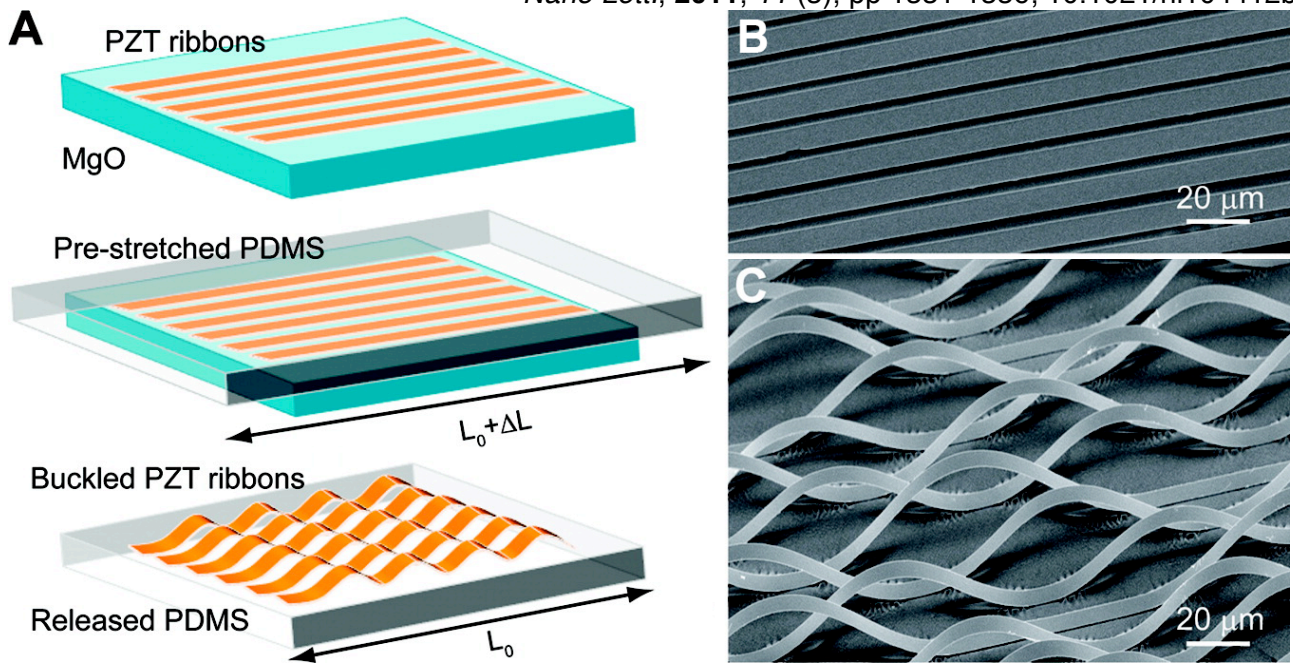

Figure 1. From top to bottom: (a) $Pb[Zr_{0.52}Ti_{0.48}]O_3$ ribbons were patterned on an MgO substrate and undercut etched using phosphoric acid (85% concentration, 75 °C, ~50 s); a slab of prestrained PDMS (~2mm thick) was laminated against the ribbons and peeled off quickly; retrieved PZT ribbons formed wavy/buckled structures upon strain relaxation. (b) SEM image of PZT ribbons transfer printed to PDMS with zero prestrain. (c) PZT ribbons spontaneously buckled under prestrained conditions.

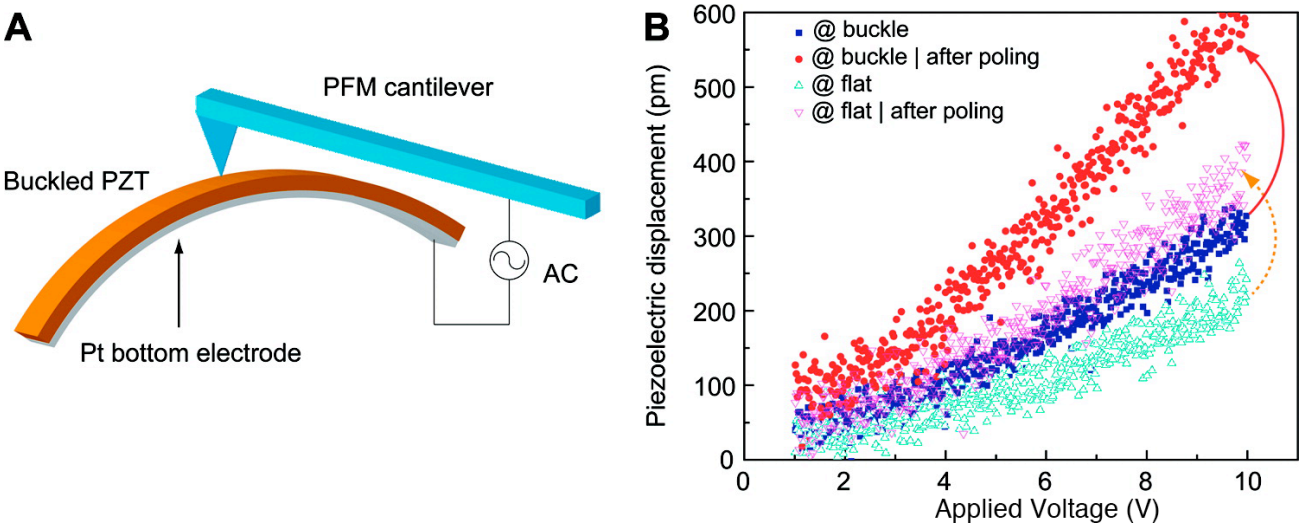

Figure 2. An ac modulating voltage was applied between the tip and Pt underlayer, and the piezoelectric displacement was measured at the tip. (a) Schematic illustration of the measurement performed on a ribbon buckle. (b) Representative piezoelectric displacement in buckled and flat regions of wavy PZT ribbons, as functions of the applied ac tip bias, before and after poling at 100 kV/cm for 30 min.

"Domains are usually randomly oriented, but can be aligned using the process of *poling*, a process by which a strong electric field is applied across the material, usually at elevated temperatures."

http://en.wikipedia.org/wiki/Poling_(piezoelectricity)

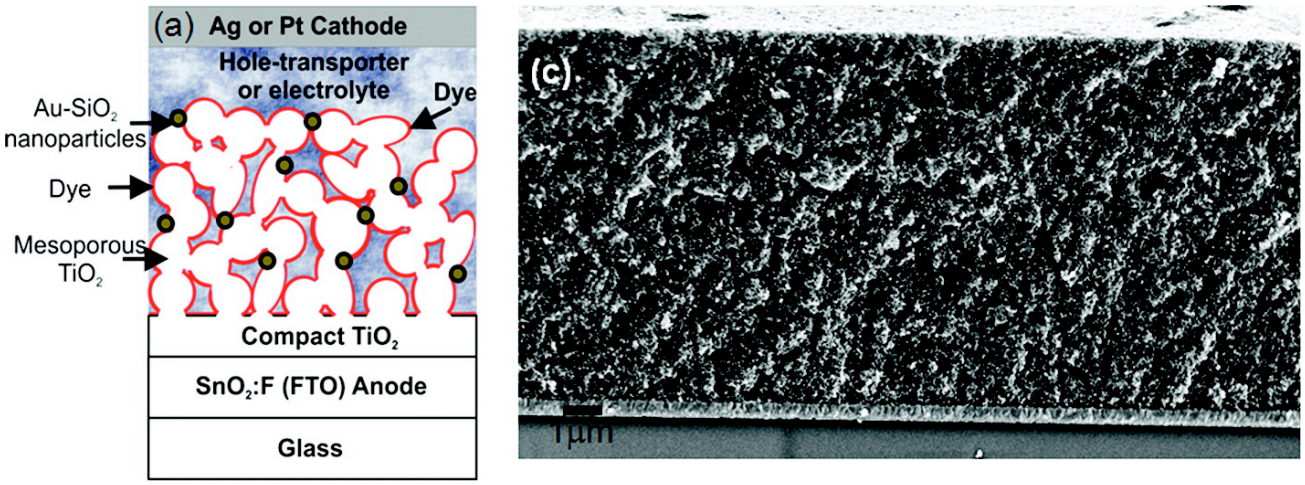

Figure 2. (a) Schematic illustration of the structure of dye-sensitized solar cells incorporating the core-shell Au-SiO_2 nanoparticles. Drawings are not to scale; the TiO_2 nanoparticles are around 20 nm in diameter, the Au-SiO_2 nanoparticles are around 15 nm in diameter, and the overall film thickness is between 1 to 5 μm. (c) SEM cross-sectional image of the mesoporous TiO_2 film incorporating the Au-SiO_2 nanoparticles.

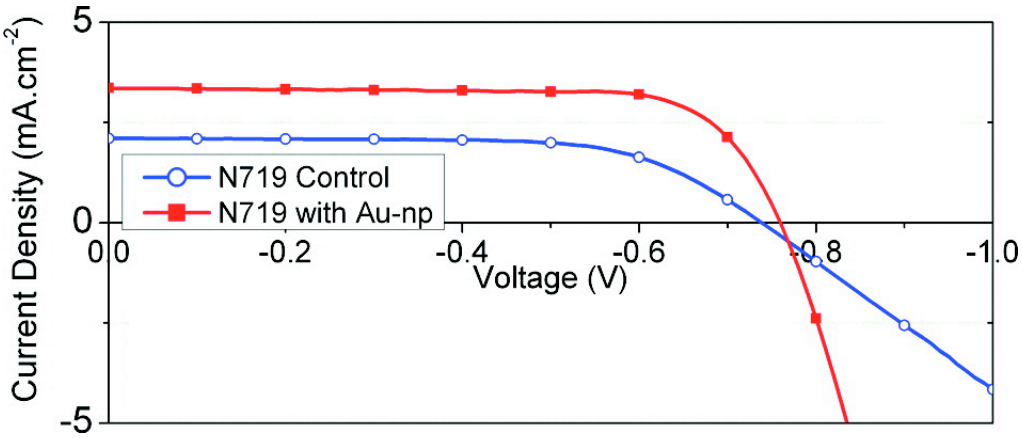

Figure 3. Current-voltage characteristic for N719 ruthenium sensitizer and iodide/triiodide liquid electrolyte-based DSSCs of 1.1 μm thickness with dye only (blue, open circles) and with the incorporation of the Au-SiO_2 core (15 nm)-shell (3 nm) nanoparticles into the paste. Dye only devices showed an average efficiency of 1.08 ± 0.10%, while those incorporating Au-SiO_2 nanoparticles produced an average efficiency of 1.65 ± 0.32%. The photocurrent is significantly enhanced with the presence of the Au-SiO_2 nanoparticles, indicating that the light harvested from these “plasmonic” components is directly contributing to the photocurrent generation within the devices.

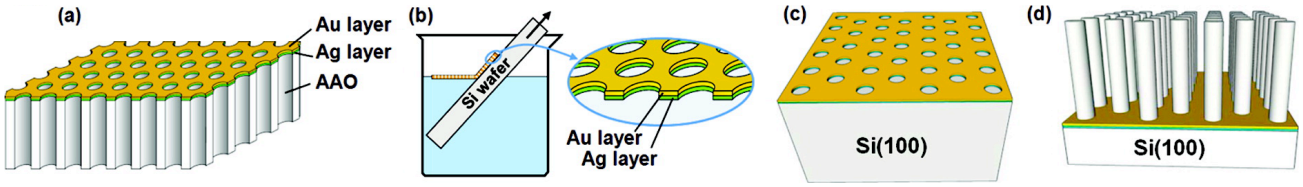

Figure 1. Schematic of the SiNW fabrication process: (a) sequential sputter depositions of Ag and Au on the surface of AAO membrane; (b) transfer of Au/Ag bilayered metal mesh onto a silicon wafer from the surface of etching solution after removal of AAO membrane from the bottom side of the metal mesh; (c) metal-assisted chemical etching using mixtures of HF, H_2O_2, and H_2O; (d) fabrication of SiNWs with controlled axial orientations and morphologies.

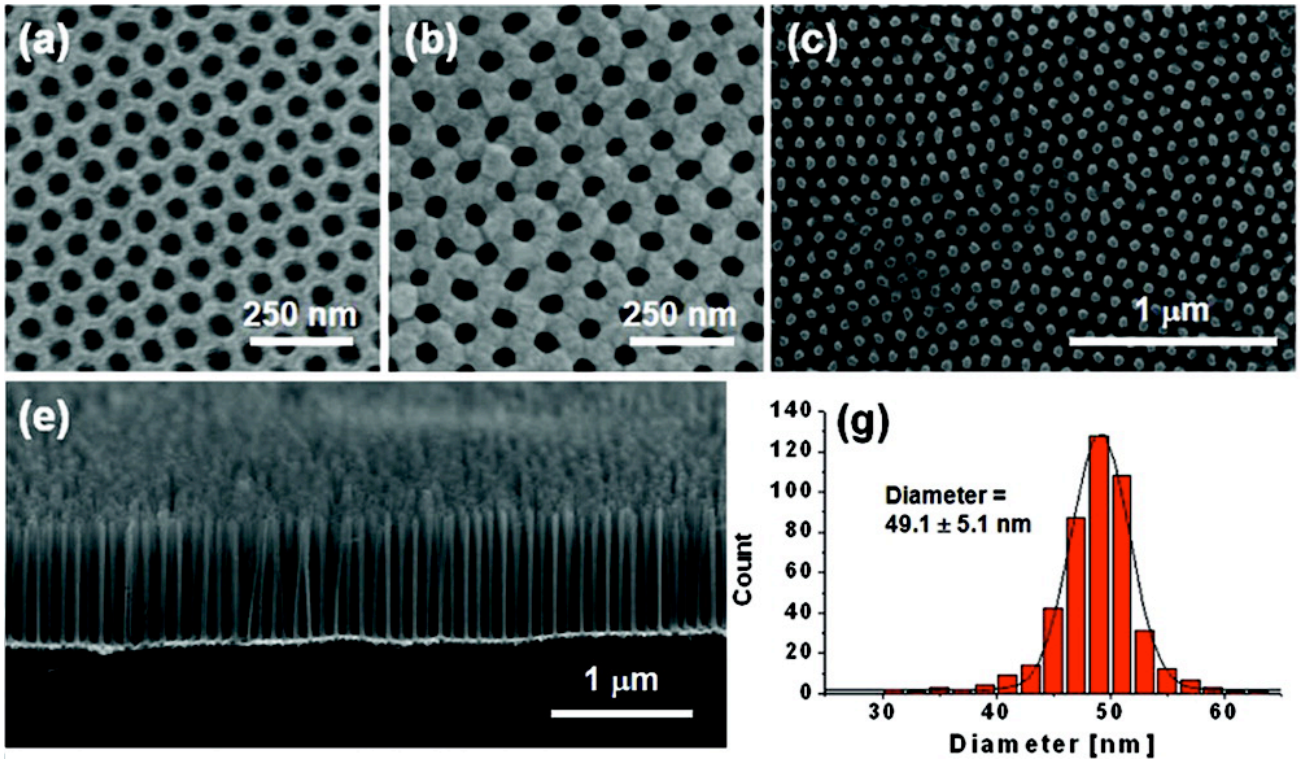

Figure 2. SEM micrographs of (a) AAO membrane and (b) Au/Ag bilayered metal mesh. (c) Typical plan-view SEM image of vertically aligned SiNWs obtained by metal-assisted chemical etching of Si(100) wafers by using Au/Ag bilayered metal mesh. (e) Cross-sectional SEM images of vertically etched Si(100) wafers, showing SiNWs with 39.5 ± 4.2 nm diameters; (g) Histogram showing the diameter distribution of SiNWs shown in panel c, together with a Gaussian fit (solid line) of the measured statistical data.

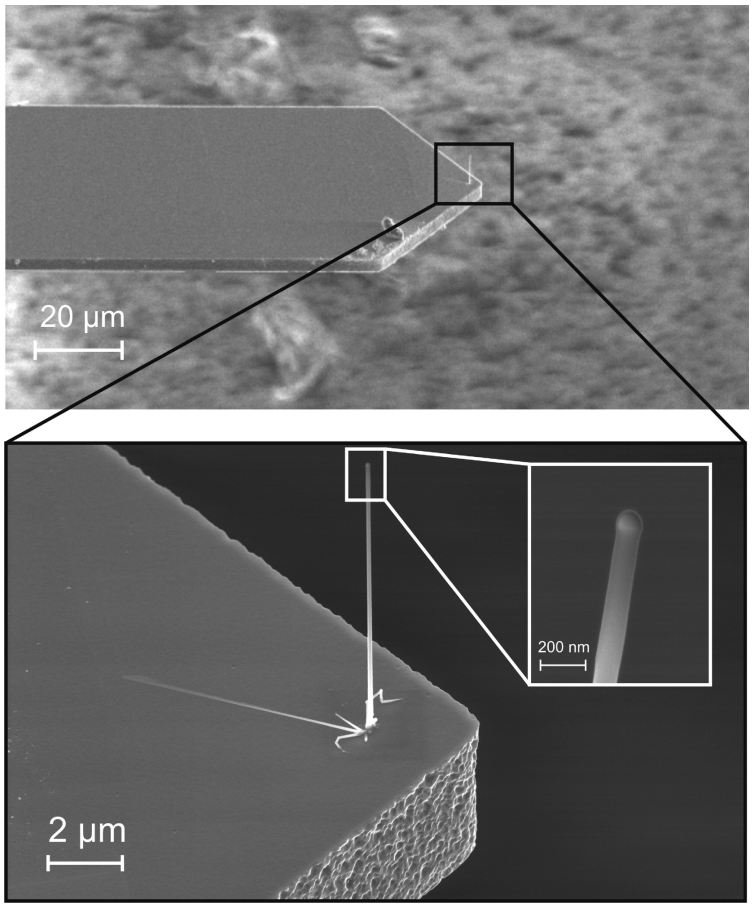

Figure 4. Electron micrograph of an epitaxially grown SiNW on an AFM cantilever.

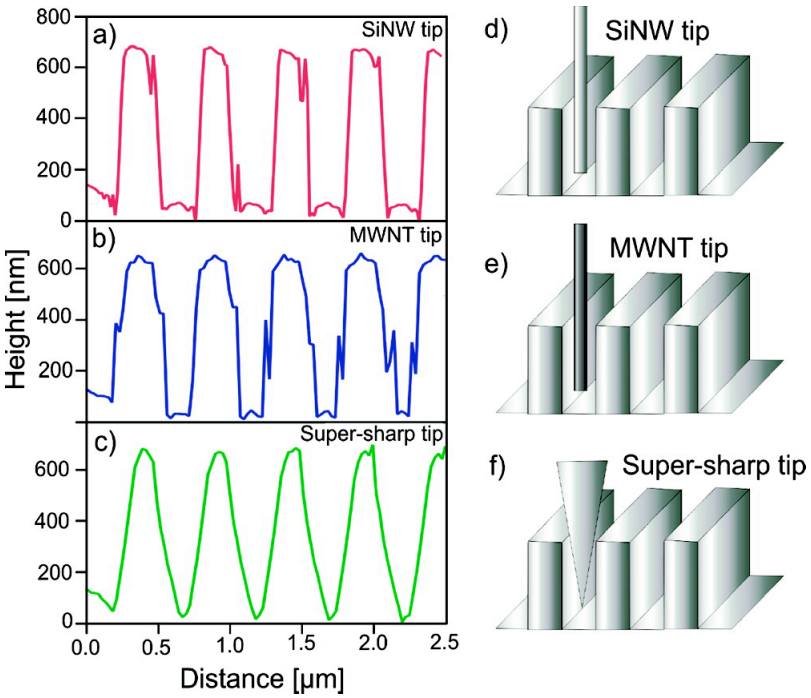

Figure 6. (a-c) AFM scans of a silicon trench using a SiNW, MWNT, and Supersharp AFM tip. (d-f) Illustration of a SiNW, MWNT, and Supersharp AFM tip scanning a silicon trench.

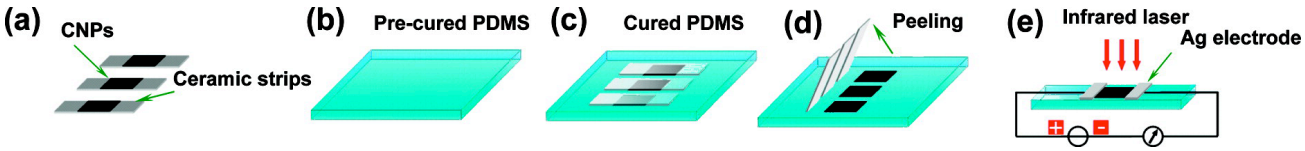

Figure 1. Schematic diagram of the fabrication of infrared sensors. (a) CNPs were first grown on ceramic strips by a simple flame synthesis process in an alcohol burner. (b) The PDMS base and curing agent were mixed with a ratio of 10:1. After intense stirring, the solution was heated in a 60 °C electrical oven for about 10-15 min to form a precured PDMS substrate. (c) The ceramic strips with CNPs on them were placed on the precured PDMS which was heated at 60 °C for another 10-15 min. After the PDMS substrate was fully cured, the ceramic strips were carefully peeled off from the PDMS substrate. (e) Electrodes were deposited at the two ends of the CNPs films.

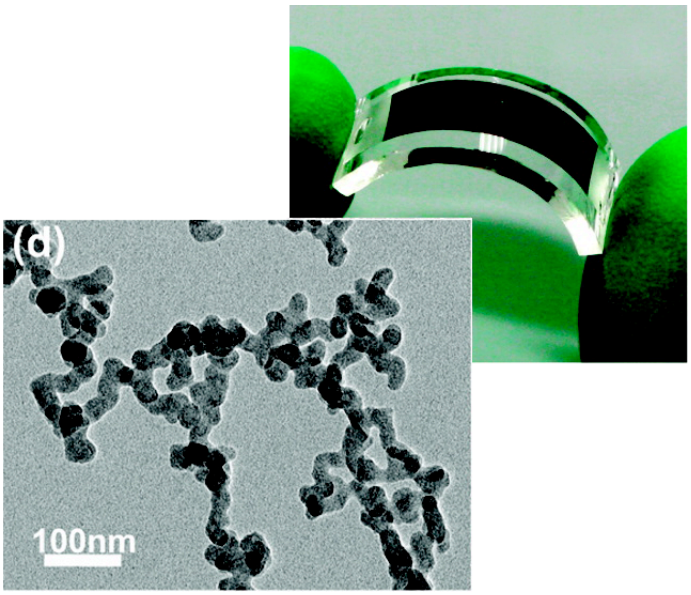

Figure 2. Optical image of the device, revealing the uniformity and flexibility of the CNPs after being transferred onto PDMS. (d) TEM image of CNPs.

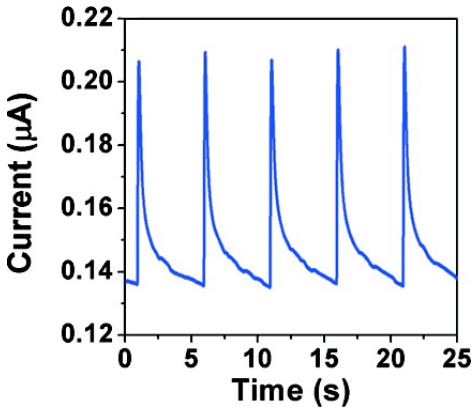

Figure 5. Infrared photoresponse characteristics of CNP-based sensors The infrared light source is an Nd:YAG laser with a photoemission wavelength of 1064 nm in pulse mode (2 ms pulse width, 5 s period, 7.8 mW/mm^2).

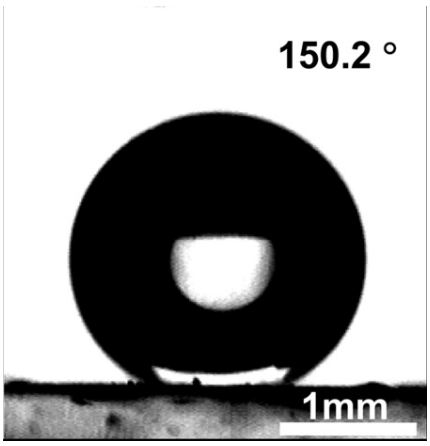

Figure 6. Water droplet of 5 μL on the device surface, showing a contact angle of 150.2°.

Chem 150 **Second Test** April 21, 2010

Interpret the figures by expanding on what is being illustrated, explaining procedures or techniques, indicating why it might be important or making connections to our class readings and laboratory work. Tell more than rewriting the caption. Try to use your interpretation to demonstrate additional knowledge beyond what is show here.

ACS Nano, March 2010, 10.1021/nn100197u

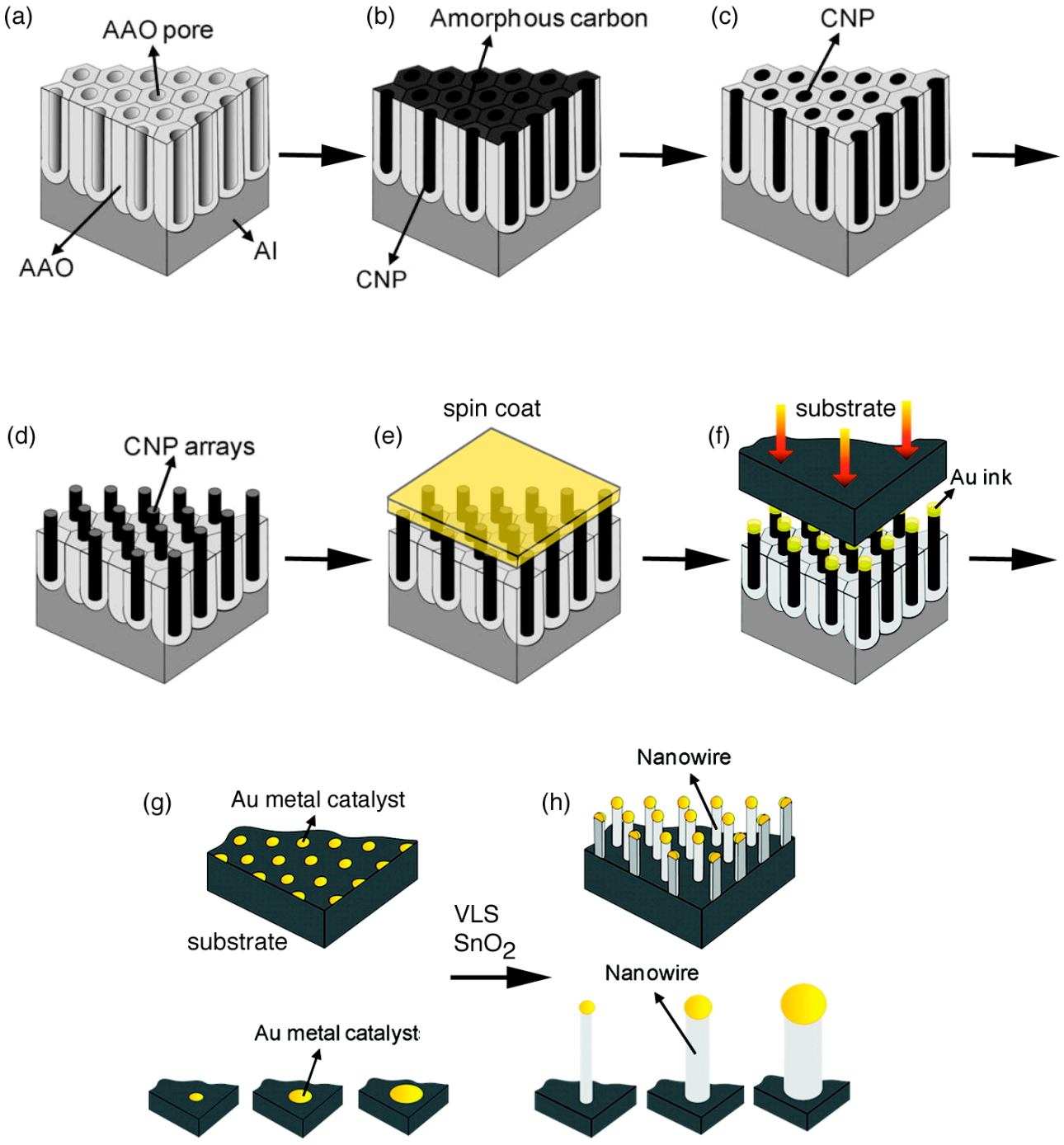

A schematic illustration of the synthetic procedures: (a) preparation of the nanoporous AAO template, (b) CVD at 600°C with a C_2H_2 and NH_3 gas mixture, (c) ion-milling, (d) selective wet-chemical etching, (e) spin-coating of $HAuCl_4$, (f) contact printing of the Au ink on a Si/SiO_2 substrate, (g) preparation of the Au metallic catalysts by annealing, and (h) growth of the semiconductor NWs from the contact printed Au catalysts.

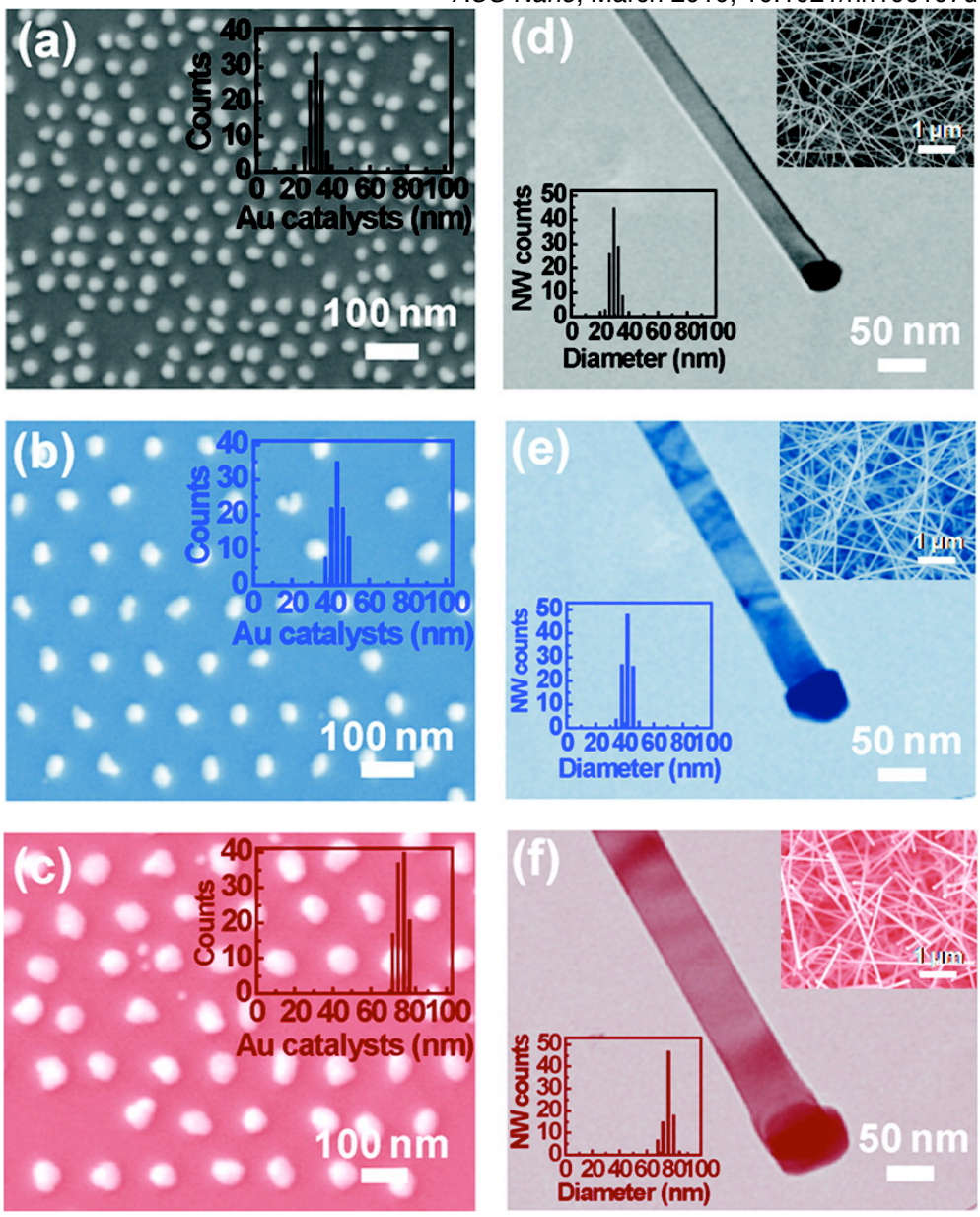

SEM images of contact-printed Au catalysts that display the average size of (a) 30, (b) 42, and (c) 71 nm, respectively. Insets show the histograms of the printed Au nanoparticles. TEM micrographs of grown SnO_2 NWs of (d) 32, (e) 43, (f) 77 nm in diameter, which were initiated over the printed Au catalysts. The SEM images of the upper insets display the SnO_2 NWs grown on the Au-catalyst-printed substrate. Lower insets indicate the histograms of the grown SnO_2 NWs.

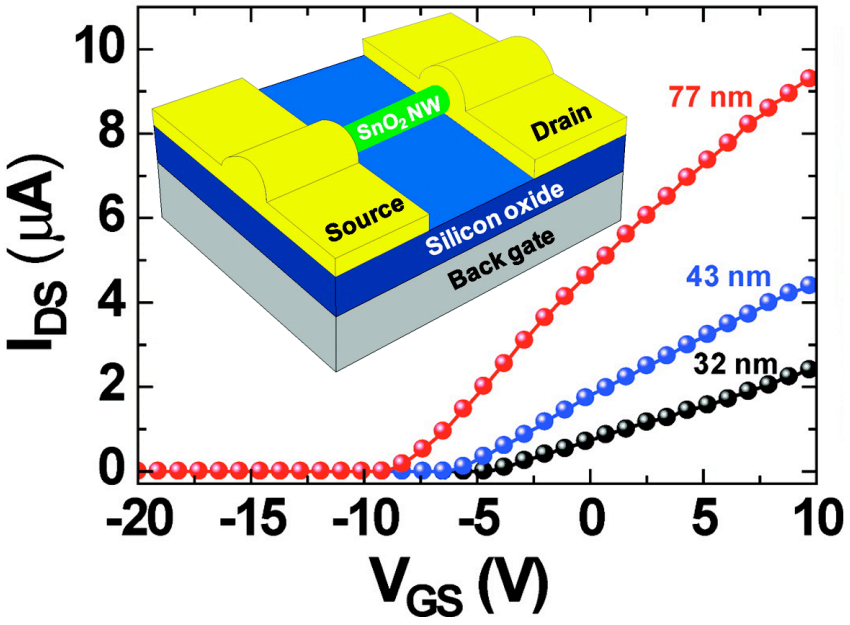

The SnO_2 NW-FETs transfer characteristics (I_{DS} *vs.* V_{GS}) at a fixed drain bias of 1 V exhibit typical n-type semiconductor characteristics.

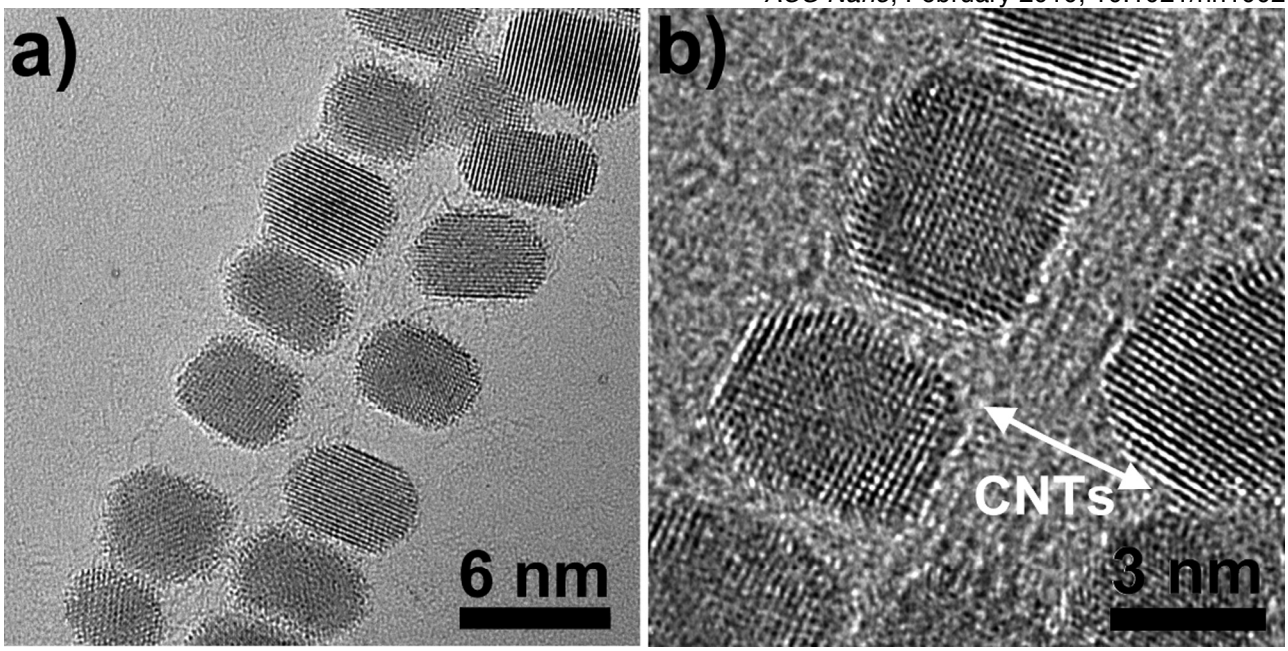

HRTEM images of CoPt NPs attached to SWCNTs show an atomically close proximity of the NP and the CNT surface, while there is a visible distance of about 0.8 nm between two adjacent NPs due to oleylamine ligands on the NP surfaces. The NPs are closely connected to the CNTs' surface with no apparent ligands between.

TEM image of CoPt NPs attached to SWCNTs (a) with corresponding electron diffraction (b).

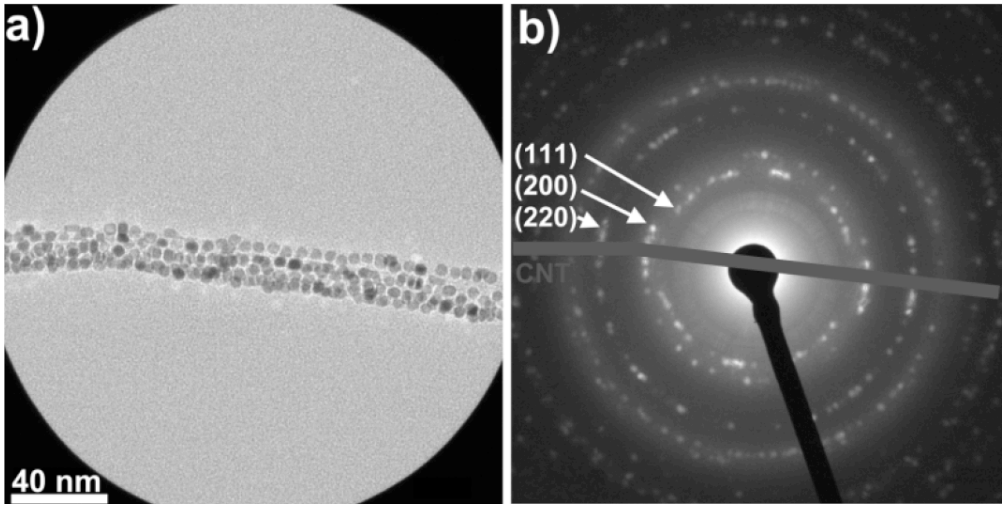

The Raman spectroscopy D-band corresponds to the sp^3 hybridization of the CNTs. If covalent functionalization of the CNT structure occurred, the intensity of the D-band would increase significantly.

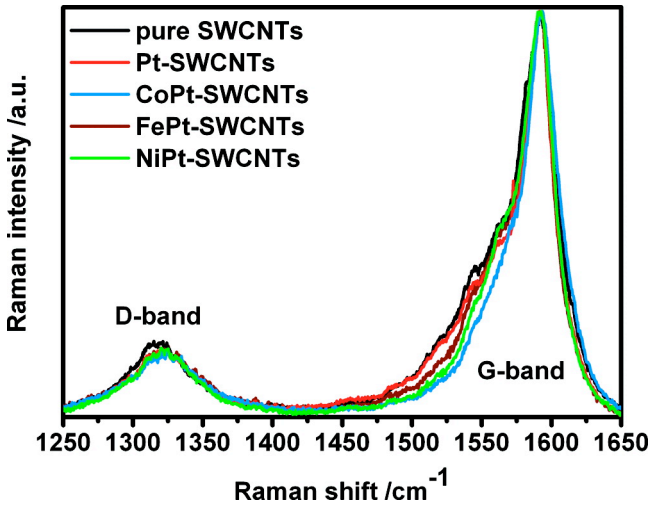

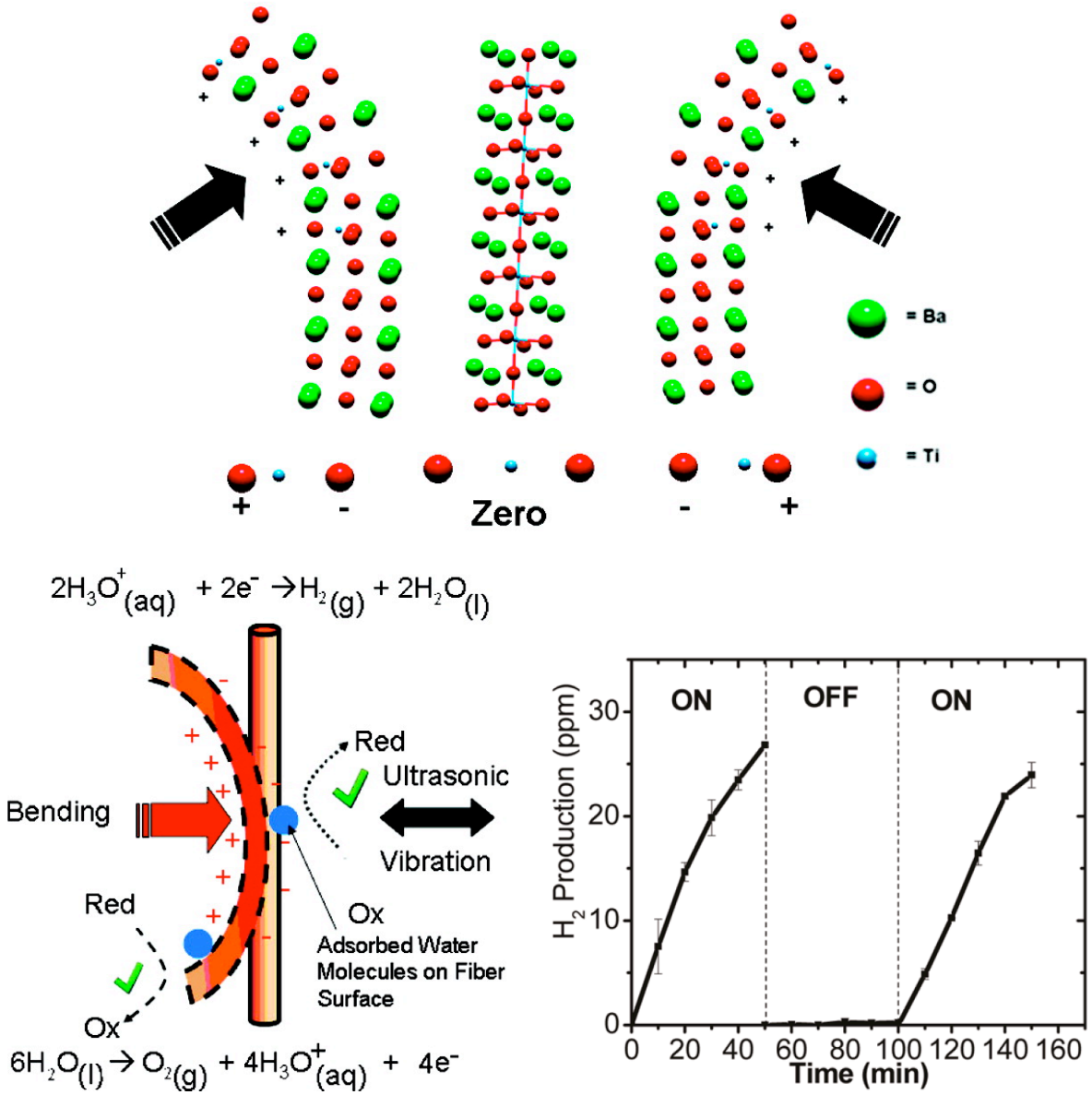

Schematic diagrams showing the charges developed on elongated $BaTiO_3$ microcrystals through bending with ultrasonic vibration in which the Ti-O distance changes. H_2 and O_2 are produced by deforming a $BaTiO_3$ dendrite in water via oxidation-reduction reactions. Gas generation stopped when the ultrasonic wave vibrations were turned off (51-100 min). After evacuating the reaction system and starting the ultrasonic waves again, a similar H_2 production rate was obtained.

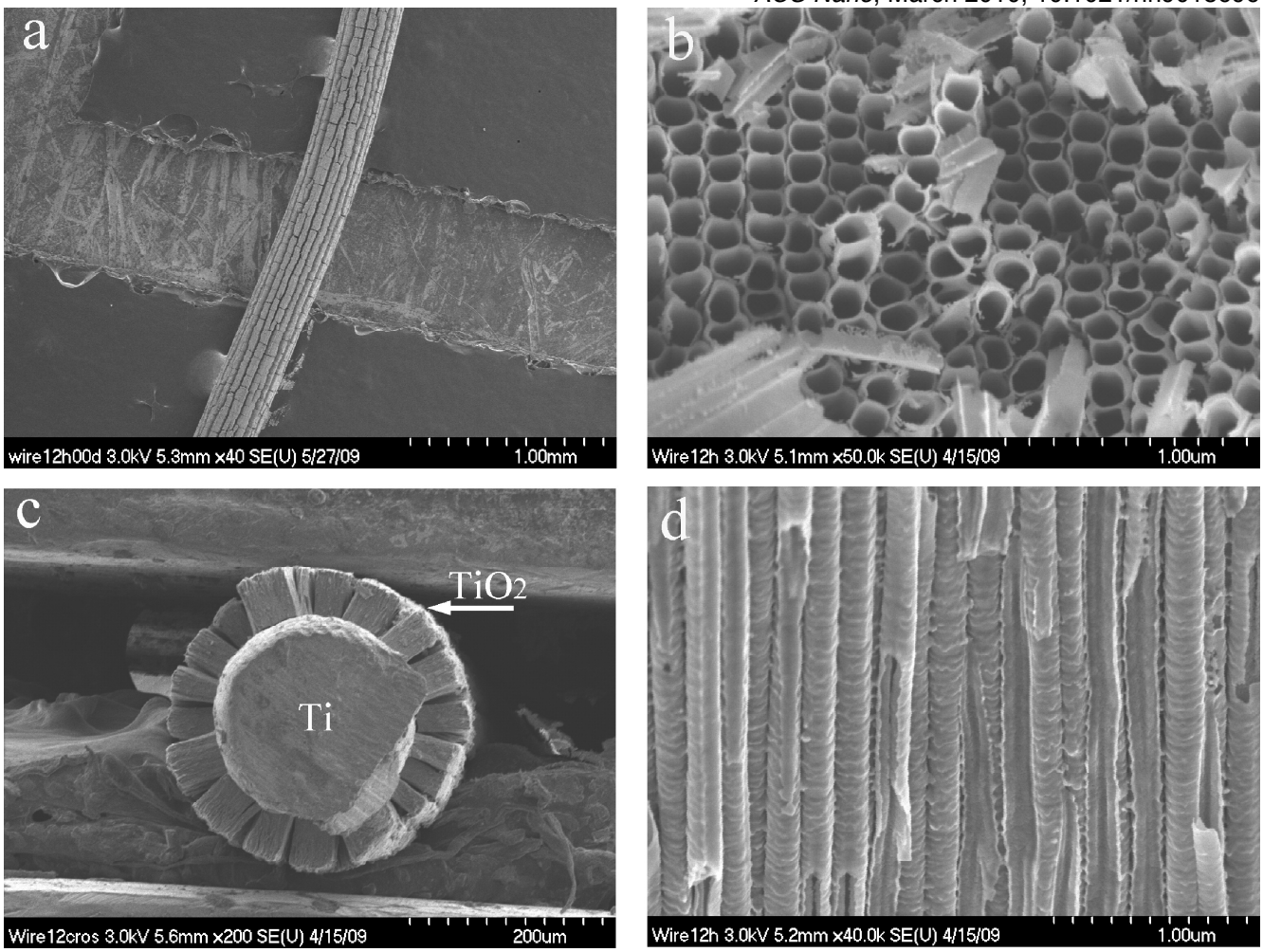

Top view (a,b) and cross-sectional (c,d) FESEM images of TiO_2 nanotube arrays grown around a Ti wire fabricated by anodization at 60 V for 12 h.

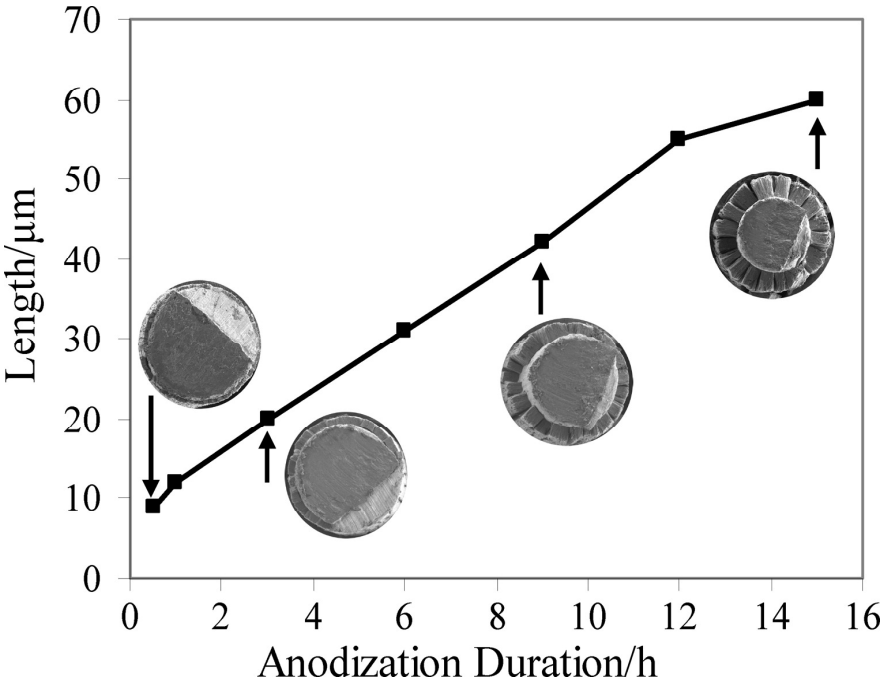

Effect of the anodization duration on the length of TiO_2 nanotube arrays grown around Ti wires.

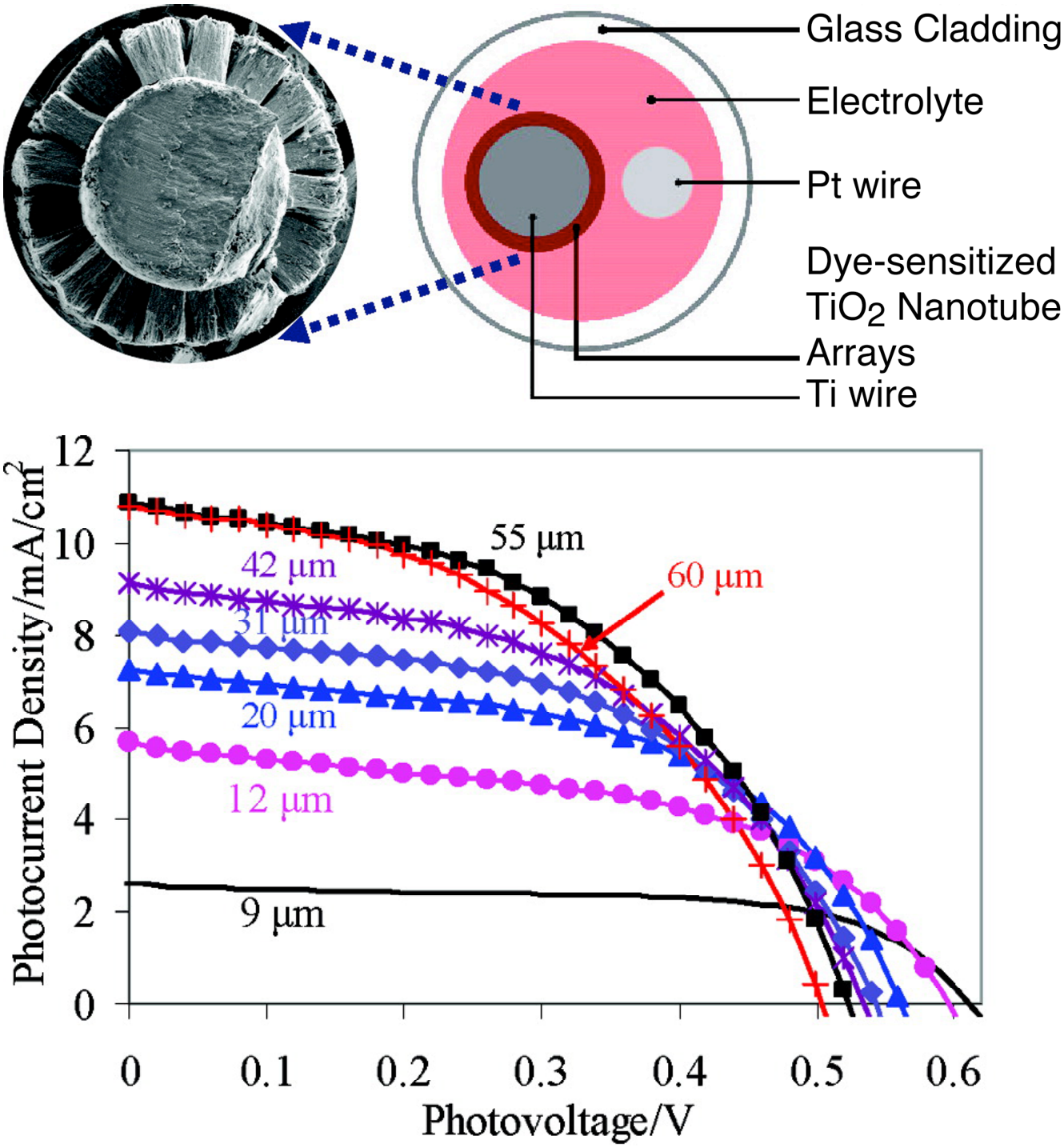

I V curves of prototype DSPVWs using TiO_2 nanotube arrays with varying lengths.